FREEFORM METROLOGY USING DEFLECTOMETRY

by

Logan Rodriguez Graves

A Dissertation Submitted to the Faculty of the

COLLEGE OF OPTICAL SCIENCES

In Partial Fulfillment of the Requirements
For the Degree of

DOCTOR OF PHILOSOPHY

In the Graduate College

THE UNIVERSITY OF ARIZONA

2019

THE UNIVERSITY OF ARIZONA
GRADUATE COLLEGE

As members of the Dissertation Committee, we certify that we have read the dissertation prepared by *Logan Graves*, titled *Freeform Optical Surface Testing with Deflectometry* and recommend that it be accepted as fulfilling the dissertation requirement for the Degree of Doctor of Philosophy.

Daewook Kim Date: 5-29-2019

Gregory Smith Date: 5/29/2019

James Schwiegerling Date: 5/29/2019

R. John Koshel Date: 5/29/2019

Final approval and acceptance of this dissertation is contingent upon the candidate's submission of the final copies of the dissertation to the Graduate College.

I hereby certify that I have read this dissertation prepared under my direction and recommend that it be accepted as fulfilling the dissertation requirement.

Daewook Kim Date: 5-29-2019
Dissertation Committee Chair
Optical Sciences/Astronomy

ACKNOWLEDGEMENTS

Dae Wook Kim: My mentor and friend. Thank you for sharing your endless enthusiasm and guidance.

Greg Smith: Thank you for your insight and mentorship.

Matt Dubin: I would most assuredly be a less skilled, and less interested, scientist without your influence. Thank you.

Tianquan Su and Run Huang: Thank you for your early guidance.

My Family: You all are incredible. I love you.

Large Optics and Fabrication Group: Thank you for the support and excellent memories.

Thank you for the opportunity of engaging in this research.

DEDICATION

To my family

both here and then,

with all my love.

TABLE OF CONTENTS

LIST OF FIGURES

APPENDIX A: Model-free Deflectometry for Freeform Optics Measurement Using an Iterative Reconstruction Technique

APPENDIX B: Model-free Deflectometry for Freeform Optics Measurement Using an Iterative Reconstruction Technique

APPENDIX C: Model-free Deflectometry for Freeform Optics Measurement Using an Iterative Reconstruction Technique

APPENDIX D: Model-free Deflectometry for Freeform Optics Measurement Using an Iterative Reconstruction Technique

APPENDIX E: Model-free Deflectometry for Freeform Optics Measurement Using an Iterative Reconstruction Technique

LIST OF TABLES

APPENDIX A: Model-free Deflectometry for Freeform Optics Measurement Using an Iterative Reconstruction Technique

APPENDIX B: Model-free Deflectometry for Freeform Optics Measurement Using an Iterative Reconstruction Technique

APPENDIX C: Model-free Deflectometry for Freeform Optics Measurement Using an Iterative Reconstruction Technique

APPENDIX D: Model-free Deflectometry for Freeform Optics Measurement Using an Iterative Reconstruction Technique

ABSTRACT

Precision freeform optics are finding increased usage in new optical systems. Deflectometry is a non-null optical metrology method that has great application potential to be a measurement method for freeform and standard optics, offering a wide slope dynamic range and excellent accuracy and precision. The technique utilizes a known source which emits rays of light that are deflected by the unit under test (UUT) and are captured by a recording camera. By knowing the precise location of the source, the ray intercepts at the UUT, and the camera, the local surface slopes of the UUT can be determined and integrated to obtain a reconstructed surface. This study investigates three major topics to improve deflectometry and identify new Deflectometric based techniques.

The first topic explored is a software-based method for an iterative surface reconstruction process. Deflectometry relies on determining the local surface slopes of the UUT by precisely knowing the ray intercept locations at the surface. Any error in the assumed surface model therefore directly reduces the reconstructed surface accuracy. A new processing method was developed called model-free deflectometry, which requires no optical surface model, and instead iteratively reconstructs the optical surface leading to improved final reconstruction accuracy. The method was used to reduce departure of a freeform optic from interferometric results from 15.80 μm root-mean-square (RMS) using model-based deflectometry down to 5.20 μm RMS with the model-free method developed. Further, most of the 5.20 μm RMS residual departure was explained using a simulation to model the inherent noise present from hardware limitations.

The second topic is a deflectometry system configuration which generates a virtual 2π steradian measurement volume, enabling full aperture deflectometry measurements of previously unmeasurable flat and convex freeform optics. The technique utilizes a source tilted over the UUT, enabling at least a partial aperture test. However, by clocking the UUT, a series of virtual sources are generated, which when considered as a whole, create a virtual source enclosure around the UUT allowing for a full aperture test. The method was shown to have accuracy similar to an interferometric test for a fast F/1.26 convex sphere and successfully tested a highly freeform Alvarez lens.

Lastly, a power scalable, time-modulated high stability infrared source is explored for infrared deflectometry. The new source is an integrating box design with a precision emission area machine cut into an aluminum box. The light sources are modular high-efficiency resistive alloy membranes held in small caps. The design allows for power scaling by adding or removing caps from the source design. The caps are powered in parallel and are modulated at approximately 1 Hz to allow for signal isolation, thereby greatly improving signal to noise ratio. The new source was compared with a traditional tungsten source, both run at the same power output, and the source stability and geometry compared. Several common optical surfaces were tested with both sources to compare the accuracy and precision of the sources. It was found that the integrating box features a significant improvement in performance.

1. INTRODUCTION

Freeform optics are finding increased usage in modern optical system. From artificial and virtual reality headsets to illumination systems and next generation extremely large telescopes, non-axisymmetric, complex optical surfaces, referred to as ‘freeforms’, are key technology enablers [1–7]. These complex surface shapes have created a distinct pressure on the fabrication and metrology areas of optics. Compounding this challenge is the expansion into crafting optics from new and exotic materials, including ultra-low expansion glasses such as Zerodur or simply 3D printed plastics. A customer expects a fabricated freeform optic to depart from the ideal shape by fewer than tens of nanometers root-mean-square (RMS). Fortunately, fabrication methods have rapidly evolved and are not only able to deliver optics which meet requirements but are now providing high efficiency and more streamlined fabrication processes for more rapid and reliable optics production. These fabrication methods include computer numeric controlled (CNC) machining and diamond turning, standard grinding and polishing, sub-aperture corrections via Magneto-Rheological Fluid (MRF) methods, or even 3D printing or molding methods [8–13].

These fabrication methods take a variety of materials, from glass to plastics or metals, and convert them from base material to a final precision surface. Not only is it essential to verify the final shape of the optic meets specification, but for many of these fabrication processes, accurate shape measurement detailing the progression of the optic is required. This area, known as metrology, is essential to enabling freeform optics fabrication. A variety of metrology methods exist, but broadly they can be divided into two main categories: contact and non-contact metrology. Both areas of metrology are essential for optical fabrication, but non-contact metrology is favored for cases where rapid and highly accurate metrology is needed, and can be safer for the optical surface [14]. The two most common non-contact metrology methods that can provide optical precision are interferometry and deflectometry. When cost and time are no issue, interferometry is the gold standard optical metrology method, which readily can achieve nanometer level surface measurement accuracy. Interferometry requires a null configuration, which in the case of freeform optics can mean custom null-optics are needed. Typically, this is achieved by using a computer-generated hologram (CGH) custom null optic. Although powerful, these null optics are custom only for one stage of one optic being tested, and they can be prohibitively expensive [15,16]. Deflectometry is a non-null test method which measures the local surface slopes of a unit under test (UUT) and integrates the slopes to reconstruct the surface. With proper calibration, the method can produce surface measurements comparable to commercial interferometry, with the added benefit of not requiring a null test configuration, making it an ideal metrology tool for the fabrication and verification of freeform optics [14,17,18].

Deflectometry utilizes a source and a camera to test the local surface slopes of a UUT. In a test, rays are emitted by a source and are deflected by the UUT. After deflection some rays enter the camera and are recorded on the detector. In a test setup, the camera detector is mapped to the UUT surface by focusing the camera onto the optic surface; in doing so local ‘mirror pixels’, or discrete areas on the UUT, are created, which are where the local slopes are be calculated. By carefully modulating the spatial source emission, the precise location of where the ray exited the source can be determined. Knowing the ray origin, the location of deflection at some mirror pixel, and the final ray end point on the camera detector, the local slope of the mirror pixel where the deflection occurred can be determined to high precision. The raw output of a deflectometry test is fundamentally the start ray positions at the screen and the corresponding end locations at the camera detector, from which using software methods the local slopes are calculated and integrated using either a zonal or modal integration method to reconstruct the optical surface [19].

Two factors must be satisfied for a deflectometry system to be able to test an optic. First, the UUT must specularly reflect the light emitted by the source for testing to be possible. For polished surfaces this is readily achieved using a digital source such as a liquid crystal display (LCD), and for ground surfaces utilizing an infrared source can satisfy the specular reflection condition, depending on how rough the surface is. Second, for an area on the UUT to be measurable, light emitted from some area on the source must be deflected into the camera. This is referred to as the slope dynamic range for deflectometry, which depends on the system hardware configuration. If a clear line of sight exists from a camera pixel to a UUT mirror pixel to a point within the source area (limited by source extent), obeying the law of reflection, it is within the testable dynamic range of the system. This is a highly important factor for freeform optics, which can have large surface slope ranges.

For deflectometry to be widely applicable as an optical quality test method for the next generation of freeform optics, several improvements are required. First, reconstruction accuracy when no accurate surface model exists, a common occurrence during the grinding phase of fabrication, must be improved. Second, deflectometry has historically been used primarily for metrology of concave optics; however, this leaves out testing of flat and especially convex optics. Thus, deflectometry must be expanded to provide accurate metrology to this range of optical surfaces. Finally, while deflectometry was extended to the infrared region to provide metrology of diffuse surfaces, the traditional source used for the system, a tungsten ribbon, suffers from several inherent limitations which must be addressed to improve the accuracy of infrared deflectometry, as well as to extend it to testing optics under thermal load. The scope of this study is the investigation of methods to address each of these topics, thereby improving deflectometry as a freeform metrology method.

1.1 Model-Free Deflectometry

Deflectometry is highly sensitive to system level errors and uncertainties. Particularly when calculating local slopes, any uncertainty in the assumed positions of all components, from the source, the UUT, and the camera, can significantly reduce the reconstruction accuracy [20,21]. Fundamentally, to calculate the local slope, a ray is traced from the source to the UUT, where the intercept location is determined (or assumed) and from there the ray is traced to the camera pixel which recorded it. While various calibration methods exist to verify the location and accuracy of the source and camera, including using precision measurement devices such as a laser tracker and spherical mounted retro-reflectors (SMRs) or a coordinate measurement machine (CMM) to determine the spatial coordinates the objects, no such method exists for verifying the UUT surface, which is the goal of a metrology test. In cases when no accurate UUT model exist, reconstruction accuracy using deflectometry is limited.

Historically, the simplest solution is to assume a flat for the UUT surface model, which can result in highly inaccurate reconstruction. Alternatively, an iterative system parameter optimization process can be used to improve reconstruction results [22]. Or, a non-zonal parameter dependent integration can be performed to improve the initial UUT model, followed by a successive over-relaxation zonal integration to improve the final reconstruction accuracy, provided the initial surface model is sufficiently accurate [23,24]. Building upon prior work in which a starting seed input surface model was iteratively improved by adjusting the radius of curvature of the model [25], a general method was developed, known as model-free iterative deflectometry (MID), which removes the need for any input surface model and instead performs and iterative surface reconstruction process to improve the final surface reconstruction accuracy. The method improves the surface reconstruction of freeform surfaces, including the low spatial frequency surface shapes which previously were not accurately reconstructed for deflectometry measurements using prior non-iterative techniques.

The present work in Section 2.1 introduces the MID algorithm, which relies on a multi-step software package to iteratively reconstruct the surface. A simulated system and error analysis, detailing the expected performance in the presence of noise and position uncertainty is presented in Section 2.1.2-2.1.3. The real-world performance demonstration is given in Section 2.1.4.

1.2 Infinite Deflectometry

One growing area of freeform design is that of convex or even flat freeform optics. Interferometry offers high accuracy surface metrology for optics, but it requires a null configuration for testing. Particularly for freeform optics, this means a custom null optic, such as a computer generated hologram (CGH), is required for accurate testing of such freeforms [15,16]. While offering numerous benefits, including alignment holograms and custom high precision nulls, CGHs can be prohibitively expensive and are usable only for one custom null configuration. Even with these advanced nulls, obtaining a full-aperture null for convex optics, or even larger flat optics, can be impossible. Thus, stitching interferometry can be required, in which sub-aperture areas of the optic are measured and stitched together. While great improvements have been made for stitching interferometry, the technique is both time consuming and, for non-axisymmetric optics, can require several custom null optics for different sub-apertures, increasing the complexity and cost of testing [26–29]. In some cases, it is non-feasible to perform a high accuracy stitching interferometric measurement of such optics. While contact metrology methods such as swing arm profilometry, CMM sampling, or the Hindle test exist for testing such surfaces, they cannot provide optical quality accuracy of the surface features, leaving high-frequency surface shapes on the order of nanometers untested [30,31].

Traditional deflectometry has served as a 3D surface reconstruction method for freeform concave surfaces through surfaces up to and including slow (i.e. large radius of curvature relative to diameter of optic) convex surfaces. However, a full aperture optical quality test of general convex optics, and particularly freeform convex optics, has not yet been achieved. Primarily, this is due to the traditional deflectometry configuration and how it is tied to the line of sight requirement for a test. For a traditional deflectometry system, the testable slope dynamic range of the UUT is determined by the source area. This can be determined by tracing rays in reverse from the pupil of the camera to the UUT and, following the law of reflection, to the source area. By calculating where the rays intercept the source plane, the required source area can be determined. In a traditional deflectometry setup for a concave surface, the camera and source will be located near the center of curvature of the optic, thereby approaching a one to one imaging condition and thus allowing for a small source area to test the entire optical aperture [4,32]. However, for a convex optical surface, the source cannot be placed at the center of curvature, and thus the required source area becomes extremely large (if not infinitely large).

One possible method to extend the testable slope dynamic range is to alter the deflectometry configuration by simply surrounding the UUT with five source walls. This technique, known as Cavlectometry, uses a multi-projector system to project a phase-shifted sinusoid pattern onto the side walls and roof of a room, which has a UUT located in the center of the room with a camera observing the surface, thereby creating a deflectometry setup [33]. The ray path for a traditional deflectometry setup and a source enclosure setup of a convex UUT is shown in figure 1.

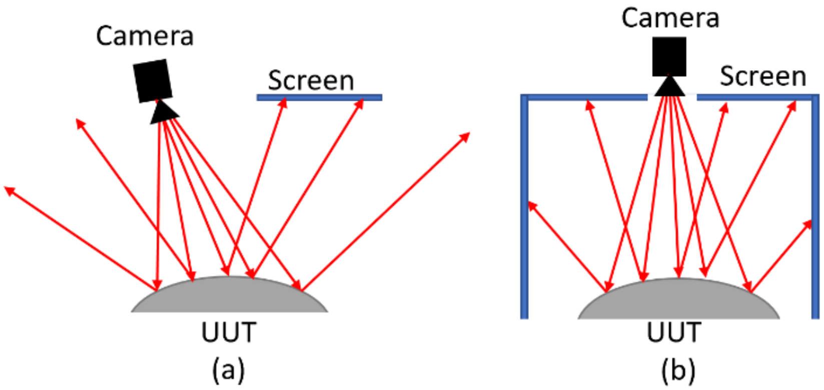

Figure 1. For a traditional deflectometry system, a digital display and camera are placed over the optic for measurement. However, this configuration only measures a small area of a convex UUT, as seen in a reverse ray trace of the system (a). Instead, by enclosing the UUT with a source, such as in a Cavlectometry configuration, a larger area of the UUT can be measured.

A phase-shifting deflectometry (PSD) measurement can then be performed and the surface can be reconstructed. While the method extends the testable slope dynamic range of a deflectometry system, it struggles with high-frequency nanometer level surface feature reconstruction. This is due to the lower resolution, optical aberrations, contrast uniformity, and other issues inherent in most projector systems [34,35]. These issues add uncertainty at the system level to the deflecomtetry test and limit reconstruction accuracy. For these reasons, traditional deflecomtetry tests for concave optics rely on modern digital displays, which possess characteristically higher resolution, but are limited by realizable source sizes and shapes (i.e. meter class flat LCD screens are the upper range of this type of source at the time of writing).

The present work in Section 2.2 introduces a new configuration called Infinite Deflectometry which creates a 2π-steradian measurement volume around a UUT to provide full aperture surface metrology of surfaces up to and including freeform convex optics. The system configuration is described in Section 2.2.1. Experimental results for a fast-convex spherical optic as well as a highly freeform Alvarez lens are provided in Sections 2.2.2-2.2.3.

1.3 Time Modulated Scalable Infrared Source for Long Wave Infrared Deflectometry

One area that heavily features freeform surface shapes is that of rough optical surfaces created during the grinding phase of optical fabrication. The grinding phase broadly covers the period when the surface figure error reduces from hundreds of microns down to ~1 μm RMS. Because of the large grit size used in grinding, it is possible to rapidly converge to the final desired surface shape, thereby making for a more efficient fabrication process. Of course, this is not the only area of optics which feature freeform rough surfaces. Solar collectors are being explored which are fabricated from metal plates and are shaped as parabolic troughs [36], as well as other optical components which are designed with a rough surface or feature a diffuse coating. These rough surfaces are challenging to test, as they do not specularly reflect visible light, thus visible deflectometry and interferometry are inapplicable.

Instead, infrared deflectometry has successfully been utilized to measure the surface of rough, non-specularly reflective freeform optics, such as that of the Daniel K. Inouye Solar Telescope 4.2 meter off-axis parabolic primary mirror [37]. For such testing the traditional source used is a scanning line source, which is created by heating a tungsten ribbon. Unfortunately, a tungsten ribbon has several fundamental limitations including low maximum driving power, non-uniform spatial emission, and unstable temporal emission characteristics. Additionally, some rough surface optics require testing while under thermal load. In these scenarios, not only are there minor thermal fluctuations from the background, but additionally, if the optic is under thermal load, the thermal emission may not be stable during a measurement. As with nearly all deflectometry measurements, a background signal is typically subtracted from measurement data. However, in infrared deflectometry testing, the common thermal fluctuations in testing, particularly for optics under thermal load, creates a fluctuating background which is not easily isolated from the true signal.

The presented work introduces a long-wave infrared temporally modulated integrating cavity (LITMIC) source. The source uses several resistive elements as power input to an integrating cavity, which has a machined exit slit that provides uniform emission. The system configuration and background are described in Section 2.3.1-2.3.3. Experimental results exploring the spatial and temporal characteristics of the LITMIC source as compared to a tungsten ribbon are explored in 2.3.4. Finally, an infrared deflectometry measurement of a rough ground glass optic, an aluminum blank, and an aluminum blank under thermal load was performed using both a traditional tungsten ribbon source and the LITMIC source. The reconstruction ability and the repeatability of both sources is examined in section 2.3.5. The LITMIC source demonstrates improved source properties, and the capability for a measurement of an optic under thermal load with a fluctuating background.

Note: This dissertation is based on a collection of published journal articles. The published works are connected under the umbrella of freeform testing with deflectometry and are integrated into this dissertation in a logical manner. In-depth discussion and treatment of the studies are provided in the appended reprints of the articles.

2. PRESENT STUDY

The methods, results, and conclusion of this study are presented in the papers appended to this dissertation.

2.1 Model-Free Deflectometry

Deflectometry requires accurate knowledge of the position of all components in a test configuration to correctly calculate surface slopes. In cases where no accurate surface model of the UUT is known, such as the grinding phase of an optic, in which millimeters of surface material may be removed between runs, reconstruction accuracy with deflecomtetry is severely limited, particularly for low-spatial frequency surface shapes such as power and astigmatism. Simple assumptions of a surface model, such as a flat or a best fit sphere, will be highly inaccurate for freeform optics, creating a challenge for accurate surface reconstruction of freeform surfaces with deflectometry. For these cases the reconstruction accuracy from a deflectometry test can be significantly improved by performing an iterative surface reconstruction process, called model-free iterative deflectometry (MID). The following Sections 2.1.1-2.1.4 are a summary of an article published in the journal *Optics Letters*, Appendix A, as well as a proceedings paper published and presented at *Optical Manufacturing and Testing XII*, Appendix D.

2.2.1 Iterative Surface Reconstruction

Accurate guiding of the fabrication process during the grinding phase, as well as accurate surface metrology for optics with unknown surface models, is an essential process. The need for accurate metrology for guiding freeform fabrication was demonstrated during the grinding process of the Daniel K. Inouye Solar Telescope (DKIST) primary mirror, during which grinding was guided by the then new infrared deflectometry system known as SLOTS [32,38]. During this period, several processes were in place to verify the base surface model of the DKIST primary mirror between SLOTS measurements, including using a Laser Tracker (LT) to map the base surface figure. In this way, a relatively precise surface model was always provided for processing the SLOTS deflectometry measurement of the UUT surface. The fabrication process and surface figure for the DKIST primary are shown in figure 2.

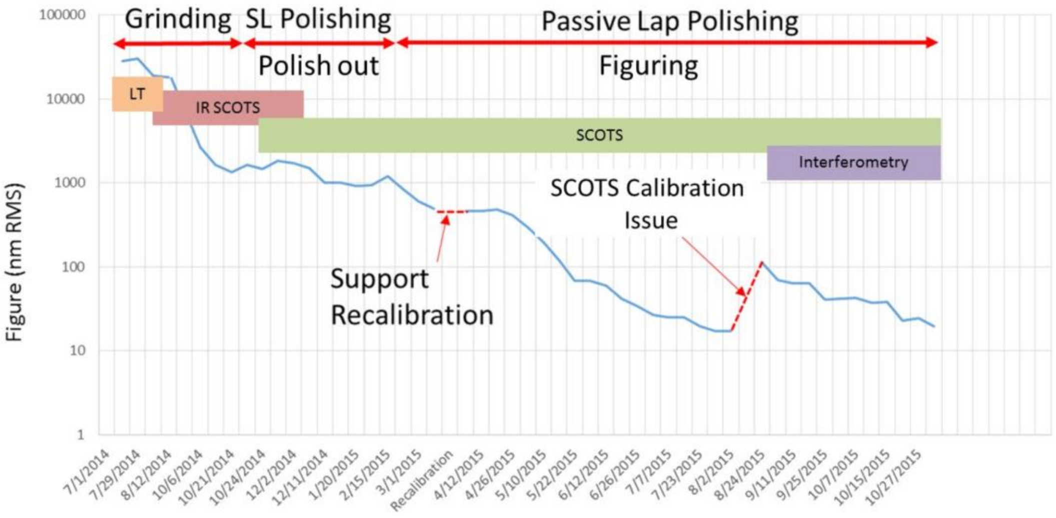

Figure 2. The grinding phase of optical fabrication represents a period of rapid material removal. If properly guided, as was the case during the DKIST primary mirror fabrication, the optic can rapidly approach the desired surface figure, shaving months to even years off of the total fabrication period [32].

Unfortunately, there are cases when a precise surface model cannot be readily provided to the deflectometry processing pipeline. In these cases, the simplest approach is to assume a flat surface model or make a best guess base surface shape model. However, both methods create a systematic error between the real ray intercept location at the UUT in the deflectometry test, and the assumed intercept location during the slope calculation. Particularly for freeform optics, this basic shape assumption will significantly depart from the true surface model and create significant error. This error manifests as inaccuracy in the reconstructed surface, predominantly in the low order spatial frequency surface shapes. By performing an iterative surface reconstruction, in which the precise ray intercept location is recalculated at each new reconstructed surface, an accurate surface model can be converged upon, thereby significantly improving final surface reconstruction accuracy.

The iterative surface reconstruction is accomplished via a process known as model-free iterative deflectometry which builds on preliminary work [25]. The MID technique improved reconstruction of freeform surfaces when no accurate surface model exists, particularly improving low spatial frequency terms like power and astigmatism, without the need for any input surface model. The method uses the freeform reconstructed surface that is output from a deflectometry measurement as a continuously updating surface model for the UUT. This iterative process is repeated until the reconstructed surface model converges, at which point the final reconstructed surface is output. By using an updating surface model, at each iteration the ray intercept calculation at the UUT becomes more accurate, improving the reconstruction accuracy across all spatial frequencies.

The MID approach takes as inputs the Cartesian coordinates of the camera and source, which are held in vectors C and S respectively. A flat surface model is generated as the UUT model, defined as matrix U^0. The UUT model solution space is bound using a measured physical coordinate on the UUT, $u_k(x,y,z)$. Additionally, the pointing vectors of the camera pixels, defined as matrix R, also must be precisely determined using a calibration process and input into the software. Using these inputs, the MID method then runs for $t = 0{:}N$ iterations. Inside of the MID process, the ray intercept locations at the UUT must first be determined. This is accomplished using a Delaunay triangulation [39], which segments the UUT surface mesh into unique, well-defined triangular surface planes, defined as matrix Q^t. With this matrix, a Möller–Trumbore algorithm [40] is used to efficiently and accurately determine the intercept locations at the UUT, with precision that exceeds the number of surface mesh points. The combined Delaunay/Möller -Trumbore (DMT) process is essential for accurately calculating the ray intercept locations, and thus accurate determination of the local surface slopes. It should be noted that the DMT processing time linearly increases while the reconstruction accuracy logarithmically improves with increasing sampling of the UUT surface, represented by the camera pixels measuring local areas on the UUT surface. Figure 3 demonstrates the combined DMT method and how it allows for greater intercept calculation accuracy than just relying on the mapped camera pixel mesh.

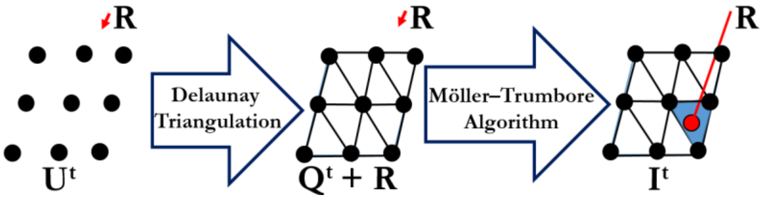

Figure 3. The DMT process takes a finite mesh of points, represented by matrix U^t, and segments the points into unique triangles, held in matrix Q^t. The rays are traced along their pointing vectors, R, and the precise intercept inside of the triangles is determined.

With the ray intercept locations, as well as the ray start and end locations from matrices C and S respectively, the local surface slopes of the UUT in the x and y directions, defined as matrices T_x^t

and T_y^t respectively, are determined. The surface is then reconstructed using a Southwell integration [19], and a new surface model is created, U^t, for that iteration. The process is iterated a total of N iterations, which results in a final output is the reconstructed surface model U^N. The entire iterative process is shown in figure 4.

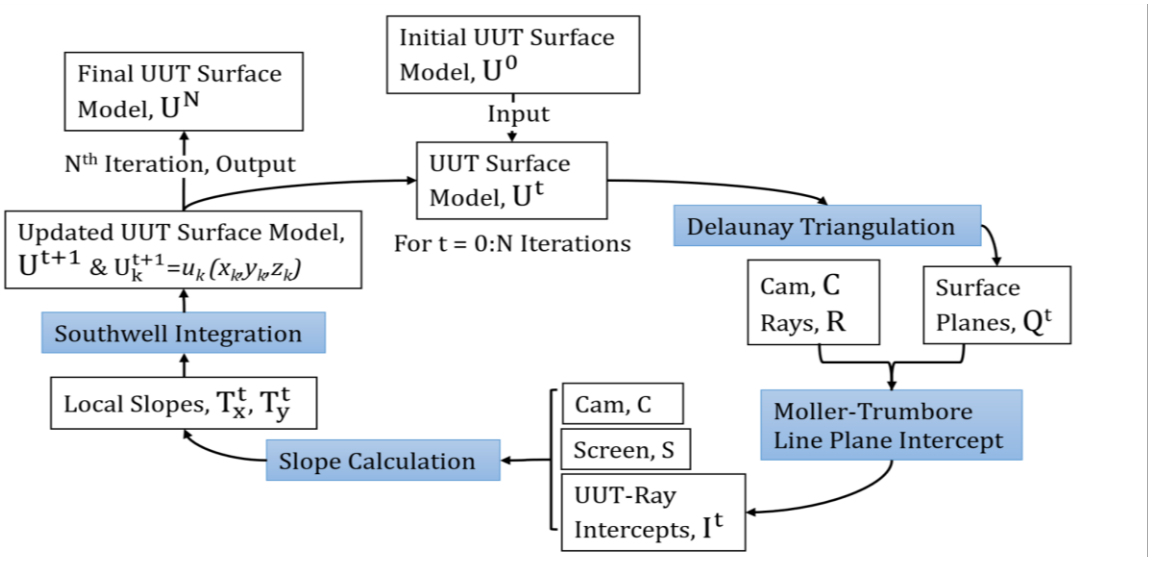

Figure 4. Using an initial flat surface model, U^0, the MID method iterates for a total of N iterations, at which point it converges to a final reconstructed surface model U^N.

2.2 Simulated System Performance

A simulated phase shifting deflectometry (PSD) software configurable optical test (SCOTS) system was modeled in Matlab. The camera detector was modeled as having a 101×101 array of pixels, with a pinhole camera system. The screen was modeled as a continuous plane. The system was modeled to test a segment of the James Webb Space Telescope (JWST) primary mirror [41]. The segment was modeled as 1320 mm in diameter, with a radius of curvature of 15899.91 mm and a conic of -0.99666, and was 1320 mm off axis from center, representing a real world freeform optic test case, and the UUT filled the camera detector. Rays were traced from the camera to the modeled UUT surface and were reflected to the source plane. Using the source and camera ray locations, the surface was reconstructed using the MID method for a total of nine iterations. Figure

5 demonstrates the results of the zero-iteration reconstruction, which is identical to a traditional non-iterative reconstruction process if a flat was the assumed surface model.

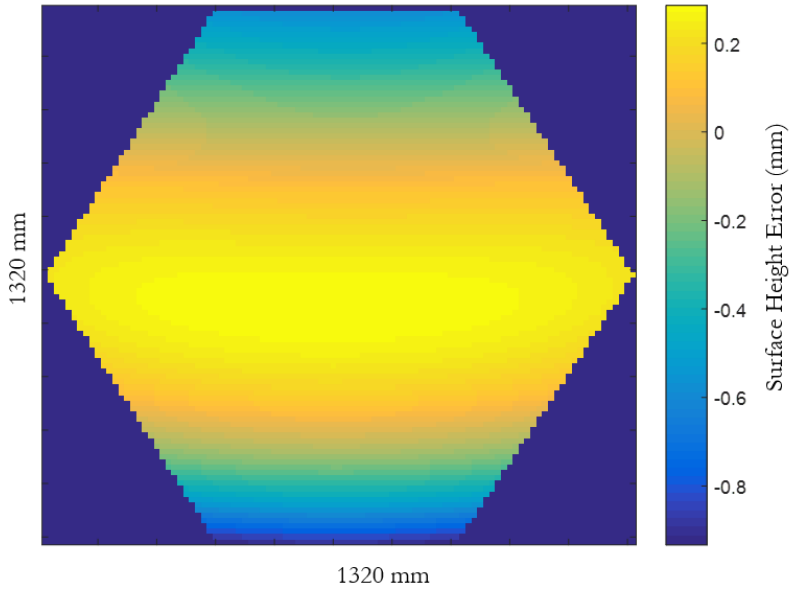

Figure 5. The JWST features several hexagonal off-axis aspheric surfaces. A mirror segment was modeled and a simulated deflectometry measurement was performed. The data was processed using the MID technique, to examine the reconstruction convergence process. As seen above, the zero-iteration surface has large reconstruction error, which is most heavily manifested as astigmatism.

The Delaunay triangulation process resulted in 20,000 surface triangle planes being generated, after which for every pixel on the camera detector the Möller -Trumbore process was used to determine the intercept coordinate on the surface planes. This process is a vectorized process to improve processing efficiency. Utilizing 8 Gb of RAM, with a single threaded Intel CPU operating at 2.90 GHz, the total time required for one iteration from start to finish was approximately 120 seconds, of which 93 seconds were required for the DMT process. For the simulation, with an ideal system, the final surface RMS difference from ideal was 6.17 picometers, which was approximately machine precision. With zero iterations, the RMS difference from ideal was 280.97 µm, thereby demonstrating the MID approach significantly improves reconstruction accuracy.

Of course, in a real test, random noise as well as systematic uncertainty are primary concerns. In the case of noise, random white noise ranging from 0 to 1 µm in the x and y positions was added to the detector coordinates. White noise added a random high spatial frequency error in the final reconstructed surface map with a root-mean-square (RMS) error of 11.17 nm from the ideal surface shape. The reconstruction RMS error through iterations, as well as the surface reconstruction generated after the total of nine iterations had run for both the white noise and positional uncertainty cases are shown below in figure 6.

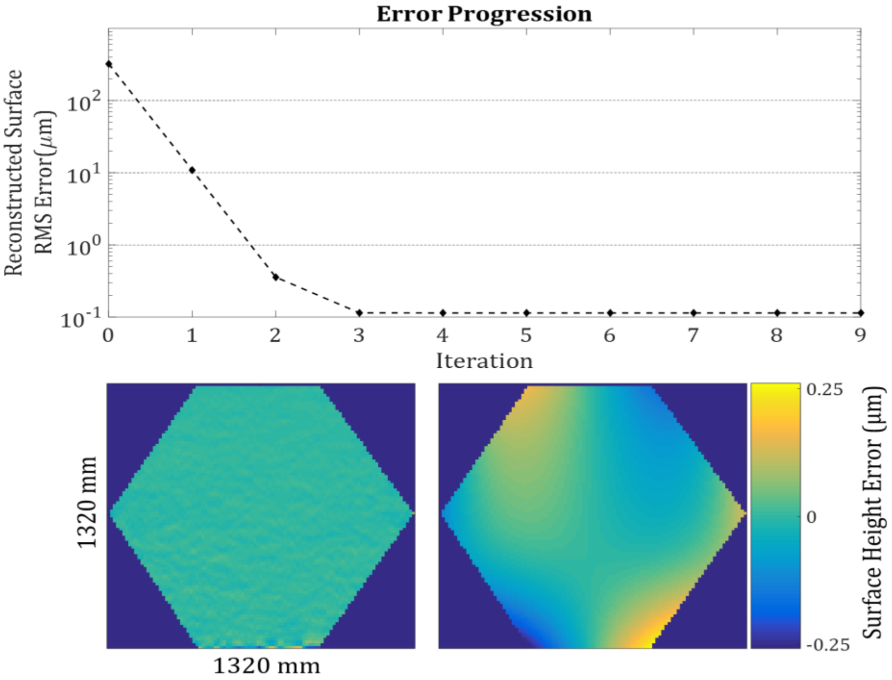

Figure 6. After simulating a deflectometry test of a segment of the JWST primary mirror, the surface was reconstructed using the MID method for a total of nine iterations. The reconstructed RMS error was determined at the end of each iteration (top). Additionally, white noise was simulated to model screen uncertainty, which resulted in a random high frequency error in the final reconstructed surface (bottom left), while a positional uncertainty in the position of the camera pupil resulted in low-spatial frequency reconstruction errors (bottom right).

Additionally, a real-world test was performed of a highly freeform optic, which had a unique spiral pattern imparted on a base sphere surface. This system was modeled in Matlab, replacing the freeform nature of the optic with just a sphere, and the uncertainty in the coordinates of the camera and source, which were measurable to an accuracy of ±10 μm in position and ±1 mrad in angular accuracy, were modeled. Using the real measured ray vectors for the camera a simulation was performed which reconstructed the surface using the MID method with 6 iterations, which was sampled using a 512×512 grid, to match the pixel array size in the real test. For no positioning uncertainty, the MID method reconstructed the modeled spherical surface to machine precision. With the position uncertainty modeled however, there was clear error in the reconstruction even with the MID method, particularly at low-spatial frequency terms. The root-sum-square (RSS) error between the MID reconstructed surface and the ideal surface was approximately 5 μm and was predominantly arising from astigmatic error, which was very similar to the real-world test result results. The full summary of the error, which was calculated by fitting Standard Zernike terms 5:11 to the difference between the reconstructed surface and the ideal surface, after modeling the system with an error of 10 μm in x, y, and z and 1 mrad in tip, tilt, and roll for the camera and screen separately is given in tables 1 and 2.

Table 1. Model-free Iterative Deflectometry Reconstruction Error with Screen Uncertainty

Zernike Terms	10 µm X Pos. Error (µm)	10 µm Y Pos. Error (µm)	10 µm Z Pos. Error (µm)	1 mrad Tip Error (µm)	1 mrad Tilt Error (µm)	1 mrad Rotation Error (µm)	RSS Value (µm)
Z5	0.003	-1.497	-0.042	0.031	-0.002	-0.001	**1.50**
Z6	1.471	0.002	0.203	0.001	0.034	0.002	**1.49**
Z7	0.005	0.603	0.010	0.003	0.001	0.001	**0.60**
Z8	0.576	0.007	0.038	0.002	0.002	0.001	**0.58**
Z9	0.028	0.161	0.031	0.078	-0.015	-0.002	**0.18**
Z10	-0.580	0.161	-0.102	0.018	0.078	0.002	**0.62**
Z11	0.207	0.171	0.152	0.170	0.170	0.170	**0.38**

Table 2. Model-free Iterative Deflectometry Reconstruction Error with Camera Uncertainty

Zernike Terms	10 µm X Pos. Error (µm)	10 µm Y Pos. Error (µm)	10 µm Z Pos. Error (µm)	1 mrad Tip Error (µm)	1 mrad Tilt Error (µm)	1 mrad Rotation Error (µm)	RSS Value (µm)
Z5	-0.006	4.119	-0.120	-0.001	-0.001	-0.001	**4.12**
Z6	-4.093	0.000	0.600	0.000	0.000	0.000	**4.14**
Z7	-0.008	-1.311	0.055	0.001	0.001	0.001	**1.31**
Z8	-1.253	-0.008	0.261	0.001	0.001	0.001	**1.28**
Z9	-0.203	-1.033	0.051	0.000	0.000	0.000	**1.05**
Z10	1.787	-0.313	-0.177	0.004	0.004	0.004	**1.82**
Z11	0.092	0.165	-0.479	0.170	0.170	0.170	**0.56**

2.2.3 Model-Free Test of Freeform Optic

To demonstrate the efficacy of the MID approach, a real test of a bare glass optical surface with freeform departure from a sphere in all directions was measured. The radius of curvature (RoC) of the surface was 200 mm and the diameter was 100 mm. The UUT had ~0.67 µm RMS and ~2.50 µm PV departure from the base sphere, with a maximum surface slope of 576.64 µrad. The optic was fabricated using a magnetorheological finishing (MRF) technique to impart a spiral pattern on the optical surface.

As a baseline, the surface was measured using a commercial Zygo Verifire^{TM} MST interferometer. To acquire the deflectometry measurement of the surface, a simple SCOTS deflecomtetry system was used. It must be noted that the interferometric technique used does not accurately reconstruct piston, tip, tilt, or power terms of the UUT, therefore, these terms were not considered in the final reconstructed surface comparisons. For this optic, there was no custom null on hand, thus, an ideal null configuration could not be obtained on the interferometer, and the high fringe density at best null resulted in some untestable areas on the optic. Figure 5 demonstrates the best null configuration and the fringe density issues.

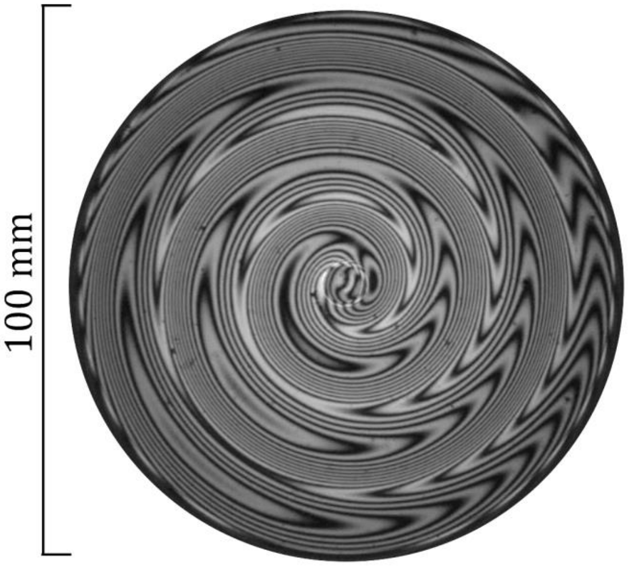

Figure 7. Interferometry requires a null configuration for testing an optic. In the case of a complex spiral pattern freeform optic, no custom null was available, instead, the best spherical null was used. At best null configuration, the interference pattern suffered from high fringe density, limiting reconstruction of some areas, as seen above. Deflectometry on the other hand does not require a null configuration, and instead can readily test such complex freeform surfaces, provided an accurate surface model is given, or, if that is not possible, the MID method can be used.

The optic was also tested using a SCOTS system, which has all components mounted into place on a breadboard. The coordinates of all components were measured using a CMM to an accuracy of ±10 μm, while the ray vectors of the camera pixels were calibrated prior to the test and known for the system. The optic was placed on a rotation stage, and multiple clocking positions of the optic were taken and used to remove systematic error via a rotation calibration process [42]. Taking the raw data from the deflectometry test, the surface was reconstructed in three ways. The surface was reconstructed using the MID method, using a total of six iterations. Additionally, as a comparison, a traditional non-iterative reconstruction was performed assuming (1) a flat for the base optical surface, and (2) a best fit sphere of 200 mm radius of curvature. All reconstruction methods used the same raw input deflectometry data. The MID reconstructed surface, termed MID_6, the flat model traditional reconstructed surface, termed MB_{flat}, and the best fit sphere model traditional reconstructed surface, termed MB_{sphere}, where then analyzed to compare the Standard Zernike terms between the reconstructed surface and the measured surface from the interferometric measurement, referred to as INT. It must be noted that the missing data regions in the INT map were not considered in the comparisons.

For the comparison, low-spatial frequency surface differences were analyzed by fitting Standard Zernike terms 5:11 to the difference maps between INT and MID_6, MB_{flat}, and MB_{sphere}. Zernike terms 1:4, representing piston, tip, tilt, and power were not considered. Table 3 demonstrates the resulting Zernike term differences of the surfaces.

Table 3. Low Order RMS normalized Zernike Term Difference between Reconstructed and Interferometric Surface Maps

Zernike Term	**MID_6 (µm)**	**MB_{flat} (µm)**	**MB_{sphere} (µm)**
Z5, Oblique Astigmatism	0.76	1.90	0.42
Z6, Vertical Astigmatism	-5.12	-44.28	-15.80
Z7, Vertical Coma	-0.36	-1.98	-0.40
Z8, Horizontal Coma	-0.10	0.55	0.11
Z9, Vertical Trefoil	0.32	1.01	0.25
Z10, Oblique Trefoil	-0.05	0.29	0.06
Z11, Spherical	0.04	0.63	0.17

Z5:Z11 Total RMS Diff	5.20	44.39	15.80

The total Zernike term RMS departure, for low order terms Z5-Z11, from the INT for MID_6, $\mathrm{MB}_{\mathrm{flat}}$, and $\mathrm{MB}_{\mathrm{sphere}}$ surfaces were 5.20 µm, 44.39 µm, and 15.80 µm, respectively. The MID method was thus able to reduce the reconstruction difference for a deflectometry measurement from an interferometer measurement of the same optic by a factor of nearly 10 when no model is provided, and by roughly a factor of 3 when a best fit base surface model was provided. The reconstructed surface maps, with increasing Zernike term removal, are shown in figure 6.

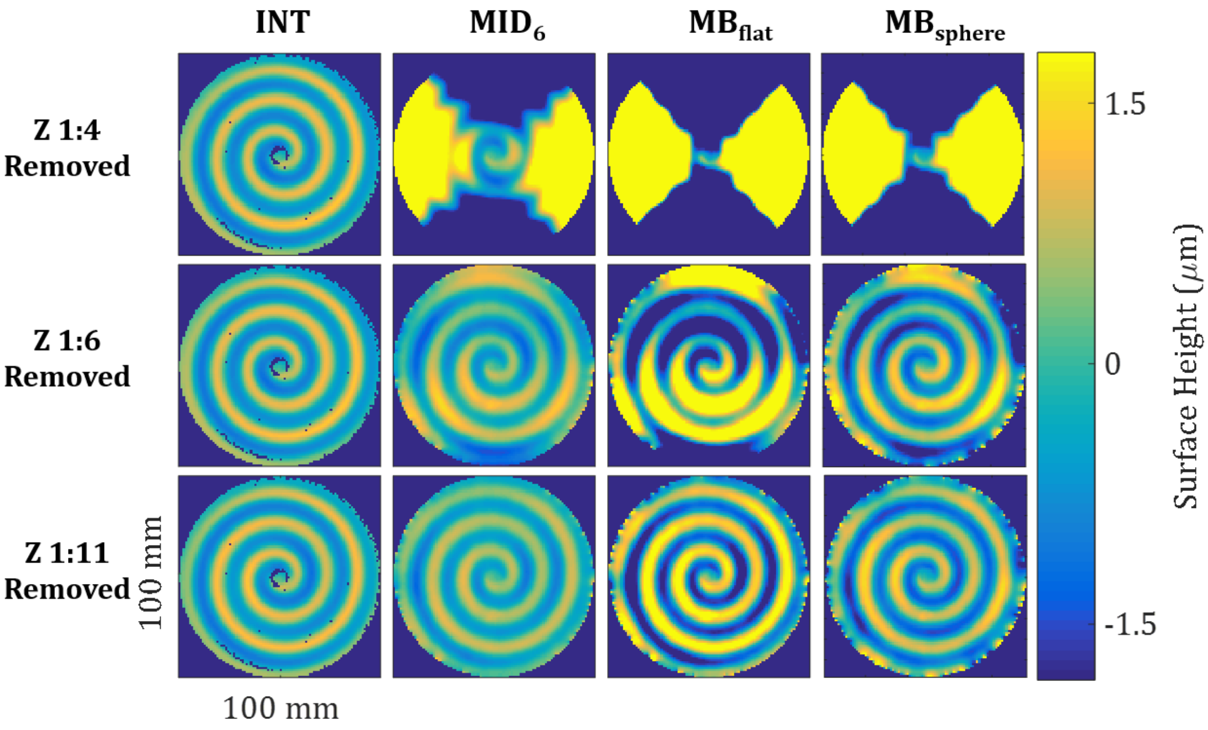

Figure 8. The reconstructed interferometric surface map (1st col), MID method with 6 iterations (2nd col), and non-iterative traditional reconstruction with a flat UUT model (3rd col) and a 200 mm RoC base sphere model (4th col) method had Zernike terms 1-4 (top row), 1-6 (middle row), and 1-11(bottom row) removed to compare error contribution from low spatial frequency. (Note: Excess fringe density led to missing data in the interferometric map).

The MID technique resulted in a surface which more closely matched the interferometric measurement when compared to a traditional non-iterative technique for model-free deflectometry surface reconstruction. Particularly at the low spatial frequencies it achieved more similar results to the interferometric measurement. Small uncertainties in geometrical knowledge of the positions of all components contributed to some of the residual astigmatism and coma in the MID_6 reconstructed surface, as demonstrated by the simulation of the test. However, the MID method improves the well-known low order accuracy issues of traditional deflectometry while maintaining the advantage of a large dynamic range, when compared to interferometry. The effect of dynamic range is particularly clear for this UUT, which suffered from missing data regions in the measured interferometric map due to the inability to obtain a null over the entire surface.

In summary, the MID method was shown to provide significantly improved reconstructed accuracy for freeform surfaces measured by a deflectometry system when no accurate surface model exists. The technique can readily be applied for any deflectometry case when a deflectometry system has measured an optic. A novel deflectometry configure which addresses the need for testing convex freeforms is investigated in Section 2.2.

2.2 Infinite Deflectometry for Creating a 2π Steradian Measurement Volume

Historically deflectometry has provided precision metrology to optics with a concave base shape. However, this leaves out more than half of the optics spectrum, thus a need for deflectometry of flat and convex optics exists. This is especially true for freeform convex optics, as interferometry typically may require stitching for accurate measurement of a convex surface, which, for a freeform convex optic, can require complex configurations and multiple custom CGHs. By creating a virtual source enclosure around an optic under test, deflectometry can readily measure up to highly convex freeform surfaces. By leveraging modern sources in a unique configuration known as Infinite Deflectometry, optical quality testing of any UUT surface, from concave to convex in base shape, can be achieved, thereby extending deflectometry as a freeform metrology device. The following Sections 2.2.1-2.2.4 are a summary of an article published in the journal *Optics Express*, Appendix B.

2.2.1 Source Enclosure for Extended Slope Dynamic Range

The slope dynamic range of a deflectometry system is defined as the measurable surface slope range on the UUT surface which can be measured given the size and position of the camera and source. It can be more easily understood if the system is traced in reverse, taking a ray from the camera pupil and tracing it to the UUT surface. Based on the surface slope, the reflection angle of the ray can be determined using the law of reflection and can be propagated to the source. If the ray intercepts the source, the slope of the UUT can be measured. For concave optics, by placing the camera and source near the center of curvature, a near one to one imaging condition is met, allowing for all pixels in the camera pupil to be traced to the UUT surface and to return to a small focused bundle near the center of curvature of the mirror. Thus only a small source area is required for testing. However, for convex surfaces, this is not the case, as rays traced to the surface of the UUT come to a virtual focus, and instead in image space diverge, thus requiring a potentially infinitely large source. The ray path for rays traced from a deflectometry camera to a concave and convex UUT is shown in figure 7.

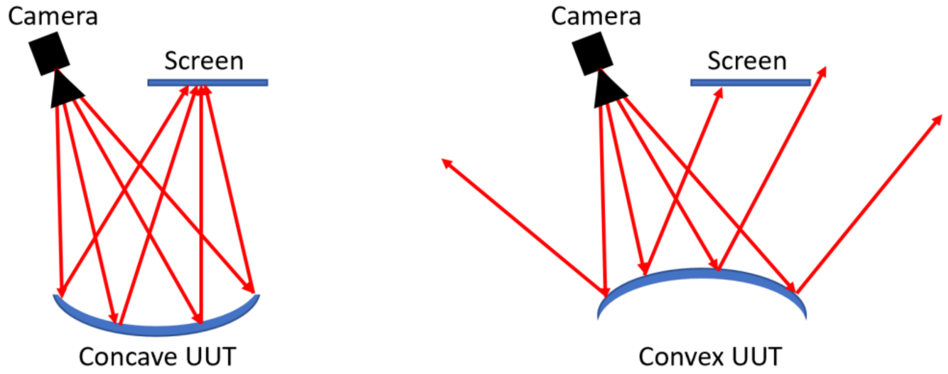

Figure 9. For a traditional deflectometry system, the required source area for testing the slope range of a UUT can be determined by tracing rays from the camera, reflecting them from the UUT, and tracing to the source. For a concave UUT, if the camera and screen are placed near the UUT center of curvature, only a small area on the screen is required for full aperture testing. The same setup for a convex UUT fails to test the full aperture of the UUT.

One approach to a deflectometry test of a convex or freeform object is to surround the UUT with a source enclosure using projectors to project a phase-shifting deflectometry pattern on the walls of a room. This technique, known as Cavlectometry, was able to reconstruct low spatial frequency features of freeform objects, including a car hood an even a teapot [33]. Due to the inherent optical aberrations in a projector system, as well as other systematic errors, the method is unable to achieve optical quality reconstruction, particularly of high-frequency surface shapes. Therefore, it is desirable to achieve the same source enclosure but with a higher quality source.

This is achieved in the method known as Infinite Deflectometry. The approach places the UUT on a precision rotation stage and tilts a high-resolution modern LCD source over the UUT. A camera is mounted in place over the UUT and is focused on the UUT surface, as in a traditional deflectometry test. The UUT is then clocked at several positions through a full 2π radians. This process can be thought of as clocking the screen around the UUT instead, creating a virtual screen at each clocking position. At each clocking position, a phase shifting deflectometry measurement can be performed, measuring a different area on the UUT. By combining all the individual deflectometry measurements, a virtual source enclosure is created around the UUT, forming a tipi shaped 2π-steradian measurement volume around the UUT. The base system configuration, as well as a ray trace showing where individual rays strike intercept the source enclosure at each clocking position is shown in figure 8.

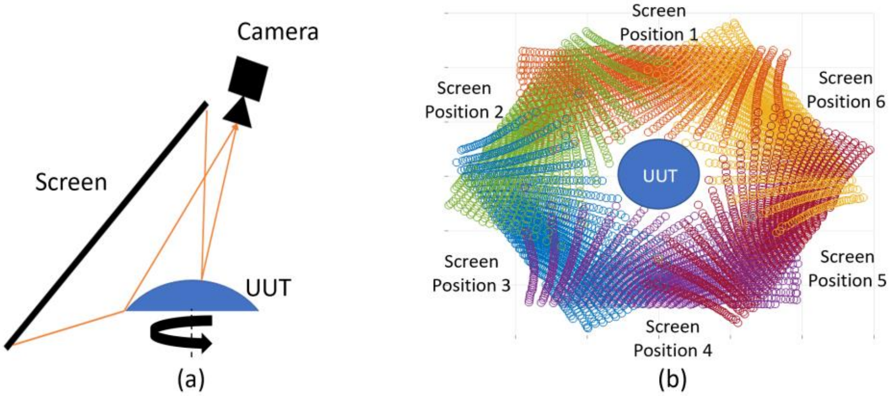

Figure 10. Infinite Deflectometry relies on mounting a UUT on a precision rotation stage and tilting a high-resolution screen over the surface. A camera is mounted above the UUT (a). The UUT is then clocked, which creates a series of virtual screens around the UUT. By considering all the virtual screens together, a 'tipi' like virtual source enclosure is created around the UUT (b).

At each clocking position, at least some portion of the UUT aperture is measured, resulting in a raw deflectometry data for every clocking position. This raw data is converted to local slope measurements of the measured portion of the UUT aperture for every clocking position. These sub-aperture local slope maps are then converted to a cohesive full-aperture local slope map of the UUT. This is done by performing a linear interpolation of the data, after first removing the piston and tip/tilt of the local slope maps to better assure proper stitching. Note that the removal of piston in slope domain removes tip/tilt in the surface domain, while tip/tilt in slope domain removes power and astigmatism in the surface domain, thus, these features cannot reliably be represented in the reconstructed surface when using this stitching methodology. The final full-aperture local slope map is then integrated using a Southwell integration to reconstruct the full aperture surface map. Figure 9 demonstrates the flow down chart from the raw data output from an Infinite Deflectometry measurement of an optic to the final reconstructed surface.

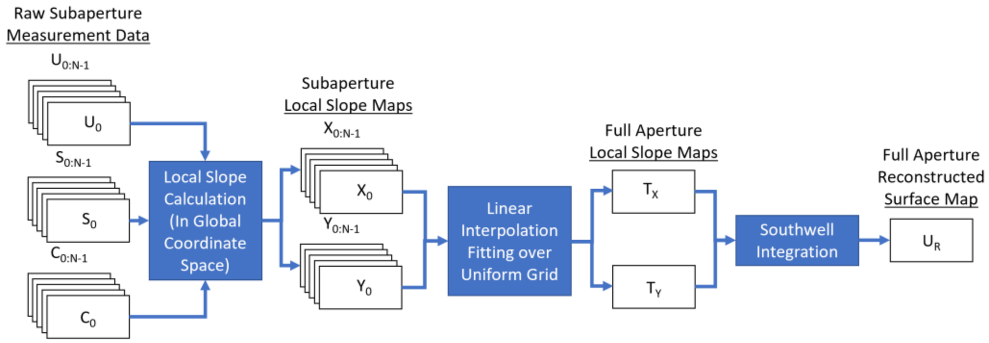

Figure 11. An Infinite Deflectometry takes a deflectometry measurement at *N* clocking positions of a UUT, resulting in at least a partial measurement of the UUT aperture. This raw measurement data, which consists of the camera, screen, and UUT positions at each clocking position, is converted to local slope maps at each clocking position. A linear interpolation is performed to combine the individual clocking measurements into full aperture local slope maps, which are then integrated to reconstruct the surface across the full aperture.

This combined hardware and software process described the entire Infinite Deflectometry process. The method enables measuring concave to convex standard and even highly freeform surfaces. Sections 2.2.2-2.2.3 describe measurements of a fast-convex spherical optic as well as a highly freeform Alvarez lens surface. The hardware for the Infinite Deflectometry system featured a Point Grey Flea3 camera (Model # FL3-U3-32S2M-CS), which has a 2.5 µm pixel pitch. The source was an Apple iPad Pro (Model # A1670) which measured 262.85 × 197.04 mm and had 2732 × 2048 pixels, with a 96.2 µm pixel pitch. The UUT was positioned on a custom 3D printed mount, which fit into a Klinger motorized rotary stage (Model # DP179), driven by a Leadshine digital stepper driver (Model # EM402).

2.2.2 Measurement of a Fast F/1.26 Convex Spherical Optic

A fast f/1.26 50 mm diameter convex sphere was measured using the previously described Infinite Deflectometry system. Additionally, the surface was measured on a Zygo Verifire commercial interferometer, using an f/0.75 reference sphere. The resulting measured UUT area in the base configuration of the Infinite Deflectometry setup, as well as the best null of the UUT on the interferometer are shown in figure 10.

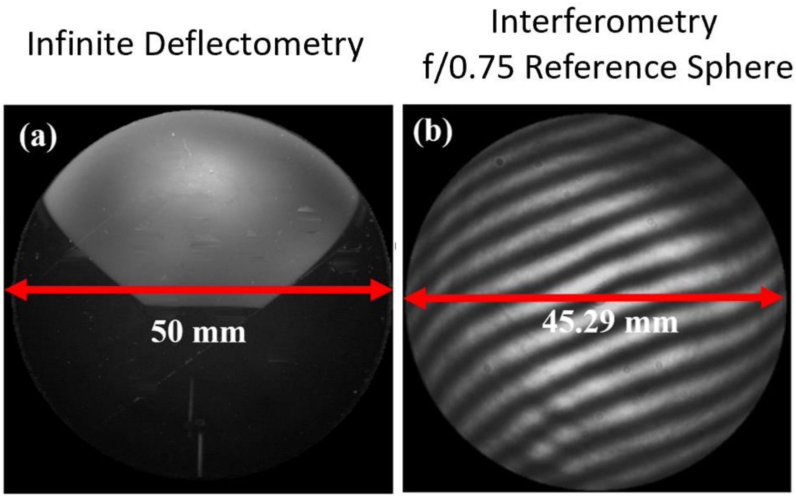

Figure 12. A fast f/1.26 convex sphere measuring 50 mm in diameter was measured using Infinite Deflectometry and interferometry. The Infinite Deflectometry setup measured only a portion of the UUT aperture in the base configuration, demonstrating the need for multiple clocking positions (a). The interferometry used a f/0.75 reference sphere and was able to only measure a 45.29 mm aperture on the UUT (b).

The test of the spherical optic served two primary purposes; determining the effect clocking steps has on reconstruction accuracy and determining in an absolute sense the best possible reconstruction accuracy for the given system. To measure the impact the number of clocking steps has on reconstruction accuracy multiple tests were performed at 6, 45, 90, and 180 clocking positions of the UUT using the Infinite Deflectometry system. Additionally, the 180-clocking position test was used as the best-case performance for the Infinite Deflecomtetry system. This allowed for a verification of the accuracy of surface reconstruction. It should be noted that because the interferometer could only measure a 45.29 mm diameter inner aperture of the UUT, the comparison is only considered for this inner aperture, and not the full 50 mm aperture measured using the Infinite Deflectometry system. Further, piston, tip/tilt, and defocus, corresponding to standard Zernike terms 1:4, were removed from both the interferometric and ID measurements, as neither system as configured can accurately measure these terms. Additionally, comparisons were made after standard Zernike terms 1:6 were removed, after terms 1:21 were removed, and after terms 1:37 were removed. These resulting reconstructed surface maps are referred to as $\mathrm{ID}_{\mathrm{R}}^{1:\mathrm{Z}}$ for the Infinite Deflectometry maps and $\mathrm{INT}^{1:Z}$ for the interferometer measurement maps, where Z refers to the highest number of standard Zernike terms removed and R refers to the number of clocking steps used in the Infinite Deflectometry test. Figure 11 demonstrates the reconstructed Infinite Deflectometry surface maps.

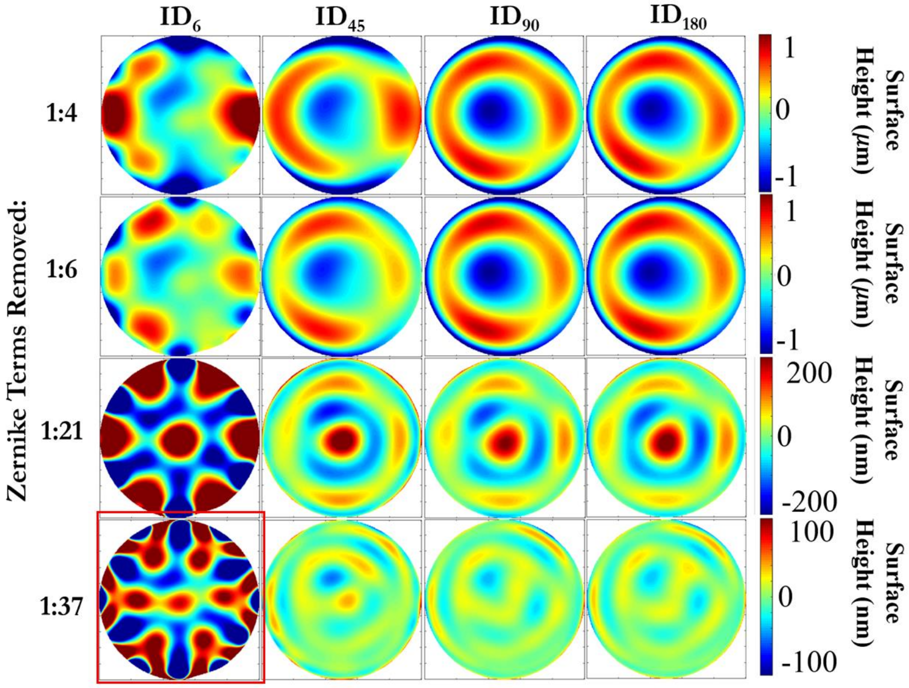

Figure 13. Infinite Deflectometry requires the UUT is clocked through a full 2π rotation. This allows for creating a virtual source enclosure around the UUT, enabling a full aperture surface reconstruction. However, it is important to understand how the number of clocking steps impacts reconstruction. With increasing clocking steps from 6 (left column) up to 180 (right column) there is a significant difference in reconstructed surface. Further, while only removed Zernike terms 1:4 (top row) shows minor difference, with increasing term removal up through 1:37 removed (bottom row) it is evident that too few clocking positions leads to inaccuracies in the reconstructed surface. This is most likely due to stitching errors. This is most apparent for the 6 clocking position case with 37 terms removed, in the bottom left corner.

It is apparent that significant errors in the surface reconstruction are present with too few clocking position steps. This is most likely due to a stitching error. For the case described, the spherical optic exhibits significant non-linear reflecting between the central line of the optic relative to the edges of the testable area. Further, any systematic errors, such as uncertainty in the base position of the camera, UUT, or screen, are known to lead to reconstruction errors. However, such uncertainties typically manifest as tip/tilt or power errors. Thus, the edges of the tested region will exhibit the greatest absolute deviation from the true surface slope. For two sub-aperture maps that are stitched together, this means that there will be a large error between the two overlapping areas, whose magnitude grows as the extent of the stitching area grows. Thus, for the 6 clocking term scenario, there are significant issues across all spatial frequencies, but most important is the obvious six spoke-wheel high frequency pattern, representing the misalignment at the stitching phase of the 6 individual sub-aperture slope maps. This issue is mitigated by using many clocking positions, thereby shrinking the sub-aperture test area and mitigating mis-alignment issues and non-linearity problems. This is apparent as such high-frequency spoke-wheel type errors are not present in the 180-clocking position test.

Considering the best-case performance of the Infinite Deflectometry system as configured, the 180-clocking step test was compared with the interferometry measurement of the UUT. It was important that not only low spatial frequencies, such as coma and trefoil, are accurately reconstructed using Infinite Deflectometry, but also that high spatial frequency features are also measurable, as the surface smoothness can be a key parameter for freeform optics. Figure 12 shows the 180-clocking position reconstruction as well as the interferometry measured surface.

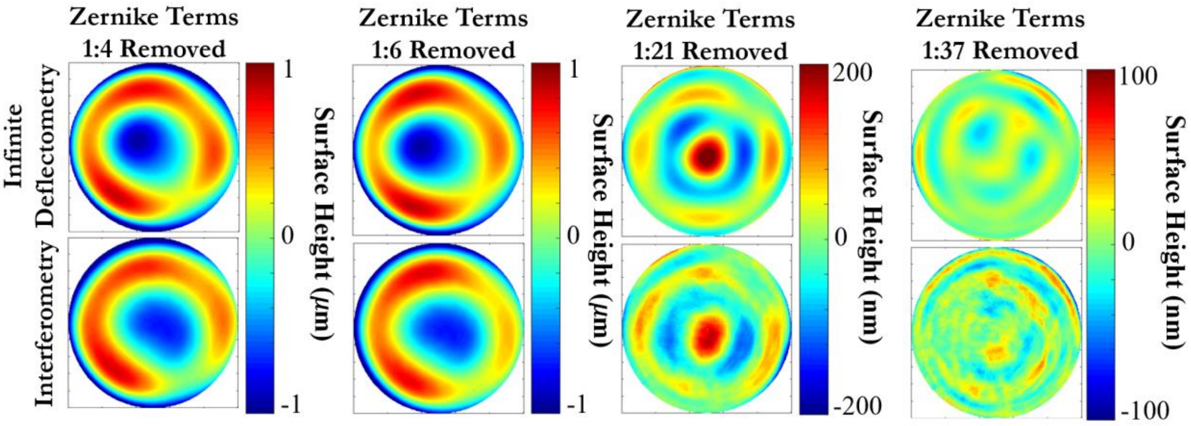

Figure 14. A fast f/1.26 convex spherical optic represents a classically challenging to test convex optic. This surface was measured using an Infinite Deflectometry system with 180 clocking positions (top row), which measured the full 50 mm aperture, as well as using a Zygo Verifire interferometer (bottom row) which measured a limited measurement area of a 45.29 mm diameter aperture on the UUT. Zernike terms 1:4 (1st column column), 1:6 (2nd column), 1:21 (3rd column), and 1:37 (4th column) were removed for both reconstruction maps.

As an additional comparison, the surface sag RMS values of both the Infinite Deflectometry using 180 clocking steps reconstructed maps $\mathrm{ID}_{180}^{1:Z}$, and the interferometric maps, $\mathrm{INT}^{1:Z}$, with Z standard Zernike terms removed, are reported in Table 4. Again, please note that for an accurate and fair comparison, the were only determined over the common 45.29 mm diameter central aperture

Table 4. Surface Sag RMS of 45.29 mm Diameter Central Aperture on f/1.26 50 mm Diameter Convex UUT from ID and INT Surface Sag Maps.

Surface Map	**Surface RMS Zernike Terms 1:4 Removed (nm)**	**Surface RMS Zernike Terms 1:6 Removed (nm)**	**Surface RMS Zernike Terms 1:21 Removed (nm)**	**Surface RMS Zernike Terms 1:37 Removed (nm)**
INT	462.04	447.69	53.71	18.48
ID^{180}	477.34	431.49	56.00	16.26

The $\mathrm{ID}_{180}^{1:Z}$ and $\mathrm{INT}^{1:Z}$ maps are in close agreement across spatial frequencies. For low spatial frequency features there is good agreement. Additionally, as higher terms are removed, as in the $\mathrm{ID}_{180}^{1:37}$ and $\mathrm{ID}_{180}^{1:37}$ cases, there is good agreement, and the RMS surface sag values were within a few nanometers of one another. There are residual differences, however, these are most likely explained by two things. The standard problem of systematic errors arising from uncertainties can affect reconstruction accuracy, and typically most strongly affect low spatial frequency terms. Additionally, the high number of clocking positions and stitching results in several overlapping areas, as well as some minor uncertainty in the rotation stage used, which together result in an apparent smoothing of the reconstructed surface. This is most clear at high spatial frequencies. Lastly, it appears that the Infinite Deflectometry measurement resulted in some smoothing of reconstructed surface features, which may partly result from the stitching process.

2.2.3 Full Aperture Measurement of Highly Freeform Alvarez

An Alvarez is a complex optic which is composed of two complementary phase plates, which are defined by a third order polynomial. By displacing the plates by equal and opposite amounts, defocus can be adjusted, creating a variable power element [43]. The surface of the complementary phase plates can be highly freeform in nature and has presented a particularly challenging surface to both fabricate and measure. Alvarez lens' were invented in the early 1970's, with applications found in visual optics, and more recently have begun to be fabricated over circular apertures [44]. With recent advancements in materials and fabrication processes, particularly CNC diamond turning methods, it is now more feasible to create an Alvarez lens, although, without a custom null CGH, metrology is still quite challenging. Thus, this optic presented an ideal case for testing the capability space of the Infinite Deflectometry system.

To this end, an Alvarez lens was designed and fabricated on a PMMA disk which measured 1 inch in diameter. The optical surface, where the third order polynomial terms were generated, measured only 6 mm in diameter. The optical surface was designed to have 17 µm of Zernike term Z8, which represents horizontal coma, and -17 µm of Zernike term Z10, which represents 45$^{\mathrm{o}}$ trefoil. Only one of the pairs of complementary surfaces was selected for testing. Further, because no custom null existed or could be purchased for measuring the optic, it had been untested since manufacturing. Several attempts were made to obtain an interferometric measurement using a best matching available null optic; however, the fringe density exceeded the capabilities of the available commercial interferometer.

The lens was placed in the Infinite Deflectometry system and measured using 180 clocking positions, after which the surface was reconstructed. The reconstructed surface was compared to the designed theoretical surface. However, the manufacturing process is highly challenging, and the true generated surface potentially deviated significantly from the designed surface. Thus, as an additional reference, a profile of the surface was obtained using a contact-type KLA-Tencor Alpha-Step D-500 profilometer to measure a surface profile of the Alvarez lens. The resulting profile was compared to the same (within a reasonable uncertainty tolerance) profile of the reconstructed surface from the Infinite Deflectometry measurement. For both profiles the mean measurement value was removed to allow for direct comparison.

The resulting reconstructed full aperture surface map of the Alvarez lens optical surface, as well as the design surface, is shown in figure 13. In absolute terms the RMS value with piston, tip/tilt, and power removed was 24.02 μm in the reconstructed surface, as compared to 24.04 μm in the designed surface.

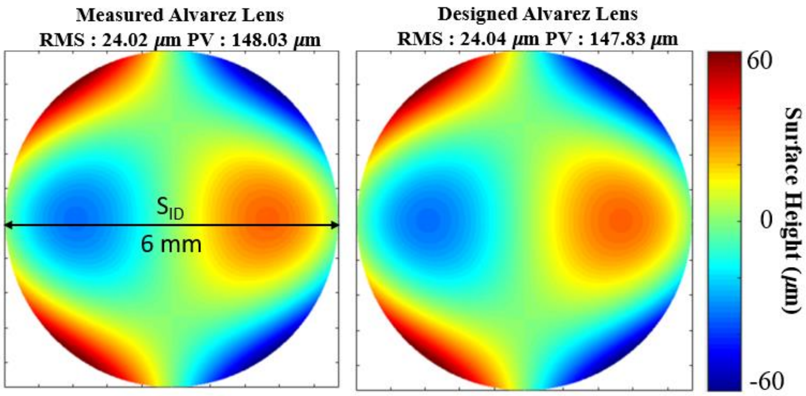

Figure 15. An Alvarez lens is a useful complementary phase plate optic which has a third order polynomial shape imparted on both plates. By displacing one plate relative to the other, defocus can be adjusted. Such an optic was generated on a PMMA plate, with a 6 mm optical aperture. The highly freeform shape was successfully measured using Infinite Deflectometry, and the reconstructed surface (left) was compared to the designed surface (right). It should be noted the extreme shape variation, measuring ~150 *μ*m peak to valley across a small 6 mm aperture made metrology with other techniques such as interferometry impossible without a custom null optic.

Standard Zernike terms 1:37 were fit to the reconstructed surface map and were compared to the designed theoretical Standard Zernike terms. The RMS surface deviation from ideal design was 2.75 µm with Zernike terms 1:4 removed, 1.78 µm with terms 1:8 removed, 178 nm with terms 1:21 removed, and 160 nm with terms 1:37 removed. Figure 14 demonstrates the fit Standard Zernike terms from the reconstructed surface and the designed surface.

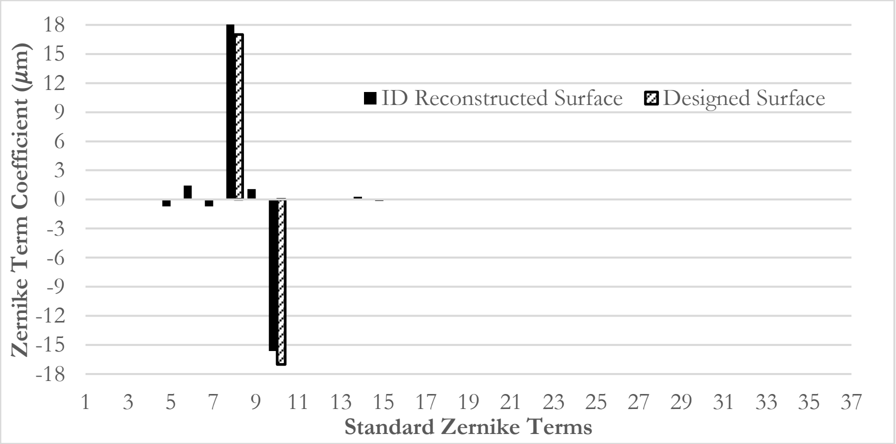

Figure 16. Fitting Zernike terms represents an ideal way to compare the measured surface to the ideal designed surface for an Alvarez lens, which

is designed to have known discrete amounts of third order (Zernike) polynomials. Zernike terms 1:37 were fit to the Infinite Deflectometry (ID) reconstructed surface, and the designed Z8 and Z10 terms are were compared to the measured terms.

The independent verification of the measured surface, as performed by measuring a profile of the surface with a touch profilometer and comparing it to a matching profile from the reconstructed surface map from the Infinite Deflectometry measurement is shown below in figure 15. The absolute surface height of both profiles, as well as the difference between the profiles is shown.

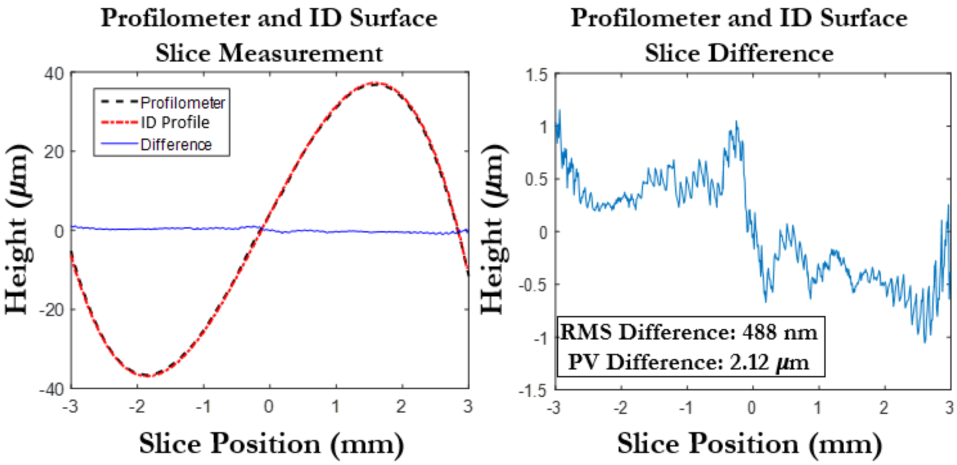

Figure 17. Due to the challenging shape of an Alvarez lens, there is no guarantee that the fabricated surface matches the designed surface. Therefore, guiding metrology is performed during the fabrication period. Thus, as an independent verification a profile of the manufactured Alvarez lens was performed with a touch profilometer and compared to the profile of the Infinite Deflectometry reconstructed surface (left). The absolute difference between the two profiles was also determined (right).

The Infinite Deflectometry system reconstructed surface closely matched the designed surface. Zernike terms Z8 and Z10, the designed third order polynomials used to generate the Alvarez lens, were the most significant terms present in the reconstructed surface. Other minor residual terms, particularly Z5 and Z6, which represent astigmatism, as well as Z9, which represents vertical trefoil, were also present in the final reconstructed surface. It is unclear why the astigmatism persists and may hint at some minor flaw in implementing the Southwell integration, as the removal of tip and tilt in the slope stitching phase should negate astigmatism in the reconstructed map. When compared to the profilometer measurement however, the results were in even closer agreement. The RMS difference between the two profiles, with piston, tip and tilt removed was only 488 nm.

In summary, Infinite Deflectometry was able to extend deflectometry to provide full aperture reconstruction of up to convex optics, both standard and freeform in shape. Importantly, the method can reconstruct the surface including high spatial frequency shapes, which had historically not been possible for a full aperture convex optic deflectometry measurement. This capability greatly improves freeform metrology capabilities by providing an additional metrology tool that can readily measure the increasingly complex surface shapes of freeform optics. Finally, a technique which improves the testing of freeform diffuse (in the visible spectrum) optics is investigated in Section 2.3.

2.3 Time Modulated Infrared Deflectometry

As the use and complexity of optics has grown, the demand for a more efficient fabrication process has also increased. The grinding phase of optics, during which the surface can take on a highly freeform shape as areas are grinded away, presents an ideal convergence period. If properly guided, the total fabrication time of an optic can be significantly reduced. However, during the grinding period, the optical surface is highly diffuse, thus visible light deflectometry, or even visible interferometry, are unable to test the surface. Further, the grinding phase of optics represents only one area of diffuse optics that require testing. New materials and optical designs call for diffuse optical surfaces that must accurately be measured. Infrared deflectometry has, within the past decade, accomplished high accuracy surface measurements of various diffuse optics by using a tungsten ribbon operating as a pseudo-blackbody line scanning source for infrared deflectometry [21,37]. However, a tungsten ribbon type source has power limitations, spatial uncertainty both via mechanical deformation and emission pattern changes, as well as temporal uncertainty.

To address these issues, a long wave infrared temporally modulated integrating cavity (LITMIC) source was developed. The source features and emission area which is stable and known to machining precision, and the spatial emission pattern is highly uniform and temporally stable. The use of a time modulated signal allows for better signal to noise results. Further, the issue of minor fluctuations in the background thermal radiation of a scene, which not only negatively impacts infrared deflectometry of standard optics but has made testing of optics under thermal load impossible, is well handled by the new source. The following Sections 2.3.1-2.3.5 are a summary of an article submitted to the journal Applied Optics, Appendix C.

2.3.1 Infrared Deflectometry Sources

Deflectometry requires a specular reflection to occur at the surface of a tested optic to properly measure the surface. However, many optics have surfaces which do not specularly reflect visible light, which is commonly used not only for deflectometry but for other metrology methods, such as interferometry, as well. Many optics, including freeforms, are fabricated by grinding a base material towards the final desired surface shape with successively finer polishing grits. This process is usually described in two phases: the grinding phase, where the surface roughness can range from hundreds of microns RMS down to ~ 1 µm RMS, and the polishing phase, where super fine polishing tools are used to create a smooth final surface. Traditionally, to test during the grinding phase, a rough surface must be polished and then tested using visible metrology methods. However, the requirement of intermittent polishing between grinding runs greatly extends fabrication time, adding costs and reducing efficiency. Beyond grinding phase optics, there also are a large range of freeform optics which are designed to have rough diffuse surfaces or have coatings or are made from non-specularly reflective materials. One final area of freeform optics which is seeing exponential growth, but where testing still proves challenging, is that of solar collector optics. Many designs call for parabolic trough designs, while others used complex non-axisymmetric collection designs. In either case, the surface of such optics can be diffuse if the material is not coated, and infrared testing can be required. Testing the base shape of such optics is possible with infrared testing. However, testing the shape while under thermal load is historically impossible, as the background radiation can wash out the signal from a test system, and the thermal radiation levels are prone to fluctuate, making removal of background signals impossible.

Early work on infrared deflectometry utilized a line source, made using a heated tungsten ribbon, which was scanned in orthogonal directions, coupled with a long-wave infrared (LWIR) camera. Such a system has been used extensively in freeform testing of diffuse optics [21,37,38,45,46]. However, the tungsten ribbon has some innate physical characteristics which add uncertainty to the test system and limit reconstruction accuracy. The ribbon material can experience large temporal fluctuations, non-uniform spatial emission, and limited power output. Additionally, because the source is a static one with a relatively large thermal mass, it is challenging to accommodate dynamic noise and thermal fluctuations during a test. This presents a serious problem for infrared testing, as all bodies in and out of scene will radiate some infrared light adding to background light levels. However, more challenging is that the radiant flux may change during the test, thereby invalidating the ‘background’ images captured pretest. One example of this is a localized heated ‘tail’ that can be left in the air from the scanning ribbon. Any signals which are not directly from the rectangular emission pattern (if the source is a line source) will lead to inaccuracy in conversion of the raw signal data to screen coordinates, performed using a centroiding process, which will then lead to errors in the surface reconstruction. It is key to note that static shifts which systematically skew the centroid, such as a ‘tail’ or another emission source which doesn’t fluctuate during the test, will add low frequency reconstruction errors, and may be removable via proper calibration. High frequency shifts however, such as those caused by a fluctuating signal from the source, will lead to high spatial frequency reconstruction errors which are difficult to impossible to isolate from a real signal. When considered holistically, because freeform optics are an arbitrary shape, any uncertainty in the reconstruction becomes highly detrimental as it can be impossible to known if the reconstruction is true or has error, and every nanometer is important to guiding and verifying the true freeform shape.

To address both the physical limitations of a traditional infrared deflectometry source, and to expand testing possibilities to more dynamic scenes and surfaces under thermal load, a new source was created which is a long-wave infrared time-modulated integrating cavity (LITMIC) source. The source is an integrating box design which features a precision machine cut emission slit. The geometry of the slit is stable over time, and known to machining precision, and the spatial emission is optimized to be uniform over the slit. Several small resistive heating elements are used to input light into the cavity and offer high temporal stability and a long lifetime (10,000 hours). Most importantly, however, is that the emission is temporally modulating, achieving an 80% contrast ratio at up to 1 Hz. In doing so, active signal isolation can be performed throughout testing, allowing for dynamic removal of background thermal radiation that enters the scene, and therefore providing a higher signal to noise ratio.

The LITMIC source can be created out of any high reflectivity, stable and machinable material. However, for ease of fabrication an aluminum block was used to create the cavity. It should be noted that aluminum does not represent the ideal interior cavity material; instead, a material such as gold or silver, which feature high reflectivity and lower emissivity, would be an ideal material to coat the interior of the box in. LightTools was used to optimize the interior dimensions of the cavity, the heating elements locations, and the interior surface roughness (3.4 μm RMS) to achieve uniform emission at the exit slit, while also achieving non-direction output over roughly 2π steradians. Figure 16 demonstrates the CAD model of the design and the emission pattern as simulated in the LightTools at the exit slit.

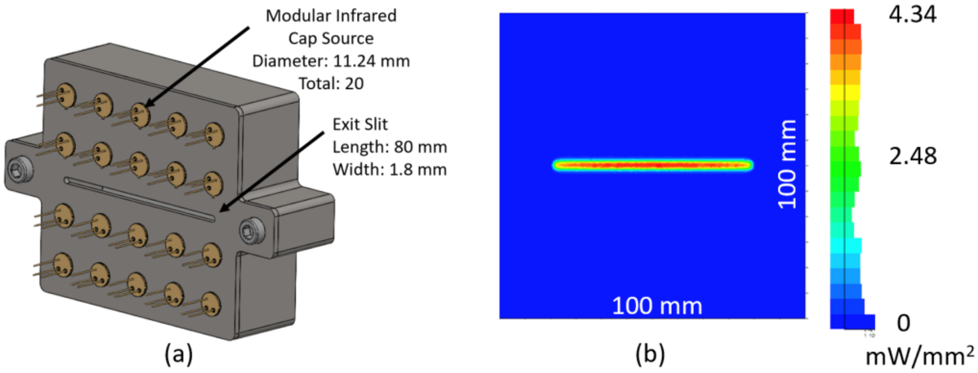

Figure 18. An aluminum integrating box was designed and optimized to make an infrared source. The box was designed to have 20 input source ports, where small, high emissivity, modular and time-modulating infrared cap sources were input in the final built box. An emission exit slit, where light would leave the box, was designed to match the dimensions of a comparison tungsten ribbon infrared source (a). The optimized design was modeled in Light Tools, where the irradiance at the surface of the box was simulated to assure high uniformity across the exit slit (b).

2.3.2 Infrared Deflectometry Sources Radiometric Modeling

The radiometric properties of a traditional tungsten ribbon based source have been well documented [47]. The LITMIC source has similar radiometric properties as a tungsten ribbon, in that both are well described as pseudo-blackbody sources. For the presented study, both sources feature identical emission areas and are linearly scanned, which results in a signal vs. scanning position raw data output from the camera for a test. This raw data is centroided to determine the coordinates of the source which resulted in excitation of a given camera pixel.

As has been described previously [21,48,49], the centroid uncertainty, σ, as determined from error propagation when only noise is considered, is determined from the recorded intensity response width, w, the number of samples taken, N, and the SNR, as shown in equation 1:

$$\sigma = \frac{w}{\sqrt{N}\,SNR} = \frac{w}{\sqrt{N}\;P_{sig}/NEP}, \text{ [1]}$$

Where P_{sig} refers to the signal power and *NEP* is the noise equivalent power. The centroid uncertainty can be directly related to the slope uncertainty, as show in equation 2:

$$\Delta s \cong \frac{\sigma}{2Z}, \text{ [2]}$$

Where Z refers to the distance from the source to the UUT in the test setup. The signal power in equation 1 is determined from the reflected radiance, L_{ref}, the diameter of the camera aperture, D_{ap}, the source width, w_{sc}, and the camera focal length, f, as shown in equation 3:

$$P_{sig} = \tau_o L_{ref} A_{im} \Omega_{pix} = \tau_o L_{ref}\ (w_{sc} D_{ap})\ \frac{A_{pix}}{f^2}, \text{ [3]}$$

Where the reflected radiance, L_{ref}, is determined from the source radiance, L_{src}. The value is scaled by the reflectivity of the UUT, r_U, and the relative reflectance due to rough surface scattering, r_s. The reflected radiance is given by equation 4:

$$L_{ref} = r_a\ r_s\ L_{srce}, \text{ [4]}$$

The source radiance of the tungsten ribbon and LITMIC source are unique to each source. The source radiance of the tungsten ribbon, referred to as $L_{src\_ribbon,}$ is given by equation 5:

$$L_{srce\_ribbon} = \frac{\varepsilon^r\ \alpha^r_{7-14}\ P_{ribbon}}{\pi A_{srce}}, \text{ [5]}$$

Where the total power from the power supply, P_{ribbon}, must be scaled by the emissivity of the source over the given radiation band of 7-14μm, ε_r, which is 0.10 [47,50,51]. As configured for testing, the power draw was approximately 2.1 W (2.2 A, 0.95 V), with an operating temperature of 440 °C. The portion of the total radiation in the 7-14 μm band, referred to as α^r_{7-14}, is determined using the Stefan-Boltzmann law. Finally, the solid angle is calculated from the solid angle a plane source radiates towards a hemisphere, given by $\pi = 3.14\ rad$, while the surface area of the source, A_{src}, is directly taken from the source geometry. While similar in structure, the source radiance of the LITMIC source, $L_{src\_cavity,}$ has some key differences, as shown in equation 6:

$$L_{srce\_cavity} = r_c^b\ \frac{\varepsilon^c\ \alpha^c_{7-14}\ N\ P_{cap}}{\pi A_{srce}}, \text{ [6]}$$

Unlike the tungsten ribbon source, the input power is calculated from the power per cap source, P_{cap}, which for the designed cavity was approximately 0.35 W (23.8 V, 14 mA), with a temperature of 450 °C, and must be scaled by the total number of caps used as inputs into the cavity, N, which for the presented design was 20. The emissivity and radiation are given as ε^c and α_{7-14}^{c} respectively. Lastly, the total output radiance from the cavity must be scaled by the reflectivity of the cavity interior, r_c, which for bare aluminum at the operating temperature is approximately 0.93 [52], for every bounce of a ray. For simplification, the average number of bounces a ray takes from the cap source to exiting the emission slit, given by b, was used to scale the reflectivity. This value was determined for the given design as approximately 46, as calculated in the LightTools model.

It should be noted that the power used for both sources can be scaled using careful engineering, however, there is a fundamental limit to the possible input power. For the tungsten ribbon, the source will fail above a certain power threshold. Below that threshold, as more power is added, the source emission will shift to high energy, resulting in shorter peak wavelength emission, which is non-ideal for rough surface testing. The LITMIC source power can be scaled by increasing the number of input caps used. Again however, above a certain threshold, the input energy will become too great for the interior cavity. Other ways to increase power include improving the interior cavity reflectivity and cooling the interior cavity. The parameter values for the as designed and manufactured LITMIC source, as well the tested tungsten ribbon, are provided in table 5.

Table 5. Source Parameters for Radiometric Modeling of Scanning Line Source Infrared Deflectometry

Parameter	Notation	Value	Unit
Tungsten Ribbon power total consumed	P_{tot}	2.10	W
Single cap power total consumed	P_{cap}	0.35	W
Tungsten Ribbon Radiation in 7-14 um band	α_{7-14}^{r}	0.28	N/A
Cavity Radiation in 7-14 um band	α_{7-14}^{c}	0.28	N/A
Tungsten Ribbon Source Emissivity	ε^r	0.10	N/A
Cavity Source Emissivity	ε^c	0.90	N/A
Cavity Reflectivity (Bare Al)	r_c	0.93	N/A
Cavity average ray bounces	b	46	N/A
Source surface area (for both sources)	A_{src}	1440	mm^2
Ribbon source radiance	$L_{srce\ ribbon}$	1.36×10^{-5}	$\mathrm{W/mm^2/sr}$
Cavity source radiance	$L_{srce\ cavity}$	1.38×10^{-5}	$\mathrm{W/mm^2/sr}$

Finally, please note that fine tuning of the applied power to each source was adjusted in final testing to achieve similar power counts on the camera. This allowed for a more direct one to one comparison of the sources.

2.3.3 Infrared Deflectometry Testing with LITMIC Source

An infrared deflectometry system featuring a long-wave infrared camera and a scanning stage with a source mount that allowed for easy and repeatable mounting was created on an optical bench. A traditional tungsten ribbon source and the LITMIC source described were mounted separately and an infrared deflectometry measurement of several optics was performed with each source. Please note that the radiant flux from both sources was designed to be similar, and fine tuning of the source power was performed to achieve similar counts from the LWIR camera. Further, identical camera settings were used for all measurements. In this way, the infrared deflectometry system and UUT were held identical between the tungsten ribbon and the LITMIC sources.

The optics measured were diffuse optics which could not be tested using visible deflectometry. The first optic was a 2-inch diameter ground glass flat sandblasted with 1500 grit, referred to as Glass^{1500}, while the second optic was a 3-inch diameter aluminum blank, which was tested at room temperature and under thermal load, after the temperature was raised to 150°C, referred to as Al_{Room} and Al_{150} respectively. The surfaces of both optics were measured using a Zygo NewView 8300 Interference Microscope, and the surface roughness of the Glass^{1500} optic was found to be 127.89 nm RM while the Al_{Room} optic had a surface roughness of 102.53 nm RMS.

Five sequential measurements were performed for each optic using each source, and the mean peak signal power recorded from the UUT across the sequential measurements was determined, as well as the standard deviation in peak power across the measurements. The mean peak noise recorded from the background, as well as the standard deviation in peak noise power across the measurements was also determined. Finally, the centroiding repeatability was also calculated and is directly proportional to the signal power standard deviation. For the tungsten ribbon source, several background images were captured prior to turning on the source, and an average background image was determined and subtracted from all subsequent measurement images with the scanning source turned on. For the LITMIC source, several images were captured at each scanning position with the source flickered on and then off, and the ‘off’ images were directly subtracted from their corresponding ‘on’ images. Figure 17 demonstrates the two optics measured using the infrared deflectometry systems.

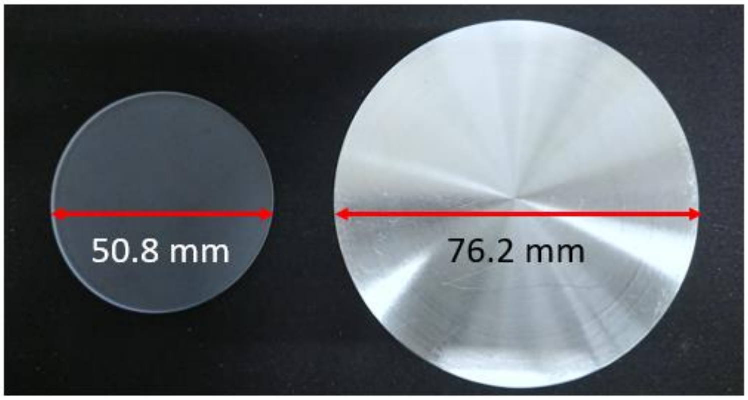

Figure 19. A 2-inch diameter rough ground glass flat, referred to as Glass^{1500}, (left) and bare aluminum flat, referred to as Al_{Room}, (right) were selected for measurement due to their diffuse nature, making infrared deflectometry and ideal metrology method. The surface roughness of both optics was measured using a Zygo NewView 8300 Interference Microscope. The ground glass surface featured a surface roughness of 127.89 nm RMS while the bare aluminum surface roughness was 102.53 nm RMS.

To measure the temporal behavior of both sources a LWIR camera was focused onto the sources. Over a 30-minute period, an image was recorded of both sources every 10 seconds, and the temporal behavior was analyzed. The mean peak power for pixels imaging the sources over the 30-minues was determined, as was the standard deviation in the peak power. Additionally, the mean peak noise and the noise standard deviation over the 30-minute recording interval was determined for both sources.

To measure the spatial emission behavior of the sources, an image of the sources when turned on was captured. A profile across the source was then calculated from the image to analyze the signal power counts.

2.3.4 Source Temporal Stability and Spatial Profile Results

The recorded images of the tungsten ribbon and LITMIC source as captured using a LWIR camera focused onto the source planes is shown in figure 18. The traditional tungsten ribbon source displays a more gaussian profile, with a peak signal near the center. Additionally, two smaller peaks are visible outside of the main ribbon profile which are caused by localized resistive heating in the screws which are used to mount the ribbon. The LITMIC source features more of a flat top profile with fall off near the edges. The edge fall off is expected, as the signal on the detector is the result of a convolution of the rectangular source with the circular camera pupil, therefore some roll on and roll off is expected.

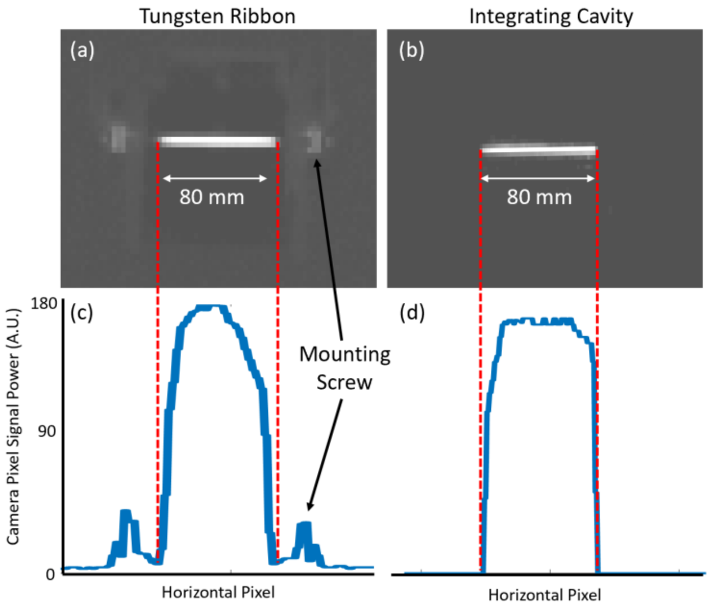

Figure 20. The source geometry is a key parameter in a deflectometry system. For the designed infrared deflectometry test system, and image of the tungsten ribbon (a) as well as the integrating cavity (b) sources was captured using the system camera through focused onto the source through a flat mirror. Observing a profile of the source for the tungsten ribbon (c) and the LITMIC (d) sources, it is seen that the average signal power is similar, but the source profile geometries are quite different, where both should ideally form a flat top rectangular shape.

The average source signal over a 30-minute period as recorded by imaging the tungsten ribbon source and the LITMIC source every 10 seconds is shown in figure 19. It can be observed that the traditional tungsten ribbon source exhibits rapid thermal fluctuations, with a signal standard deviation being 2% of the total peak power, and the peak to valley variation being 12% of the peak power. The LITMIC source exhibits a standard deviation of 0.5% of the total peak power and a peak to valley variation of approximately 2% of the peak power. The noise only fluctuated by ~0.4% of the total peak power.

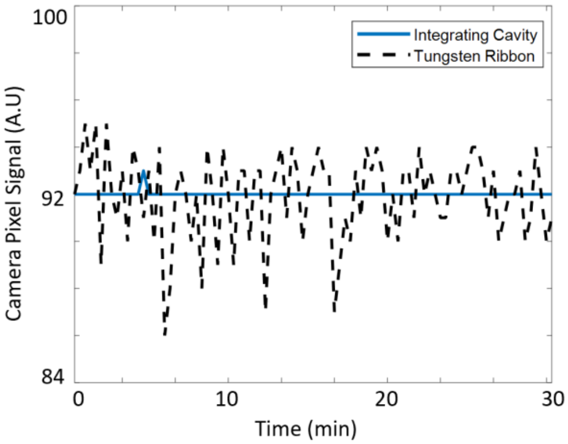

Figure 21. High temporal stability is essential for a deflectometry source, as any fluctuations in the radiant flux directly impacts the recorded power by the camera pixels, which leads to reconstruction error. Over a 30-minute period, with samples taken every 10 seconds, the camera detector pixel signal of the tungsten ribbon source (dotted black line) and the integrating cavity source (solid blue line) were recorded, to determine temporal stability of both sources.

The time averaged camera signal from both sources, referred to as signal$_{\text{time-mean,}}$ along with the standard deviation of the peak signal power, referred to as signal$_{\text{time-std}}$, was calculated from the temporal measurement. Additionally, the peak-to-valley signal value for both sources, referred to as signal$_{\text{PV}}$ was calculated over the 30-minute imaging period. Lastly, the time averaged background signal and the standard deviation over the 30-minute measurement period is also reported for both sources, referred to as noise$_{\text{time-mean}}$ and noise$_{\text{time-std}}$ respectively. The full statistics of the temporal study are provided in table 6.

Table 6. Temporal Stability of Tungsten Ribbon and Integrating Cavity Sources

Source	**signal$_{\text{time-mean}}$ (A.U.)**	**signal$_{\text{time-std}}$ (A.U.)**	**noise$_{\text{time-mean}}$ (A.U.)**	**noise$_{\text{time-std}}$ (A.U.)**	**signal$_{\text{time-PV}}$ (A.U.)**
Tungsten Ribbon	95.72	1.97	72.39	0.45	11.10
LITMIC	93.21	0.53	73.32	0.43	1.82

2.3.5 Testing of Rough Optics with Infrared Deflectometry

To measure the high frequency surface shapes of the tested rough optics the raw output data was processed and used to reconstruct the surface map. Standard Zernike terms 1:37 were removed from all reconstructed maps, allowing for clear observation of only the high spatial frequency terms. Figure 20 shows the reconstructed surface roughness maps of the Glass^{1500}, Al$_{Room}$, and Al$_{150}$ surfaces.

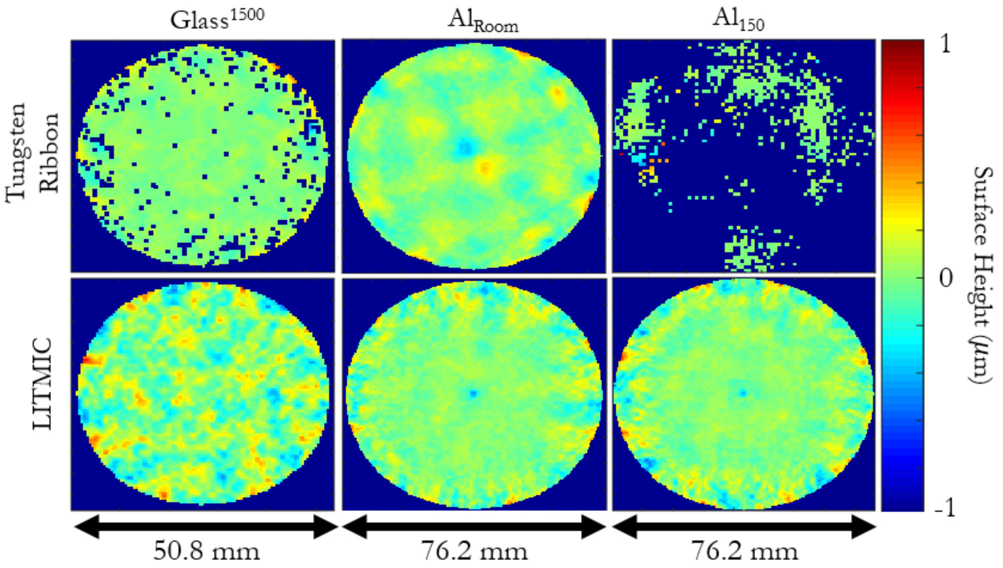

Figure 22. Using both a traditional tungsten ribbon source (top row) and the LITMIC source (bottom row), infrared deflectometry measurements were taken and the surface reconstructed for the Glass^{1500} optic (left column), the Al$_{Room}$ optic (middle column), and the Al$_{150}$ optic (right column). For all maps, Standard Zernike terms 1:37 were removed to observe the surface roughness, as represented by the high spatial frequency terms. NOTE: Missing data regions in the tungsten ribbon reconstructed maps arise from a lack of signal during testing.

The LITMIC source surface reconstruction measured the surface roughness of the Glass^{1500} as 156.63 nm RMS, the Al$_{Room}$ surface roughness as 93.78 nm RMS, and finally the Al$_{150}$ surface roughness as 106.65 nm RMS. The traditional tungsten ribbon surface reconstruction resulted in a surface roughness of the Glass^{1500} surface of 132.33 nm RMS, while the Al$_{Room}$ surface roughness was measured as 95.63 nm RMS. The tungsten ribbon was unable to measure the Al$_{150}$ surface. Figure 21 demonstrates the surface roughness maps of the Glass^{1500} and Al$_{Room}$ optics, as measured using the Zygo NewView 8300 Interference microscope, which measured the surface roughness of the ground glass optic 127.89 nm RMS and the aluminum blank as 102.53 nm RMS.

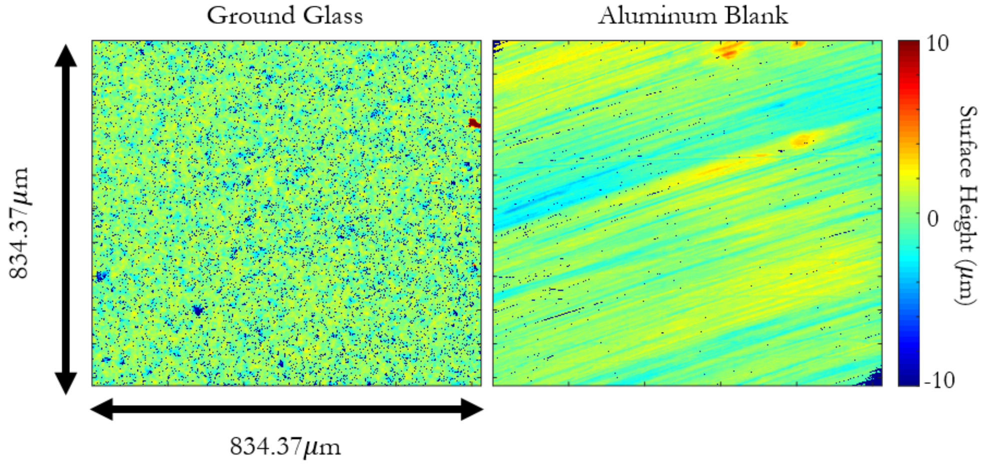

Figure 23. A 2-inch diameter rough ground glass flat, referred to as Glass^{1500}, (left) and bare aluminum flat, referred to as Al$_{\text{Room}}$, (right) surface roughness was measured using a Zygo NewView 8300 Interference Microscope. The ground glass surface featured a surface roughness of 127.89 nm RMS while the bare aluminum surface roughness was 102.53 nm RMS over a small 834×834 μm square area over each optic.

To measure the repeatability of both sources, the statistics across the same pixels imaging both the UUT and the background noise were studied across the N=5 repeat measurements for all optics. As an example, the signal throughout a full scan for all 5 repeat measurements of the aluminum blank using the LITMIC source, as well as the average signal response, is shown in figure 22.

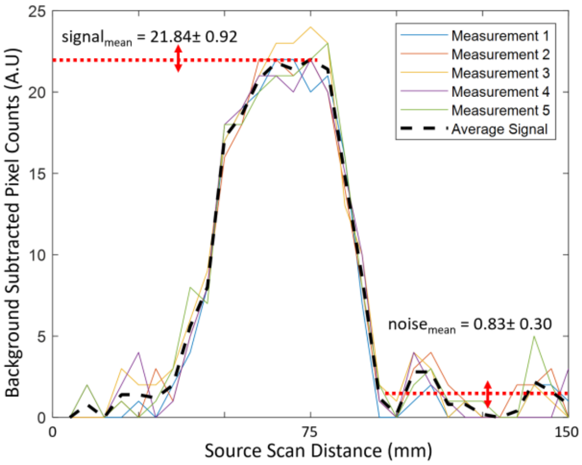

Figure 24. Five repeat measurements were obtained for every source configuration testing every optic. The five repeat camera signals for one pixel imaging the Aluminum blank at room temperature during testing

> using the LITMIC source were plotted, along with the average signal across the five measurements. For this test the mean peak signal recorded was 21.84, with a standard deviation of 0.92, while the mean peak background noise signal was 0.83, with a standard deviation of 0.30.

The full statistics, including the mean peak signal power, the standard deviation of the peak signal power, referred to as $\text{signal}_{\text{mean}}$ and $\text{signal}_{\text{std}}$ respectively, as well as the mean peak noise power and mean peak noise standard deviation, referred to as $\text{noise}_{\text{mean}}$ and $\text{noise}_{\text{std}}$ respectively are provided below in table 7. The average signal to noise ratio, referred to as SNR, and the centroiding error are provided as well.

Table 7. Source signal and reconstruction statistics using tungsten ribbon and LITMIC sources.

Source	**Optic**	**$\text{signal}_{\text{mean}}$ ± $\text{signal}_{\text{std}}$ (A.U.)**	**$\text{noise}_{\text{mean}}$ ± $\text{noise}_{\text{std}}$ (A.U.)**	**SNR**	**Centroiding Error (scam step size)**
Tungsten Ribbon	Glass^{1500}	4.68±1.92	1.28 ±0.44	3.66	3.15
LITMIC	Glass^{1500}	5.32±0.94	0.70±0.26	7.60	0.75
Tungsten Ribbon	Al_{Room}	22.68±1.17	4.74±0.27	4.78	2.25
LITMIC	Al_{Room}	21.84±0.92	0.85±0.30	25.69	0.67
LITMIC	Al_{150}	18.44±0.81	0.89±0.27	20.71	0.68

While the LITMIC source and the traditional tungsten ribbon displayed similar peak signal power for all tests, the standard deviation of the signal power was significantly different. Like the temporal measurement, the LITMIC source resulted in a significantly smaller standard deviation in peak source power across the five repeat measurements when compared to the tungsten ribbon. Further, due to the unique signal isolation capability afforded by the temporal modulation of the LITMIC source, the SNR of the LITMIC source was 2-5 times larger than the tungsten ribbon. Finally, the LITMIC source resulted in a centroiding uncertainty that was approximately 1.5 mm, while the traditional tungsten ribbon source had a centroiding uncertainty of 4-6 mm.

The temporally modulated LITMIC source demonstrates that the fundamental nature of the source provides improved emission properties, both in terms of spatial uniformity and temporal stability.

Additionally, the temporal modulation not only improves the signal-to-noise ratio for testing but allows for testing optics under thermal load or in scenes where there may be background radiation fluctuations. This can be essential for measuring freeform optics which are expected to operate in a high-temperature environment, such as solar collectors.

It should be noted that the LITMIC source tested was not optimized from an engineering perspective. By coating the interior of the cavity to achieve higher reflectivity and lower emissivity, the output signal will be larger. Further, cooling the interior of the cavity using a Peltier cooler is worth exploring to maximize contrast between the on and off states of the cavity. However, overall the LITMIC source promises to expand freeform testing of diffuse rough surface optics.

3. Concluding Remarks

Extensive work was performed to introduce a reliable reconstruction method for deflectometry testing of surfaces where an accurate surface map is unavailable. As discussed, this can be an issue in the optics fabrication process, during which the surface shape may change rapidly and in a truly freeform way between grinding runs. Additionally, there may be situations in which there is no access to the ideal freeform shape of a fabricated optic, and thus some method to calculate an accurate surface map is required. The model-free iterative deflectometry algorithmic approach provides a solution for such cases. Modeling was performed which verified that with no systematic error, the model-free approach is limited by machine precision in reconstruction accuracy. When normal loose calibration methods are considered in the simulation, modeling for tens of microns of positioning error and milliradians of tilt in all system components, the uncertainty in reconstruction of the surface increased to what was experimentally observed. Finally, a complex freeform optic, which had a spiral pattern imparted on a base sphere, was measured and reconstructed using the model-free method. The results demonstrated that for a freeform surface, the reconstruction accuracy using the model-free iterative deflectometry algorithm was more similar to an interferometric measurement of the same optic than even a traditional best fit sphere model reconstruction. This suggests that particularly for freeform optics, if an exact surface map of the ideal surface is unavailable, the model-free technique can be highly useful.

While the model-free iterative deflectometry was verified by testing a concave surface, the infinite deflecomtetry method expanded deflectometry to testing up to and including highly convex freeform surfaces. Historically, deflectometry was an ideal method for freeform testing of concave optics as a near one-to-one imaging condition could be achieved by placing the camera and source near the center of curvature of an optic, thereby requiring a small source area to test even a large optic. However, such an approach is impossible for a convex optic, where the center of curvature can be in virtual space. The infinite deflectometry system creates a virtual 2π -steradian measurement volume around the unit under test. In this way, a high accuracy deflectometry test can be performed for any optical surface shape, so long as the surface can be seen by the camera in the test. The method relies on using a high-resolution screen tilted over the optic, with a camera positioned above the optic. By rotating the optic, a virtual source is created at each clocking position. The local slope maps of sub-aperture areas are calculated using each virtual source, resulting in a full aperture local slope map of the optic. The method was used to measure a fast (f/1.26) convex sphere and resulted in a surface reconstruction highly similar to an interferometric measurement of the same optic. Further, the high-spatial frequency terms were well matched between the test methods, suggesting that infinite deflectometry can provide optical quality testing of convex optics. To explore the freeform testing capabilities of the method, an Alvarez lens as measured. The lens was highly freeform and had steep surface slopes, featuring nearly 150 μm peak-to-valley of coma and trefoil across a 6 mm clear aperture. Such surfaces are finding increased usage as when two complementary pairs are shifted relative to one another, they can induce defocus, acting as a variable focus lens system. However, they are extremely difficult to measure, as they have high freeform departure and can be very small. The infinite deflectometry system successfully measured the optic, and the reconstructed surface showed similar surface shape to the designed shape. As a complementary test, a profile of the surface was measured using a touch profilometer, and the profile of the reconstructed surface showed very close match to the profilometry measurement, with only 488 nm RMS of difference between the two profiles after piston, tip/tilt, and power were removed from the reconstructed surface. This suggests that infinite deflectometry could be a powerful deflecomtetry configuration for performing full aperture surface reconstruction measurements of highly freeform optics, as well as flat and convex optics.

Finally, a temporally modulated infrared source for deflectometry of rough, non-specularly reflective surfaces was explored. This work sought to address the need for improved geometry of a source emission, as well as more temporally stable emission in a scanning source, as compared to a traditional tungsten ribbon source. The newly created source, which was a long-wave infrared temporally modulated integrating cavity, or LITMIC for short, was created from an aluminum chunk, and utilized several resistive elements as light inputs into the cavity, which had a rectangular slit machine cut where the light was uniformly emitted over approximately a full hemisphere. Most importantly, the LITMIC source was temporally modulated, with an 80% contrast ratio at 1 Hz modulation. This feature allowed for signal isolation leading to an improved signal-to-noise ratio in testing rough surfaces. The temporal modulation also allows for dynamic in scene background accommodation, as a new background image can be easily and quickly collected for every scanning position of the source. A LightTools model was created to optimize the LITMIC cavity design and surface roughness, as well as the source input positions, to create a uniform emission profile over the exit slit. Temporal stability over a 30-minute imaging period demonstrated extremely stable power output from the LITMIC source, while a profile of the source, as imaged by a long wave infrared camera, well matched the expected flat top shape for a rectangular source imaged by a circular pupil. The LITMIC source was able to repeatably measure a rough ground glass optical surface as well as an aluminum blank and had better signal-to-noise ratios and smaller signal standard deviation over repeat measurements when compared to a traditional tungsten ribbon source. Finally, the LITMIC source produced a first of its kind infrared deflectometry measurement of an aluminum blank under thermal load, which not only had high thermal emissions but also was not stable during testing.

These results offer several avenues for interesting future work. A well calibrated deflectometry system should be created and used to test both a standard and a highly freeform optic, and the surface should then be reconstructed using the model-free iterative deflectometry method to determine the true fundamental accuracy of the method. Additionally, work should be done to determine the lower limit of seed points from the UUT surface required to avoid entering a null space in the surface reconstruction. Currently, the piston of one point on the true UUT surface, measured by a known camera pixel, must be input to the MID processing method. In doing so, the piston of the reconstructed surface is bound, which limits the solution space and helps to avoid multiple valid solutions that are all valid reconstruction surfaces. However, it has not been verified that only bounding the piston is satisfactory to avoid having more than one viable solution. For example, because there is some positioning uncertainty of the UUT location in x, y, z and tip and tilt, even with piston bound, there can be cases where two entirely unique reconstructed surfaces equally would satisfy the measured surface slopes and piston provided. In this scenario, the MID method would still converge to a solution, but there is a possibility that the solution it converged to is entirely unique and different from the real surface, and the user would be unaware of this issue. Modeling and simulations should be performed to determine what is the fundamental constraint limit required to avoid entering a null space. For the infinite deflectometry system it is apparent that the stitching of local slope maps leads to some error in reconstruction, and the current stitching method requires removal of some features in the measured data. A more refined stitching method should be investigated that leads to improved reconstruction results while retaining the fundamental measurement information. Additionally, it was found that particularly for convex optics, some light from a polarized screen will strike the optic under test at Brewster's angle. This could lead to significantly improved calibration and local accurate knowledge of the surface slope.

This topic should be explored further. Lastly, a more robust rotational calibration method should be created for the infinite deflectometry measurement to reduce systematic errors. For the LITMIC source, the upper limits of testable roughness should be explored. This will require engineering improvements to the source, including improved interior cavity reflectivity, which can be achieved by coating the cavity with a high reflectivity material. It was also noticed that the interior cavity radiated some latent light, thus, cooling the cavity, perhaps using a Peltier cooler, would improve contrast and lead to high signal-to-noise ratios. Finally, larger input source power could be introduced by adding sources. With these improvements in mind, a library of materials and surface roughness testable with the source should then be explored. One additional area of interest is exploiting the machine nature of the LITMIC source, which need not be a box cavity with a rectangular emission slit. The emission profile could be custom designed, such that emission port could allow for a phase-shifting infrared measurement.

References

1. D. Cheng, Y. Wang, H. Hua, and M. M. Talha, "Design of an optical see-through head-mounted display with a low f-number and large field of view using a freeform prism," Appl. Opt., AO **48**, 2655–2668 (2009).

2. K. Wang, F. Chen, Z. Liu, X. Luo, and S. Liu, "Design of compact freeform lens for application specific light-emitting diode packaging," Opt. Express, OE **18**, 413–425 (2010).

3. B. Martin, J. Burge, S. Miller, S. Warner, and C. Zhao, "Fabrication and Testing of 8.4 m Off-Axis Segments for the Giant Magellan Telescope," in (Optical Society of America, 2008), p. OWD6.

4. H. M. Martin, R. G. Allen, J. H. Burge, J. M. Davis, W. B. Davison, M. Johns, D. W. Kim, J. S. Kingsley, K. Law, R. D. Lutz, P. A. Strittmatter, P. Su, M. T. Tuell, S. C. West, and P. Zhou, "Production of primary mirror segments for the Giant Magellan Telescope," in *Advances in Optical and Mechanical Technologies for Telescopes and Instrumentation* (International Society for Optics and Photonics, 2014), Vol. 9151, p. 91510J.

5. M. Dimmler, P. Barriga, M. Cayrel, F. Derie, A. Foerster, F. Gonte, J. C. Gonzalez, L. Jochum, N. Kornweibel, S. Leveque, C. Lucuix, and L. Pettazzi, "Getting ready for serial production of the segmented 39-meter ELT primary: status, challenges and strategies," in *Ground-Based and Airborne Telescopes VII* (International Society for Optics and Photonics, 2018), Vol. 10700, p. 1070043.

6. D. Crampton and B. Ellerbroek, "Design and development of TMT," International Astronomical Union. Proceedings of the International Astronomical Union; Cambridge **1**, 410–419 (2005).

7. A. Tritschler, T. R. Rimmele, S. Berukoff, R. Casini, J. R. Kuhn, H. Lin, M. P. Rast, J. P. McMullin, W. Schmidt, F. Wöger, and D. Team, "Daniel K. Inouye Solar Telescope: High-resolution observing of the dynamic Sun," Astronomische Nachrichten **337**, 1064–1069 (2016).

8. T. Blalock, K. Medicus, and J. D. Nelson, "Fabrication of freeform optics," in *Optical Manufacturing and Testing XI* (International Society for Optics and Photonics, 2015), Vol. 9575, p. 95750H.

9. M. Beier, S. Scheiding, A. Gebhardt, R. Loose, S. Risse, R. Eberhardt, and A. Tünnermann, "Fabrication of high precision metallic freeform mirrors with magnetorheological finishing (MRF)," in *Optifab 2013* (International Society for Optics and Photonics, 2013), Vol. 8884, p. 88840S.

10. C. Gray, I. Baker, G. Davies, R. Evans, N. Field, T. Fox-Leonard, W. Messelink, J. Mitchell, P. Rees, S. Waine, D. D. Walker, and G. Yu, "Fast manufacturing of E-ELT mirror segments using CNC polishing," in *Optical Manufacturing and Testing X* (International Society for Optics and Photonics, 2013), Vol. 8838, p. 88380K.

11. D. D. Walker, D. Brooks, A. King, R. Freeman, R. Morton, G. McCavana, and S.-W. Kim, "The 'Precessions' tooling for polishing and figuring flat, spherical and aspheric surfaces," Opt. Express, OE **11**, 958–964 (2003).

12. S. C. West, R. Angel, B. Cuerden, W. Davison, J. Hagen, H. M. Martin, D. W. Kim, and B. Sisk, "Development and Results for Stressed-lap Polishing of Large Telescope Mirrors1," in *Classical Optics 2014 (2014), Paper OTh2B.4* (Optical Society of America, 2014), p. OTh2B.4.

13. B. G. Assefa, M. Pekkarinen, H. Partanen, J. Biskop, J. Turunen, and J. Saarinen, "Imaging-quality 3D-printed centimeter-scale lens," Opt. Express, OE **27**, 12630–12637 (2019).

14. I. Trumper, B. T. Jannuzi, and D. W. Kim, "Emerging technology for astronomical optics metrology," Optics and Lasers in Engineering **104**, 22–31 (2018).

15. M. B. Dubin, P. Su, and J. H. Burge, "Fizeau interferometer with spherical reference and CGH correction for measuring large convex aspheres," in (2009), Vol. 7426, pp. 74260S-74260S–10.

16. S. Scheiding, M. Beier, U.-D. Zeitner, S. Risse, and A. Gebhardt, "Freeform mirror fabrication and metrology using a high performance test CGH and advanced alignment features,"

in *Advanced Fabrication Technologies for Micro/Nano Optics and Photonics VI* (International Society for Optics and Photonics, 2013), Vol. 8613, p. 86130J.

17. R. Huang, P. Su, T. Horne, G. B. Zappellini, and J. H. Burge, "Measurement of a large deformable aspherical mirror using SCOTS (Software Configurable Optical Test System)," in *Optical Manufacturing and Testing X* (International Society for Optics and Photonics, 2013), Vol. 8838, p. 883807.

18. R. Huang, P. Su, J. H. Burge, L. Huang, and M. Idir, "High-accuracy aspheric x-ray mirror metrology using Software Configurable Optical Test System/deflectometry," OE, OPEGAR **54**, 084103 (2015).

19. W. H. Southwell, "Wave-front estimation from wave-front slope measurements," J. Opt. Soc. Am., JOSA **70**, 998–1006 (1980).

20. R. Huang, "High Precision Optical Surface Metrology using Deflectometry," (2015).

21. T. Su, S. Wang, R. E. Parks, P. Su, and J. H. Burge, "Measuring rough optical surfaces using scanning long-wave optical test system. 1. Principle and implementation," Appl. Opt., AO **52**, 7117–7126 (2013).

22. E. Olesch, C. Faber, and G. Häusler, "Deflectometric Self-Calibration for arbitrary specular surfaces," DGaO-Proceedings. Online journal **112**, 2 (n.d.).

23. T. Zhou, K. Chen, H. Wei, and Y. Li, "Improved method for rapid shape recovery of large specular surfaces based on phase measuring deflectometry," Appl. Opt., AO **55**, 2760–2770 (2016).

24. H. Zhang, S. Han, S. Liu, S. Li, L. Ji, and X. Zhang, "3D shape reconstruction of large specular surface," Appl. Opt., AO **51**, 7616–7625 (2012).

25. W. Zhao, L. R. Graves, R. Huang, W. Song, and D. Kim, "Iterative surface construction for blind deflectometry," in *8th International Symposium on Advanced Optical Manufacturing and Testing Technologies: Optical Test, Measurement Technology, and Equipment* (International Society for Optics and Photonics, 2016), Vol. 9684, p. 96843X.

26. S. Chen, S. Xue, Y. Dai, and S. Li, "Subaperture stitching test of convex aspheres by using the reconfigurable optical null," Optics & Laser Technology **91**, 175–184 (2017).

27. Y. Chen, E. Miao, Y. Sui, and H. Yang, "Modified Sub-aperture Stitching Algorithm using Image Sharpening and Particle Swarm Optimization," J. Opt. Soc. Korea, JOSK **18**, 341–344 (2014).

28. Y.-C. Chen, C.-W. Liang, H.-S. Chang, and P.-C. Lin, "Reconstruction of reference error in high overlapping density subaperture stitching interferometry," Opt. Express, OE **26**, 29123–29133 (2018).

29. L. Zhang, D. Liu, T. Shi, Y. Yang, S. Chong, B. Ge, Y. Shen, and J. Bai, "Aspheric subaperture stitching based on system modeling," Opt. Express, OE **23**, 19176–19188 (2015).

30. C. J. Oh, A. E. Lowman, M. Dubin, G. Smith, E. Frater, C. Zhao, and J. H. Burge, "Modern technologies of fabrication and testing of large convex secondary mirrors," in *Advances in Optical and Mechanical Technologies for Telescopes and Instrumentation II* (International Society for Optics and Photonics, 2016), Vol. 9912, p. 99120R.

31. Z. Tian, W. Yang, Y. Sui, Y. Kang, W. Liu, and H. Yang, "A high-accuracy and convenient figure measurement system for large convex lens," Opt. Express, OE **20**, 10761–10775 (2012).

32. C. J. Oh, A. E. Lowman, G. A. Smith, P. Su, R. Huang, T. Su, D. Kim, C. Zhao, P. Zhou, and J. H. Burge, "Fabrication and testing of 4.2m off-axis aspheric primary mirror of Daniel K. Inouye Solar Telescope," ADVANCES IN OPTICAL AND MECHANICAL TECHNOLOGIES FOR TELESCOPES AND INSTRUMENTATION II (2016).

33. J. Balzer, D. Acevedo-Feliz, S. Soatto, S. Höfer, M. Hadwiger, and J. Beyerer, "Cavlectometry: Towards Holistic Reconstruction of Large Mirror Objects," arXiv:1409.4095 [cs] (2014).

34. P. Candry and B. Maximus, "Projection displays: New technologies, challenges, and applications," Journal of the Society for Information Display **23**, 347–357 (2015).

35. J.-W. Huang, "Design and Fabrication of Ultra-Short Throw Ratio Projector Based on Liquid Crystal on Silicon," Liquid Crystals - Recent Advancements in Fundamental and Device Technologies (2018).

36. H. B. Kulkarni, "Design and Development of Prototype Cylindrical Parabolic Solar Collector for Water Heating Application," International Journal of Renewable Energy Development; Semarang **5**, 49–55 (2016).

37. C. J. Oh, A. E. Lowman, G. A. Smith, P. Su, R. Huang, T. Su, D. Kim, C. Zhao, P. Zhou, and J. H. Burge, "Fabrication and testing of 4.2m off-axis aspheric primary mirror of Daniel K. Inouye Solar Telescope," in *Advances in Optical and Mechanical Technologies for Telescopes and Instrumentation II* (International Society for Optics and Photonics, 2016), Vol. 9912, p. 99120O.

38. D. W. Kim, T. Su, P. Su, C. Oh, L. Graves, and J. Burge, "Accurate and rapid IR metrology for the manufacture of freeform optics | SPIE Homepage: SPIE," http://www.spie.org/newsroom/6015-accurate-and-rapid-ir-metrology-for-the-manufacture-of-freeform-optics?SSO=1.

39. "B. Delaunay, "Sur la sphère vide. A la mémoire de Georges Voronoï", Bulletin de l'Académie des Sciences de l'URSS. Classe des sciences mathématiques et na, 1934, no. 6, 793–800," http://www.mathnet.ru/php/archive.phtml?wshow=paper&jrnid=im&paperid=4937&option_lang=eng.

40. T. Möller and B. Trumbore, "Fast, Minimum Storage Ray-Triangle Intersection," Journal of Graphics Tools **2**, 21–28 (1997).

41. P. A. Lightsey, C. B. Atkinson, M. C. Clampin, and L. D. Feinberg, "James Webb Space Telescope: large deployable cryogenic telescope in space," OE, OPEGAR **51**, 011003 (2012).

42. C. J. Evans, R. J. Hocken, and W. T. Estler, "Self-Calibration: Reversal, Redundancy, Error Separation, and 'Absolute Testing,'" CIRP Annals **45**, 617–634 (1996).

43. M. Bawart, A. Jesacher, S. Bernet, and M. Ritsch-Marte, "Remote focusing in confocal microscopy by means of a modified Alvarez lens," Journal of Microscopy **271**, 337–344 (2018).

44. I. M. Barton, S. N. Dixit, L. J. Summers, C. A. Thompson, K. Avicola, and J. Wilhelmsen, "Diffractive Alvarez lens," Opt. Lett., OL **25**, 1–3 (2000).

45. D. W. Kim, C. Oh, A. Lowman, G. A. Smith, M. Aftab, and J. H. Burge, "Manufacturing of super-polished large aspheric/freeform optics," in (2016), Vol. 9912, pp. 99120F-99120F–9.

46. T. Su, S. Wang, R. E. Parks, P. Su, and J. H. Burge, "Measuring rough optical surfaces using scanning long-wave optical test system. 1. Principle and implementation," Appl. Opt., AO **52**, 7117–7126 (2013).

47. T. Su, "Asphercial Metrology for Non-Specular Surfaces with the Scanning Long-Wave Optical Test System," (2014).

48. P. R. Bevington and D. K. Robinson, *Data Reduction and Error Analysis for the Physical Sciences* (McGraw-Hill, 2003).

49. J. S. Morgan, D. C. Slater, J. G. Timothy, and E. B. Jenkins, "Centroid position measurements and subpixel sensitivity variations with the MAMA detector," Appl. Opt., AO **28**, 1178–1192 (1989).

50. J. C. De Vos, "A new determination of the emissivity of tungsten ribbon," Physica **20**, 690–714 (1954).

51. V. D. Dmitriev and G. K. Kholopov, "Radiant emissivity of tungsten in the infrared region of the spectrum," J Appl Spectrosc **2**, 315–320 (1965).

52. K. Ujihara, "Reflectivity of Metals at High Temperatures," Journal of Applied Physics **43**, 2376–2383 (1972).

53. D. W. Kim, H. M. Martin, and J. H. Burge, "Calibration and optimization of computer-controlled optical surfacing for large optics," in *Optical Manufacturing and Testing IX* (International Society for Optics and Photonics, 2011), Vol. 8126, p. 812615.

54. D. W. Kim, J. H. Burge, J. M. Davis, H. M. Martin, M. T. Tuell, L. R. Graves, and S. C. West, "New and improved technology for manufacture of GMT primary mirror segments," in

Advances in Optical and Mechanical Technologies for Telescopes and Instrumentation II (International Society for Optics and Photonics, 2016), Vol. 9912, p. 99120P.

55. P. Zhou, H. Martin, C. Zhao, and J. H. Burge, "Mapping Distortion Correction for GMT Interferometric Test," in *Imaging and Applied Optics Technical Papers (2012), Paper OW3D.2* (Optical Society of America, 2012), p. OW3D.2.

56. R. Geyl, D. Bardon, R. Bourgois, N. Ferachoglou, E. Harel, and C. Couteret, "First steps in ELT optics polishing," in *Fifth European Seminar on Precision Optics Manufacturing* (International Society for Optics and Photonics, 2018), Vol. 10829, p. 1082904.

57. U. Mueller, "Production metrology design and calibration for TMT primary mirror fabrication used at multiple manufacturing sites," in *Ground-Based and Airborne Telescopes VI* (International Society for Optics and Photonics, 2016), Vol. 9906, p. 99060Z.

58. M. Sieger, F. Balluff, X. Wang, S.-S. Kim, L. Leidner, G. Gauglitz, and B. Mizaikoff, "On-Chip Integrated Mid-Infrared GaAs/AlGaAs Mach–Zehnder Interferometer," Anal. Chem. **85**, 3050–3052 (2013).

59. H. Yoo, G. A. Smith, C. J. Oh, A. E. Lowman, and M. Dubin, "Improvements in the scanning long-wave optical test system," in *Optical Manufacturing and Testing XII* (International Society for Optics and Photonics, 2018), Vol. 10742, p. 1074216.

60. L. R. Graves, H. Quach, H. Choi, and D. W. Kim, "Infinite deflectometry enabling 2π-steradian measurement range," Opt. Express, OE **27**, 7602–7615 (2019).

61. W. H. Southwell, "Wave-front estimation from wave-front slope measurements," J. Opt. Soc. Am., JOSA **70**, 998–1006 (1980).

62. M. Aftab, J. H. Burge, G. A. Smith, L. Graves, C. Oh, and D. W. Kim, "Chebyshev gradient polynomials for high resolution surface and wavefront reconstruction," in *Optical Manufacturing and Testing XII* (International Society for Optics and Photonics, 2018), Vol. 10742, p. 1074211.

63. S. Höfer, J. Burke, and M. Heizmann, "Infrared deflectometry for the inspection of diffusely specular surfaces," Advanced Optical Technologies **5**, 377–387 (2016).

64. T. Su, W. H. Park, R. E. Parks, P. Su, and J. H. Burge, "Scanning Long-wave Optical Test System: a new ground optical surface slope test system," in *Optical Manufacturing and Testing IX* (International Society for Optics and Photonics, 2011), Vol. 8126, p. 81260E.

APPENDIX A

Model-free Deflectometry for Freeform Optics Measurement Using an Iterative Reconstruction Technique

Logan Rodriguez Graves, Heejoo Choi, Wenchuan Zhao,
Chang Jin Oh, Peng Su, Tianquan Su, and Dae Wook Kim

Copyright Transfer Agreement

2110 Vol. 43, No. 9 / 1 May 2018 / *Optics Letters* Letter

Optics Letters

Model-free deflectometry for freeform optics measurement using an iterative reconstruction technique

Logan R. Graves,[1] Heejoo Choi,[1] Wenchuan Zhao,[2] Chang Jin Oh,[1] Peng Su,[3] Tianquan Su,[4] and Dae Wook Kim[1,5,*]

[1]*College of Optical Sciences, University of Arizona, 1630 E. University Blvd., Tucson, Arizona 85721, USA*
[2]*The Institute of Optics and Electronics, Chinese Academy of Sciences, Chengdu 610209, China*
[3]*ASML Corporation, 77 Danbury Road, Wilton, Connecticut 06897, USA*
[4]*KLA-Tencor Corporation, 3 Technology Dr., Miltipas, California 95035, USA*
[5]*Steward Observatory, University of Arizona, 933 N. Cherry Ave., Tucson, Arizona 85719, USA*
**Corresponding author: letter2dwk@hotmail.com*

Received 26 February 2018; revised 27 March 2018; accepted 29 March 2018; posted 30 March 2018 (Doc. ID 324660); published 26 April 2018

We present a novel model-free iterative data-processing approach that improves surface reconstruction accuracy for deflectometry tests of unknown surfaces. This new processing method iteratively reconstructs the surface, leading to reduced error in the final reconstructed surface. The method was implemented in a deflectometry system, and a freeform surface was tested and compared to interferometric test results. The reconstructed departure from interferometric results was reduced from 15.80 μm RMS with model-based deflectometry down to 5.20 μm RMS with the iterative technique reported here.

OCIS codes: (120.0120) Instrumentation, measurement, and metrology; (120.6650) Surface measurements, figure; (120.4640) Optical instruments.

https://doi.org/10.1364/OL.43.002110

With ever-growing improvements in freeform optical fabrication, there is a high demand for accurate and dynamic metrology systems. Deflectometry and interferometry are two popular optical test methods that provide high accuracy surface metrology of a unit under test (UUT) [1,2]. Interferometric testing requires a null setup to obtain accurate results. For testing freeform surfaces or highly aspheric surfaces, the interferometer requires a null-optic, such as a computer-generated hologram (CGH) [3]. However, such null optics can be expensive and only work for one configuration.

Deflectometry is a non-null test method that has been shown to provide surface reconstruction accuracy similar to commercial interferometric systems for spherical, aspheric, and off-axis optics [4–6]. The measurable UUT surface area and slope range, referred to as the dynamic range, directly depend on the system hardware configuration. A deflectometry system uses a source which illuminates a UUT and the reflected rays are recorded by a camera. If a clear line of sight can be made from a camera pixel to the UUT surface area (mapped on the camera detector) to a point within the source area (limited by source extent), obeying the law of reflection, it is within the testable dynamic range of the system. The outputs of a deflectometry test are the coordinates of the source which illuminate each camera detector pixel. To process the data, every camera pixel has a ray traced along its pointing vector to an intercept point at the UUT model. The local slope at the intercept point required to send the ray to the recorded source point is calculated. The local slopes are integrated to reconstruct the UUT surface. Any error in the ray coordinates directly affects the reconstruction accuracy. Hardware and calibration approaches allow for error mitigation in detector and source coordinates [5,6]. An error in calculated UUT intercept coordinates is controlled by having an accurate UUT model to trace to. Unfortunately, there are times when the model is not well known, such as during the grinding phase of an optic, where the root-mean-square (RMS) surface shape error from ideal changes from the millimeter-to-micron scale. Without an accurate surface model, it is nearly impossible to correctly determine the ray intercept coordinates at the UUT surface, leading to errors in the reconstructed surface. It is worth noting that low-spatial to mid-spatial frequencies are particularly suspect, as they often represent the largest magnitude error between the UUT model and reality [5].

Reconstruction methods, when no accurate UUT model exists, are limited, and they require a user input surface model. One approach is to assume a flat for the UUT model, which works well for flat UUTs or near-flat UUTs. Proper calibration is required for accurate deflectometry reconstruction. Using an iterative system parameter optimization process leads to improved reconstruction results [7]. A rapid reconstruction method using a non-zonal parameter dependent integration to improve the initial UUT model, followed by a successive over-relaxation zonal integration can improve reconstruction, provided the initial surface model is accurate enough [8,9].

All methods described are user input intensive, however. Extending preliminary work [10], which required a seed input surface model and was only used for a spherical UUT, we have created a general iterative data-processing technique that removes the need for an input surface model, known as model-free iterative deflectometry (MID). It improves reconstruction of freeform surfaces, including the low spatial frequency terms which could not be accurately reconstructed using the previous non-iterative techniques. The MID approach takes no input UUT model; instead, it utilizes the freeform-reconstructed surface that is the output from a deflectometry measurement as a continuously updating surface model for the UUT. This process is repeated until the reconstructed surface converges. The feature of adjusting all spatial frequencies, including the low order shape, which often contains the largest discrepancy between the initial guess (i.e., flat) and the true shape of the UUT model at each iteration, allows for improved reconstruction accuracy across all spatial frequencies. In this Letter, we present reconstruction results from data collected via a software configurable optical test system (SCOTS) [5], which demonstrate the improved performance the MID technique has over traditional non-iterative deflectometry techniques for model-free measurements. Figure 1 illustrates the iterative process and the error an incorrect surface model imparts.

In the MID technique, the Cartesian coordinates in the object space (UUT) of the camera pixels and the source coordinates, defined as matrices C and S, respectively, must be known. The UUT surface is unknown, and thus a flat surface model is used, defined as the matrix U^0. To bound the solution space, a physical coordinate on the UUT, $u_k(x, y, z)$, must be measured and used in the definition of the UUT surface model. Finally, the ray-pointing vectors of the camera pixels, defined as matrix R, are determined via a calibration process. These are the fundamental inputs into the MID process. With these inputs, the MID process runs for $t = 0{:}N$ iterations.

A Delaunay triangulation [11] segments the UUT model into surface planes, defined as matrix Q^t, and the intercept locations, defined as matrix I^t, are calculated with a Möller–Trumbore algorithm [12]. This combined Delaunay/Möller–Trumbore (DMT) process is a key step in the MID method. The Delaunay triangulation takes the discrete surface points, defined by mapping the camera pixels to the UUT surface, and creates unique planes that are well-shaped triangles and have a nearest-neighbor relation. The number of planes is dependent upon the number of camera pixels. The Möller–Trumbore algorithm, meanwhile, is a rapid 3D ray-triangle intersection method, which calculates the intercept coordinate every camera pixel ray makes with the segmented surface planes via a matrix approach. Processing time for the combined DMT process linearly increases while an improvement in reconstruction accuracy exponentially decays with respect to the number of camera pixels. Figure 2 demonstrates the combined DMT process.

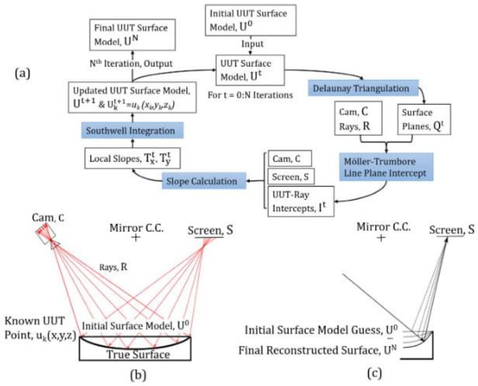

Fig. 1. Starting with a surface model guess of U^0, the MID process iterates a total of N times to output the final reconstructed surface model U^N (a). Without MID, the rays are traced to the incorrect theoretical surface U^0 (b). Using the MID method, the true surface can be converged upon (c).

Using the intercept locations along with the ray start and end points, from C and S, the local surface slopes of the UUT in the x direction and the y direction, defined as matrix T_x^t and matrix T_y^t, respectively, are calculated. The slopes are integrated using Southwell integration [13] to reconstruct the surface model. This process is iterated, outputting a new reconstructed surface model U^t, for a total of N iterations. The final output is the reconstructed surface model U^N.

As a numerical verification of the concept, a deflectometry simulation of a known optical surface was performed, and the surface was reconstructed using the MID method. The simulation modeled testing of a UUT with a SCOTS system. The raw deflectometry data, defined as the camera pixel coordinates, the pixel ray directions, the corresponding illuminating screen pixel coordinates for the camera pixels, and a known coordinate on the UUT, were recorded from the simulation. The simulated UUT was one of the hexagonal segments of the James Webb Space Telescope (JWST) primary, a segmented mirror system which uses hexagonal sub-mirrors to make the primary mirror [14]. The segment was 1320 mm in diameter, with a radius of curvature of 15899.91 mm and a conic of −0.99666. The mirror segment was 1320 mm off axis from center. The surface was reconstructed using the MID method for a total of nine iterations. The camera was modeled with 101 × 101 pixels, and each iteration took approximately 22.01 s. For the simulation, with an ideal system, the final surface RMS difference from the ideal was 6.17 picometers. With zero iterations, the RMS difference from the ideal was 280.97 μm, thus we see a dramatic improvement in reconstruction accuracy from the MID technique.

To demonstrate the numerical robustness of the MID method against noise, two cases were examined. In the first case, white noise from 0 μm to 1 μm in the x position and the y position was added to the detector coordinates. In the second case, inaccurate global positions of the camera and screen were simulated, with a shift in the position of all camera pixels by 1 mm in the x direction being imparted. Again, nine iterations were used for the MID reconstruction. The final error in the reconstructed surfaces is shown in Fig. 3.

The numerical simulation results suggest that white noise adds a random high spatial frequency error to the reconstructed

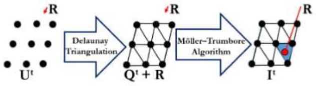

Fig. 2. Delaunay algorithm segments U^t into planes, Q^t, and the ray (R) intercept points I^t are calculated using a Möller–Trumbore algorithm.

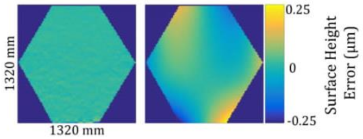

Fig. 3. Simulated error from white noise (left) and global positioning error (right) led to an RMS surface error of 11.17 nm and 66.24 nm, respectively, in the final reconstructed surface map.

surface map, with a root mean square (RMS) error of 11.17 nm. Such noise is unavoidable when using common detectors and monitors. The geometric uncertainty error added low spatial frequency error to the final reconstructed map, primarily in the form of astigmatism and coma. Across the reconstructed hexagonal mirror, the RMS error was 66.24 nm and 519.54 nm peak to valley (PV). This error is challenging to reduce without moving to advanced hardware and calibration techniques.

To verify the performance of the MID method in a real measurement, a bare glass optical surface with freeform departure in all directions was manufactured and measured. The radius of curvature (RoC) of the surface was 200 mm, and the diameter was 100 mm. The UUT had a ~0.67-μm RMS and a ~2.50-μm PV departure from the base sphere, with a maximum surface slope of 576.64 μrad. The optic was fabricated by Optimax Systems using the magnetorheological finishing (MRF) technique to impart a spiral pattern on the optical surface. The surface was measured with a commercial interferometer, the Zygo Verifire MST, and a SCOTS deflectometry system. A Zygo F/1.75 reference sphere was used as the reference optic for the interferometer. The interferometric technique used does not allow for the accurate reconstruction of the piston, tip, tilt, or power terms of the UUT, and thus they were not analyzed in the deflectometry measurement. Figure 4 demonstrates the complex fringe pattern recorded at the best null condition and the challenges associated with high fringe density in the interferometric test.

For the deflectometry system, a custom SCOTS type system built from off the shelf components was used. We utilized a Point Grey (Model # FL3-U3-32S2M-CS) camera, with a 2.5-μm pixel pitch, due to ease of access to technical specifications. When selecting the monitor, the primary consideration was required source extent to allow for testing the dynamic range of the UUT, which can be described by the aberrated spot size through an inverse ray-tracing from the pinhole location to the UUT, and to the screen. A 7″ × 5.25″ Mimo (Model # UM-760F) screen with a 150-μm pixel pitch was selected as it met the dynamic range requirements.

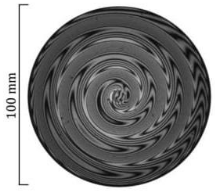

Fig. 4. Spiral shape on the UUT made obtaining an interferometric null configuration impossible for the entire mirror. Low modulation due to fringe density led to areas on the surface being unmeasurable.

To calibrate the system and determine the pointing vectors of the camera pixels, a previously described calibration method was utilized [10]. A screen was placed at two positions—$l_1(x, y, z)$ and $l_2(x, y, z)$. The camera was at a fixed position $c(x, y, z)$, and the coordinates of the illuminating screen pixel at $l_1(x, y, z)$ and $l_2(x, y, z)$ for every camera pixel were measured. The ray path for every camera pixel was then calculated. All the coordinates were measured with a coordinate measurement machine (CMM), accurate to ±10 μm.

For the deflectometry test, the UUT was placed on a rotation stage below the screen and camera. All components were mounted in place on a breadboard to maintain position throughout testing. A CMM, accurate to ±10 μm, was used to locate the body edges of the camera and screen using a touch tip. A plane was fit to the screen, while technical drawings relating the camera detector to the body were used to determine the detector coordinates. Additionally, the center point of the UUT, about which it rotated, was located. This served as the known coordinate, $u_k(x_k, y_k, z_k)$ and as the global zero coordinate in x, y, and z. This was related to the camera pixel measuring the known coordinate, pixel $p(x, y, z)$. A phase-shifting deflectometry measurement was then performed. The resulting raw data was recorded for processing.

The raw data was processed in three ways. First, the MID technique was used for a total of six iterations. Also, in a traditional non-iterative way, the data was reconstructed by assuming (1) a flat for the base surface and (2) a 200-mm RoC base sphere model, representing an unknown and known model case, respectively. The same raw data was used for all cases. To account for systematic error in the measurements a rotation calibration was performed [15]. The average error map was determined by reconstructing the UUT measured every 10° for a full rotation and calculating the average, which was subtracted from the final reconstructed map. The reconstructed surfaces generated with the MID technique and the two traditional techniques, referred to as MID_6, MB_{flat}, and $\text{MB}_{\text{sphere}}$, respectively, were then analyzed to compare the Zernike terms and the reconstructed surface shape to the surface measured by the interferometer, referred to as INT. The missing data regions in the INT are not considered in the comparison, as we did not want to extrapolate/interpolate data for comparison. The surface evolution of the MID_6 through iterations is visualized in Fig. 5.

The Zernike terms were fit to the surfaces and low order spatial frequency terms were analyzed. Table 1 displays the difference from the interferometric result in the low order Zernike terms (RMS normalized) for the MID_6 map, the MB_{flat} map, and the $\text{MB}_{\text{sphere}}$ map. The Zernike terms 1–4, the piston, the tip, the tilt, and the power, were removed to match the fact that the interferometer was unable to accurately measure Zernike terms up to Z4. (The interferometric data also

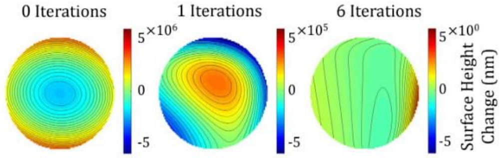

Fig. 5. Surface height change between 0 (left), 1 (middle), and 6 (right) iterations shows the most significant change occurs in early iterations. The black lines show the surface contours. (See Visualization 1).

Table 1. Low Order RMS Normalized Zernike Term Difference between Reconstructed and Interferometric Surface Maps

Zernike Term	MID_6 (μm)	MB_{flat} (μm)	MB_{sphere} (μm)
Z5, Oblique Astigmatism	0.76	1.90	0.42
Z6, Vertical Astigmatism	−5.12	−44.28	−15.80
Z7, Vertical Coma	−0.36	−1.98	−0.40
Z8, Horizontal Coma	−0.10	0.55	0.11
Z9, Vertical Trefoil	0.32	1.01	0.25
Z10, Oblique Trefoil	−0.05	0.29	0.06
Z11, Spherical	0.04	0.63	0.17
Z5:Z11 Total RMS Diff	5.20	44.39	15.80

includes its own uncertainties due to high fringe density from the non-null configuration).

The total Zernike term RMS departure, for low order terms Z5–Z11, from the INT for the MID_6, MB_{flat}, and MB_{sphere} surfaces were 5.20 μm, 44.39 μm, and 15.80 μm, respectively. This demonstrates that without subtracting any low order terms, beyond the standard removal of terms up to power, the MID method provided close to an order of magnitude improvement in accuracy matching the interferometric measurement compared to traditional deflectometry with no accurate model. The reconstructed surface maps, with the increasing Zernike term removal, are shown in Fig. 6.

The MID technique resulted in a surface that more closely matched the interferometric measurement when compared to a traditional non-iterative technique for model-free deflectometry surface reconstruction. Particularly, at the low spatial frequencies, it achieved more similar results to the interferometric measurement. We acknowledge that there are still residual differences, predominantly in the astigmatism and the coma, between the interferometric measurement and the MID reconstructed surface. Small uncertainties in geometrical knowledge of the positions of all components contributed to some of the residual astigmatism and coma in the MID_6 reconstructed surface. However, the MID method improves the well-known low order accuracy issues of traditional deflectometry while maintaining the advantage of a large dynamic range, when compared to interferometry. The effect of the dynamic range is particularly clear for this UUT, which suffered from missing data regions in the measured interferometric map due to the inability to obtain a null over the entire surface.

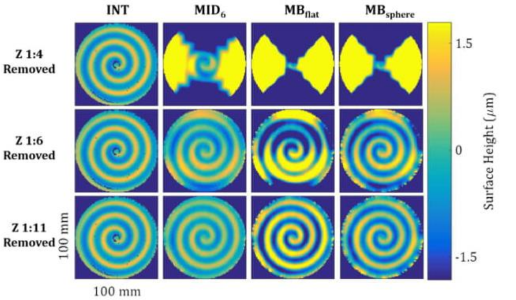

Fig. 6. Reconstructed interferometric surface map (first column), MID method with six iterations (second column), and non-iterative traditional reconstruction with a flat UUT model (third column) and a 200 mm RoC base sphere model (fourth column) method had Zernike terms 1–4 (top row), 1–6 (middle row), and 1–11 (bottom row) removed to compare error contribution from low spatial frequency. (Note: excess fringe density led to missing data in the interferometric map).

The MID technique represents a novel data-processing solution that can provide more accurate surface reconstruction results for a deflectometry measurement across all spatial frequencies. We do not claim that the MID method is superior to other precision metrology techniques such as interferometry. Instead, we seek only to improve the deflectometry-processing approach to provide more value to the optics metrology community by providing multiple options and crosschecking metrology solutions. The technique is delivered via a software package and can easily be included in an existing deflectometry system's processing pipeline. The MID method seeks only to address the fundamental reconstruction error which arises from inaccurate surface modeling of the UUT. The reported enhancement in measurement accuracy is achieved solely by the new data processing concept, not by improved hardware or calibration techniques. Using the proposed MID method, the same raw data can be reprocessed to produce a higher accuracy result, which was hidden in the raw data but not previously utilized in the surface reconstruction pipeline. This highlights the significance of the MID approach maximizing the use of information in the commonly measured deflectometry data.

Funding. II-VI Foundation Block-Gift Program.

Acknowledgment. This research was made possible in part by the II-VI Foundation Block-Gift Program, the Technology Research Initiative Fund Optics/Imaging Program, the Freeform Optics project supported by the Korea Basic Science Institute, the Friends of Tucson Optics Endowed Scholarships in Optical Sciences, and we thank Optimax Systems for providing the freeform UUT.

REFERENCES

1. B. Martin, J. Burge, S. Miller, S. Warner, and C. Zhao, *Frontiers in Optics/OF&T*, OSA Technical Digest (Optical Society of America, 2008), paper OWD6.
2. C. J. Oh, A. Lowman, G. Smith, P. Su, R. Huang, T. Su, D. W. Kim, C. Zhao, P. Zhou, and J. Burge, Proc. SPIE **9912**, 99120O (2016).
3. M. B. Dubin, P. Su, and J. Burge, Proc. SPIE **7426**, 74260S (2009).
4. D. W. Kim, C. J. Oh, A. Lowman, G. Smith, M. Aftab, and J. Burge, Proc. SPIE **9912**, 99120F (2016).
5. R. Huang, *High Precision Optical Surface Metrology Using Deflectometry* (Academic, 2015).
6. D. W. Kim, M. Aftab, H. C. Choi, L. Graves, and I. Trumper, *Frontiers in Optics* (Optical Society of America, 2016), paper FW5G.4.
7. E. Olesch, C. Faber, and G. Häusler, *DGaO Proceedings* (2011), Vol. **112**.
8. T. Zhou, K. Chen, H. Wei, and Y. Li, Appl. Opt. **55**, 2760 (2016).
9. H. Zhang, S. Han, S. Liu, S. Li, L. Ji, and X. Zhang, Appl. Opt. **51**, 7616 (2012).
10. W. Zhao, L. Graves, R. Huang, W. Song, and D. W. Kim, Proc. SPIE **9684**, 96843X (2016).
11. S. Cheng, T. Dey, and J. Shewchuk, *Delaunay Mesh Generation* (CRC Press, 2013).
12. T. Möller and B. Trumbore, J. Graph. Tools **2**, 21 (1997).
13. W. H. Southwell, J. Opt. Soc. Am. **70**, 998 (1980).
14. H. P. Stahl, in *Optical Society of India Symposium: International Conference on Optics and Optoelectronics* (2014).
15. C. Evans, R. Hocken, and W. Estler, CIRP Ann. **45**, 617 (1996).

APPENDIX B

Infinite Deflectometry Enabling 2π-steradian Measurement Range

Logan Rodriguez Graves, Henry Quach, Heejoo Choi,
and Dae Wook Kim

Copyright Transfer Agreement

Reprinted with permission from ref Opt. Express 27, 7602-7615 (2019), with permission from The Optical Society of America. COPYRIGHT **2019**.

Research Article Vol. 27, No. 5 | 4 Mar 2019 | OPTICS EXPRESS 7602

Optics EXPRESS

Infinite deflectometry enabling 2π-steradian measurement range

L. R. GRAVES,[1] H. QUACH,[1] H. CHOI,[1] AND D. W. KIM[1,2,*]

[1]*College of Optical Sciences, University of Arizona, 1630 E. University Blvd., Tucson, AZ 85721, USA*
[2]*Steward Observatory, University of Arizona, 933 N. Cherry Ave., Tucson, AZ 85719, USA*
** letter2dwk@hotmail.com*

Abstract: We present a novel deflectometry implementation termed Infinite Deflectometry. The technique provides a full aperture surface reconstruction sag map of freeform surfaces, including previously challenging to measure optics such as highly convex surfaces. The method relies on the creation of a virtual source enclosure around the tested optic, which creates a virtual 2π-steradian measurement range. To demonstrate the performance, a fast f/1.26 convex optical surface was measured with a commercial interferometer and with the Infinite Deflectometry system. After removing Zernike terms 1 through 37, the metrology tests resulted in absolute RMS surface values of 18.48 nm and 16.26 nm, respectively. Additionally, a freeform Alvarez lens was measured with the new technique and measured 22.34 μm of surface sag RMS after piston, tip/tilt, and defocus had been removed. The result deviated by 488 nm RMS from a profilometer measurement while standard interferometry failed to measure the Alvarez lens due to its non-nulled wavefront dynamic range limitation.

1. Introduction

While freeform optics provide ever-growing possibilities in designing cutting edge optical systems, their fabrication and metrology remain challenging. Currently, a wealth of fabrication methods exists whose variety provide improved fabrication of freeform surfaces. Such methods include computer numeric controlled (CNC) machining using a diamond tip tool, sub-aperture polishing using a magnetorheological fluid (MRF), molded optics, precision polishing, and more [1–5]. In verifying the freeform shape generated, two commonly utilized non-contact optical metrology methods for a unit under test (UUT) are interferometry and deflectometry [6,7].

Interferometry, which offers high accuracy and precision in surface metrology, requires a null setup to obtain accurate test results of a UUT. Computer generated holograms (CGHs) are increasingly chosen as null components in interferometric tests for their abilities to precisely create a freeform null wavefront, and, in some cases, provide additional alignment features [8,9]. Unfortunately, CGHs can be prohibitively expensive and can only null a designed specific configuration. Alternatively, deflectometry is a non-null test method which has been shown to provide surface metrology accuracy similar to commercial interferometry systems for freeform optics [7,10–12]. The method relies on rays leaving a source, being deflected by a UUT, and then being recorded by a camera. In this way, the local slopes across the UUT are measured, which can be used to reconstruct the surface through integration.

One subset of optics that still is highly challenging to measure is convex optics, both standard in shape as well as freeform. There exist a variety of test methods, including interferometric approaches, swing arm profilometry, and the Hindle test [13–15]. Most methods typically require measuring sub-apertures of the unit, which are then ‘stitched’ together. Great improvements have been made in interferometry algorithms which lead to improved sub-aperture stitching results [14,16–18]. Unfortunately, having an interferometric setup and the required null optic is not always a viable option. Further, spatial sampling of the surface shape can be limited with other metrology techniques such as contact-type

#358219 https://doi.org/10.1364/OE.27.007602
Journal © 2019 Received 21 Jan 2019; revised 17 Feb 2019; accepted 17 Feb 2019; published 28 Feb 2019

profilometers, negatively impacting the mid-to-high spatial frequency measurement capability.

While traditional deflectometry has been used as a 3D object reconstruction method for surfaces up to and including weak (i.e., large radius of curvature) convex surfaces, a full aperture optical precision test of a general convex surface has not been achieved. However, there have been successful methods which measure a plano-convex optic in transmission [19], as well as using a unique scanning laser deflectometry system to measure the departure from a sphere of convex aspheric surfaces [20]. The fundamental limitation to testing a surface using traditional deflectometry is satisfying a line of sight condition. When considered in reverse, if a ray from the camera can be traced to a point on the optical surface and, following the law of reflection, passes through the source area, the optical surface slope can be determined at said location. Traditionally, for a concave test using deflectometry, the source and camera will be placed as close to the center of curvature as possible [21,22]. This allows a small area on the source (e.g., small liquid crystal display [LCD] screen) to fully satisfy the line of sight condition. However, as the optical surface transitions from concave towards convex, the source area must increase to satisfy the line of sight condition. One work-around is instead to surround the optical surface with the screen. One implementation of this concept, known as ‘Cavlectometry’, has successfully been used to reconstruct low order surface shapes of objects such as the hood of an automobile and a teapot [23]. In this approach, a projector system was used to project phase-shifted fringes onto the walls of a room in which the tested object sat. The system is thus able to achieve an extremely large source area which encloses the UUT.

An array of projectors is not the only possible method for creating a source enclosure. While a projector array can nicely satisfy the need to create a source enclosure around the UUT, projectors systems suffer from lower resolution, optical aberrations, contrast uniformity, and more [24,25]. This in turn adds uncertainty to the deflectometry system, which can limit reconstruction accuracy. Modern digital displays possess characteristically higher resolution but are also limited by realizable source sizes. In a new configuration, a high-resolution source enclosure may be achieved by seating a UUT atop a precision rotation stage which clocks the UUT, while a digital screen and camera are mounted in place. Here, each clocked position generates a new ‘virtual’ deflectometry system, which is equivalent to rotating a single tilted display and camera about the UUT. By using multiple clocking positions, a series of ‘virtual’ screens can be created which entirely enclose the UUT, creating a tipi-shaped 2π-steradian measurement space. This is the fundamental concept of Infinite Deflectometry (ID).

In this paper we present a novel optical quality deflectometry method which generates a full aperture surface map of a unit under test. The method uses the ‘Cavlectometry’ model as inspiration, but instead creates a source enclosure around the UUT by means of a series of ‘virtual’ high resolution digital displays. This allows for high accuracy testing of fully freeform surfaces, including previously unachieved optical quality full-aperture surface metrology maps of convex surfaces using deflectometry. This method, termed ‘Infinite Deflectometry’, to reflect an ‘infinite’ dynamic range (practically limited by camera line of site), was used to measure both a highly convex spherical optic and an Alvarez lens. Results demonstrate a close match between full-aperture interferometric testing results for the convex spherical optic. Additionally, the Alvarez test results suggest this new branch of deflectometry expands the range of testable surfaces without necessitating a custom null component.

2. Background theory

2.1 Phase shifting deflectometry

Phase shifting deflectometry is a popular metrology method for testing optics [7,21,22,26–29]. The technique calculates the local slopes on a UUT using a camera and a digital display.

The camera is positioned to image the UUT surface. The camera pixels have their 3D location recorded, defined as x_c, y_c, z_c, and the pixels are mapped to the UUT surface. The mapped pixels represent discrete areas on the UUT where the local slopes will be calculated, known as 'mirror pixels'. The 3D location of the UUT and specifically the precise location of the mirror pixels is determined for the test, defined as x_U, y_U, z_U. The digital source displays a sinusoid pattern in the x and y directions, using a minimum of 3 phase steps. The reflected light is captured by the camera and the recorded wrapped phase is acquired. The phase is unwrapped and the precise location on the source which successfully illuminated every camera pixel corresponding to its mirror pixel is determined. By relating these to the location of the display, the 3D location of the display points corresponding to the camera detector pixels is determined, known as x_S, y_S, z_S. Using these three data matrices, the local slopes in the x and y orthogonal directions of the UUT at the discrete 'mirror pixels' are calculated. Finally, the local slopes are integrated, typically using a zonal integration method such as a Southwell integration [30]. In this way, the surface is reconstructed from a deflectometry slope measurement.

2.2 Infinite deflectometry creating virtual source

The deflectometry test method as described is a non-null metrology method. Two key aspects limit the range of surface slopes that the system can practically measure. First, the camera must have a clear line of sight to the area on the UUT that is to be measured. Second, if the camera pixels are traced from the camera to the UUT surface and deflected, following the law of reflection, the rays must pass through the defined source (i.e., screen) area. While the traditional deflectometry method works well for most concave surfaces, as the required source area is small by performing the test near the center of curvature, it struggles to test optical surfaces as they move away from a concave shape. As the UUT surface has a wider range of slopes, typical for freeform surfaces, or as the surface moves towards a flat or convex shape, the required source area to cover the UUT rapidly becomes very large. One work around proposed is to enclose the UUT with the source [23], thus allowing for testing a wider range of surface slopes. Figure 1 demonstrates the challenges associated with testing a convex surface with a traditional deflectometry setup and how a source enclosure could expand the testable surface range.

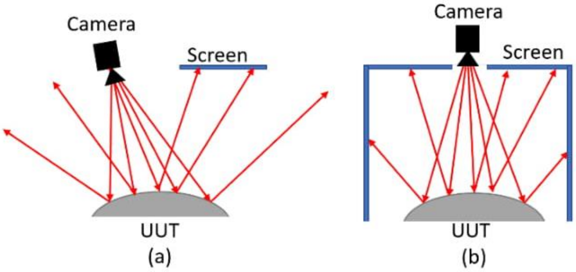

Fig. 1. A traditional deflectometry system utilizes a camera and source to test a UUT. If considered in reverse, rays can be traced from the camera to the UUT where they are deflected by the UUT mirror surface and, if they pass through the source area, the local slope on the UUT can be determined using geometry. For some surfaces, such as a convex optic, a regular screen is not large enough to allow for testing the full area of the UUT due to the missing rays (a) and presents an area where deflectometry has historically not been able to provide full aperture metrology maps. One alternative is a source screen which encloses the UUT, allowing for testing the full range of surface slopes without missing rays (b).

A modern LCD is a common source used in a deflectometry setup, desirable for their high resolution and stability. Depending on the system architecture and the optic under test there is a limit to the testable dynamic range of surface slopes for the UUT for given display size and resolution. The testable dynamic range increases as the size of the display increases, but there is a limit to the size of display that can reasonably be obtained. While a monolithic box-shaped screen which encloses the UUT would be ideal, no such screen exists in practice. Utilizing a projector system is one alternative, but there are significant distortion, uniformity, and mapping challenges associated with projectors, which limit their usability for high precision nanometer scale optical tests.

Instead of increasing the size of the screen, a series of virtual screens has been generated in the Infinite Deflectometry system. In this way, the benefit of a small high-resolution display can be leveraged while at the same time creating a larger source area. To achieve this, a source display is positioned tilted over the UUT, with a camera positioned over the UUT to image the surface. To generate a virtual screen, the UUT is clocked by a fixed angular step, which presents new areas of the UUT to the screen and camera. After a full 2π rotation of clocking steps, this can equivalently be thought of as generating a tipi-shaped virtual screen. This process is repeated to create overlapping virtual screens which entirely enclose the optic, thus allowing for the entire range of surface slopes to be tested. It should be noted that the ability to create the virtual screen enclosure is limited by the size of the UUT and the available source. For extremely large UUTs, even the largest commercially available screen will not be able to fully virtually enclose the UUT in the described configuration. Figure 2 demonstrates the setup concept, and how one high-performance screen which can test only a limited area on the UUT can be turned into six virtual screens to enclose the UUT.

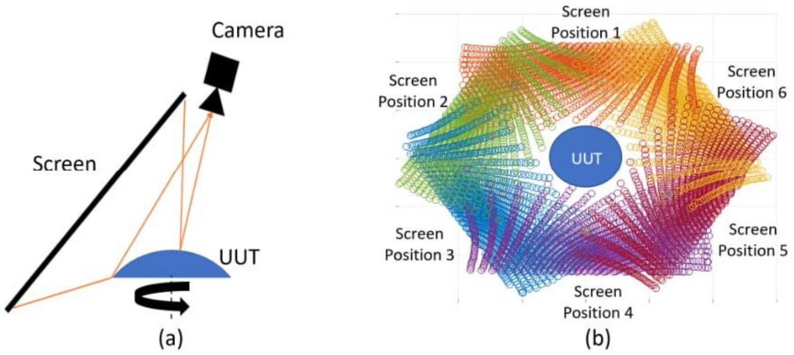

Fig. 2. By tilting a high precision screen over a UUT, and correctly positioning the camera, a partial area of the UUT can be measured using traditional deflectometry (a). If the UUT is placed on a precision rotation stage and clocked to multiple angular orientations (e.g., 6 screen positions), the full area of the UUT can be tested. This can be thought of as instead virtually clocking the screen and camera, creating a virtual source enclosure allowing for the same precision metrology over the full UUT aperture. Because each screen can only cover a segment of the UUT, a reverse ray trace from the camera pinhole to the UUT is performed to determine the intercept locations with the virtual screens, seen from the top down as scattered points (b).

At each clocking position, a deflectometry measurement is performed which covers a partial section of the UUT. After recording the data, the local slopes are calculated for every virtual configuration. This is done by carefully determining the 3D positions of the camera, screen, and UUT in the default unclocked test position, which are described as matrices which contain the individual local x, y, z positions previously discussed and are referred to as C_0, S_0, and U_M respectively. It should be noted that U_M represents an accurate model of the UUT whose center position defines the global coordinate system. During processing, for the first clocked testing position, the camera and base screen position matrices are rotated about the UUT optical axis by the amount the UUT was clocked during the test, creating new 3D position matrices. The new virtual camera position matrix is referred to as C_1 and following the phase unwrapping process the local screen positions are correlated to the global screen position, and the new virtual screen position matrix, S_1, is determined. This process is repeated for every clocking position, which for N clocking positions of the UUT results in a total of N (0 to N-1) camera and source 3D position matrices. When this process is completed, N deflectometry test data sets exist, and the local slopes for every test are determined. This is accomplished by tracing the camera pixels for every camera matrix $C_{0:N-1}$ to U_M, the UUT model, to determine the local ray intercept locations. These local ray intercept points, which are the x_U, y_U, z_U coordinates for every clocking position, are stored in matrices $U_{0:N-1}$. Knowing the final ray locations, which are recorded as the x_S, y_S, z_S in screen matrices $S_{0:N-1}$, the local slopes on the UUT model for every virtual test system in the global x and y directions are determined and recorded as $X_{0:N-1}$ and $Y_{0:N-1}$ respectively.

To combine the data into cohesive x and y local slope maps of the UUT, a multi-step process is used. First, due to uncertainty in positioning of components, there exist some uncertainties associated with the positions determined for all components in the system. These errors most heavily dominate low spatial frequency shapes, particularly piston, tip and tilt, defocus, and astigmatism. Therefore, these terms are removed from the local slope maps by subtracting the mean values of the local slopes and then performing a best fit plane to the data and subtracting this away as well. In the spatial domain, the mean of the local slopes represents the tip/tilt (depending on if it is the x or y data) while the plane fit to the data represents the first derivate of the surface, corresponding to the defocus and astigmatism of the surface. It is worth mentioning that, fundamentally, this uncertainty can be reduced with more thorough calibration and higher accuracy hardware components, which broadly is true for all general stitching metrology system cases.

After this step, the data is combined by performing linear interpolation fitting which takes the x and y UUT intercept locations and the adjusted local slope data for every test and generates a single cohesive x and y slope map of the UUT. The x and y slope maps are generated over a uniform grid. The local slopes were averaged for positions where the ray intercepts overlapped for two or more sub-aperture local slope measurements. The local slope maps in the x and y directions of the entire UUT surface are referred to as T_X and T_Y respectively. It must be noted that because the subaperture local slope maps have the slopes determined in the global coordinate system, all subaperture local slope maps are in the same reference frame. A Southwell integration [30] is then performed on T_X and T_Y which results in a reconstructed surface sag map, referred to as U_R. It is important to acknowledge that the unique value and novelty of the Infinite Deflectometry is in the enhanced dynamic range enabled by the virtual tipi screen geometry, not in the general stitching performance related treatments, which has been actively studied and reported by the stitching metrology community. Figure 3 demonstrates the data processing flow from raw data acquisition to a full aperture reconstructed surface map.

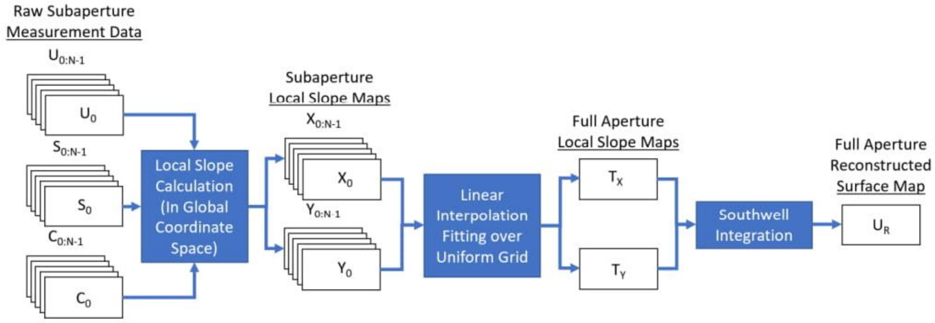

Fig. 3. Infinite Deflectometry uses a traditional deflectometry system in a unique configuration combined with clocking the UUT, which results in *N* virtual deflectometry system measurement sets, each measuring a subaperture area of the UUT. Each measurement outputs standard deflectometry outputs, resulting in global x,y,z coordinates for every test for the camera ($C_{0:N\text{-}1}$), UUT ($U_{0:N\text{-}1}$), and screen ($S_{0:N\text{-}1}$). Local slope maps in the global x and y directions for all subaperture tests are then determined, called $X_{0:N\text{-}1}$ and $Y_{0:N\text{-}1}$ respectively. A linear interpolation is used to fit the subaperture slope maps into full aperture x and y slope maps, called T_X and T_Y respectively, which are integrated using a Southwell integration to produce a full aperture reconstructed surface map of the convex UUT, called U_R.

This combined hardware and software process represents the Infinite Deflectometry technique. The method was used to test previously unmeasurable surfaces using traditional deflectometry, which demonstrate that the ID method can greatly extend the dynamic range of deflectometry to provide full aperture surface reconstruction of freeform surfaces, including flat or convex optics.

3. Experimental setup and measurements

3.1 Infinite deflectometry hardware configuration

To build and demonstrate the ID system a camera, source, and precision rotation stage were required. We utilized a Point Grey Flea3 camera (Model # FL3-U3-32S2M-CS), which has a 2.5 µm pixel pitch. This camera was utilized as its technical and mechanical data was well specified, and it had a high-resolution detector. For the source an Apple iPad Pro (Model # A1670) was utilized which measured 262.85 × 197.04 mm and had 2732 × 2048 pixels, with a 96.2 µm pixel pitch. The UUT was placed on a custom 3D printed mount, which fit into the rotation stage utilized for the test and centered the optic to the center of the rotation stage. The rotation stage was composed of a Klinger motorized rotary stage (Model # DP179), driven by a Leadshine digital stepper driver (Model # EM402).

The camera was mounted nearly centered above the UUT, while the screen was mounted in front of the UUT, and was tilted, such that the top edge of the screen slightly passed over the center of the UUT. The actual setup is shown in Fig. 3. All components were mounted on a breadboard to maintain position throughout testing. The edges of the camera body and the screen body were measured using a Coordinate Measuring Machine (CMM), accurate to ± 10 µm. Using technical drawings, the pixel positions were located relative to the camera body, while a plane was fit to the screen. The UUT body and center was measured as well, and the center of the UUT served as the global origin (0, 0, 0) coordinate. The z axis was defined as normal to the UUT and pointing up, away from the breadboard. The y axis was defined as pointing toward the screen from the UUT center, and the x axis was orthogonal to the z and y axis.

To determine the camera pointing vectors, a process previously performed was used [31,32]. The process relies on mounting the camera system such that it is pointed at a high precision monitor. The 3D position of the monitor and the camera are measured using a CMM. A line scan is performed on the monitor while the camera records. For every pixel on the camera, the centroid of the measurement response is determined to precisely calculate which location on the screen was being measured by every camera pixel. The monitor was then translated along the optical axis of the camera and the process was repeated. In doing so, the precise ray vector for every camera pixel between the two screen positions could be calculated, which served as calibration of the camera ray pointing vectors. This process was performed for the camera used prior to it being mounted in the final ID system.

Once the overall assembly and the camera calibration had been performed, the ID system was used for metrology. For every clocking position, a 16-step phase shifting deflectometry (PSD) test was performed. This involved using 8 phase steps in the horizontal and vertical directions (defined by the screen) each. The entire system was shielded during all tests from stray background light by placing a heavy black cloth over the system. After a measurement was performed, the data for the clocking position was saved and then the rotation stage would rotate the UUT to the next clocking position automatically. This process was repeated until a total of *N* rotations were performed. After all data was collected the local slopes at every clocking position were determined, and full aperture local slope maps in the X and Y directions were calculated using the method described previously. These local slope maps were integrated using Southwell integration and the final reconstructed surface map was acquired.

3.2 Fast convex mirror measurement case

To verify the performance of the system, a fast f/1.26 50 mm diameter convex sphere (UUT in Fig. 4) was measured using the ID setup described. Tests using 6, 45, 90, and 180 clocking positions were performed for comparison, which are referred to as ID_R in the results section, where *R* is the number of clocking positions used, and defines the number of virtual screens which enclosed the UUT. The clocking positions were equally spaced over a full 360° to ensure maximum exposure of the UUT surface to the virtual displays. This was used to determine the as-built reconstruction performance as a function of clocking steps used.

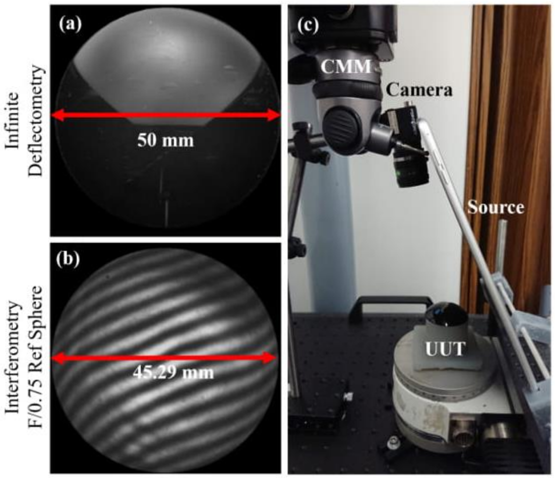

Fig. 4. A fast f/1.26 convex spherical optic with a 50 mm diameter clear aperture was measured using the Infinite Deflectometry system (a). As a comparison, a Zygo Verifire$^{\mathrm{TM}}$ MST interferometer was used to provide an independent measurement of the same optic (b), which measured a maximum 45.29 mm diameter aperture inside of the 50 mm clear aperture. The Infinite Deflectometry system was composed of a camera, source, and the UUT on a rotation stage, and all components were mounted in place and measured using a CMM (c).

The test using a total of 180 clocking positions, whose reconstructed surface map is referred to as $\mathrm{ID}_{180,}$ served as the pseudo-ideal case representing the sufficient number of clocking steps. As an independent reference, the optic was measured using a Zygo Verifire^{TM} MST interferometer which provided a comparison sag map. Due to the available reference sphere and the as-manufactured shape of the UUT, the best null configuration tested only a 45.29 mm in diameter aperture inside of the 50 mm full diameter of the optic. This measured area is referred to as INT. In all final comparisons the surface root-mean-square (RMS) data is calculated only in the common 45.29 mm inner circle of the reconstructed sag maps. The raw data images from both setups are shown in Figs. 4(a) and 4(b).

3.3 Alvarez lens measurement case

An Alvarez lens was designed and manufactured from a PMMA 1-inch diameter disk, with the optical surface machined using a diamond turning machine to generate a 6 mm central aperture area inside of the PMMA disk. The ideal optical surface was generated to have 17 μm of Zernike term Z8, which represents horizontal coma, and −17 μm of Zernike term Z10, which represents 45° trefoil. This optic represents one half of an Alvarez lens pair. Due to the non-trivial freeform nature and wide dynamic range in the surface slopes, the full aperture had previously proven very difficult to measure. For example, without a custom nulling component, such as a CGH, the fringe density exceeded the measurable range of a commercial interferometer, as shown in Fig. 5. The ID system was utilized to measure the full 6 mm central aperture, and the surface was reconstructed, referred to as $\text{ID}_{\text{Alvarez}}$.

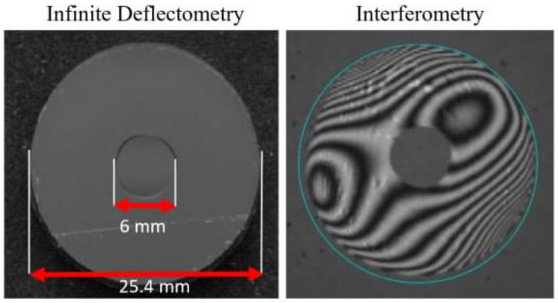

Fig. 5. An Alvarez lens was generated in a 1-inch PMMA disk. The surface was designed to have a 6 mm inner optical aperture which had 17 μm of horizontal coma and −17 μm of 45° trefoil. The surface was measured using the ID system, which measured the full aperture (left), as well using the Zygo Verifire^{TM} MST Interferometer using a reference flat without a custom CGH (right). Without a custom null optic, the fringe density exceeded the measurement capabilities of the interferometer, making it impossible to measure the central optical aperture.

As an alternative reference comparison measurement, a contact-type KLA-Tencor Alpha-Step D-500 profilometer was utilized to measure a surface profile of the Alvarez lens. The profile line was carefully chosen to measure a profile which passed through the middle of the lens and featured primarily the coma terms. A contact force of 10 mg was utilized for the measurement in order to prevent any damage or scratch on the PMMA surface (a trial test was performed with a higher force on a separate PMMA disk and resulted in a scratch on the surface). The height range of the profilometer was limited to a maximum height deviation of 100 μm with the 10 mg force limit. It is for this reason that the profile, which measured the middle of the lens in the horizontal direction was chosen, as this profile would ideally feature heights within the measurement range while also highlighting the part of the unique surface shape of the Alvarez lens. The same profile was taken from the $\text{ID}_{\text{Alvarez}}$ reconstructed map and compared. For both profiles, the mean values of the measurements were subtracted from the raw data, thereby setting the mean for both data sets to zero for direct comparison.

4. Infinite deflectometry performance

4.1 Metrology results for f/1.26 50 mm diameter convex sphere

For the comparison study, piston, tip/tilt, and defocus, corresponding to standard Zernike terms 1:4, were removed from both the interferometric and ID measurements, as they are blind to those terms. Additionally, more detailed comparisons were made after standard Zernike terms 1:6 were removed, after terms 1:21 were removed, and after terms 1:37 were removed. These are referred to for the $\mathrm{ID_R}$ maps as $\mathrm{ID}_{\mathrm{R}}^{1:Z}$ and for the INT map as $\mathrm{INT}^{1:Z}$, where Z refers to the highest number of standard Zernike terms removed. Finally, the surface sag root-mean-square (RMS) was calculated for the $\mathrm{ID}_{180}^{1:Z}$, and $\mathrm{INT}^{1:Z}$ maps over the common 45.29 mm circular aperture area of the UUT.

The reconstructed surface maps $\mathrm{ID}_{\mathrm{R}}^{1:Z}$, with Z standard Zernike terms removed and R clocking positions utilized are presented in Fig. 6. As further clocking steps are utilized in the ID system, improved reconstruction accuracy is achieved. Particularly of note are the high spatial frequencies in the reconstructed sag maps. The stitching error is most clear at high spatial frequencies when few clocking steps were used, such as in $\mathrm{ID}_{6}^{1:37}$ and $\mathrm{ID}_{45}^{1:37}$. It must be noted that for the as-built hardware used in the ID system presented here, the full test of the optic to gather the measurement data using 180 clocking is ~2 hours and 35 minutes. This does not include processing time. Thus, there is a clear tradeoff between reconstruction accuracy and time of acquisition.

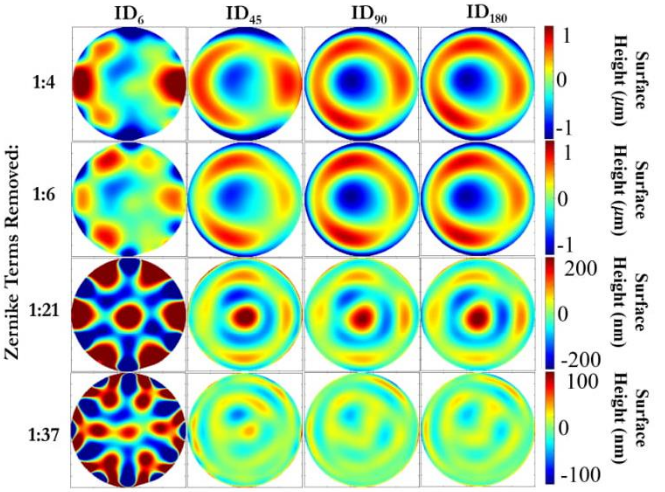

Fig. 6. The infinite deflectometry method utilizes the clocking of the UUT to create a virtual 2π-steradian tipi-shaped source area which enclose the UUT. A deflectometry test is performed at each clocking position, and the local slopes at each clocking are calculated and then stitched together to create a full aperture local slope map of the UUT, which are integrated to generate the total sag map. The process was performed for a fast f/1.26 convex sphere for 6 (1st column), 45 (2nd column), 90 (3rd column), and 180 (4th column) clocking step positions, equally spaced over a full 2π rotation. Stitching errors are apparent for fewer clocking positions, and manifest clearly as Zernike terms 1:4 (1st row), 1:6 (2nd row), 1:21 (3rd row), and 1:37 (4th row) are removed from the surface map.

The reconstructed surface maps generated by the ID metrology with 180 clocking steps, ID_{180}, and the Zygo Verifire$^{\mathrm{TM}}$ MST interferometer, INT, are compared in Fig. 7 as a function of *Z* standard Zernike terms removed.

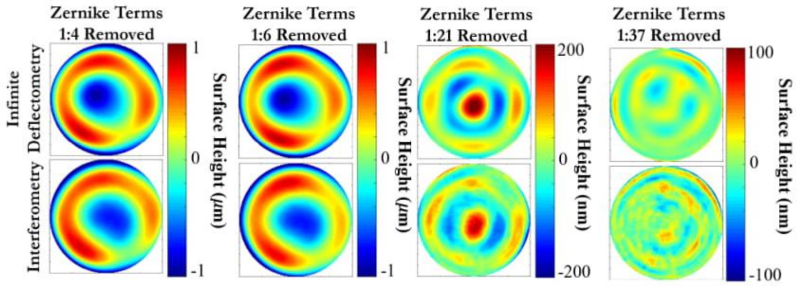

Fig. 7. A fast f/1.26 convex mirror UUT was tested using both the Infinite Deflectometry method (top row) which measured the full 50 mm diameter aperture of the UUT and a commercial Zygo Verifire$^{\mathrm{TM}}$ MST interferometer (bottom row), which measured a limited measurement area of a 45.29 mm diameter aperture on the UUT. Due to uncertainties in both systems for the UUT piston, tip/tilt, and defocus, Zernike terms 1:4 were removed for both reconstruction maps (1st column). Additionally, to better compare the surface reconstruction across spatial frequencies, Zernike terms 1:6 (2nd column), 1:21 (3rd column), and 1:37 (4th column) were removed for both reconstruction maps.

The surface sag RMS values of the reconstructed maps $\mathrm{ID}_{180}^{1:Z}$ and $\mathrm{INT}^{1:Z}$, with Z standard Zernike terms removed, are calculated and reported in Table 1. The values were only calculated over the common 45.29 mm diameter central aperture, to match the 45.29 mm diameter aperture measured by the interferometer.

Table 1. Surface Sag RMS of 45.29 mm Diameter Central Aperture on f/1.26 50 mm Diameter Convex UUT from ID and INT Surface Sag Maps

	Surface RMS Zernike Terms 1:4 Removed (nm)	Surface RMS Zernike Terms 1:6 Removed (nm)	Surface RMS Zernike Terms 1:21 Removed (nm)	Surface RMS Zernike Terms 1:37 Removed (nm)
INT	462.04	447.69	53.71	18.48
ID_{180}	477.34	431.49	56.00	16.26

The $\mathrm{ID}_{180}^{1:Z}$ and $\mathrm{INT}^{1:Z}$ maps showed close agreement across spatial frequencies. Additionally, the RMS surface sage values were very similar. However, due to the overlapping areas tested and the slope stitching, it appears that the ID process performs a slight smoothing process in the reconstructed map. Additionally, some error inherent in phase-shifting deflectometry systems may be negatively impacting the reconstruction accuracy in the infinite deflectometry test. These errors, including positioning uncertainty, have been well explored for PSD based deflectometry measurements [29,33] although a more complete follow up study is required to fully understand the unique errors sources to the infinite deflecomtetry configuration. Finally, the ID process was readily able to achieve a full aperture reconstruction of the highly convex f/1.26 50 mm diameter optic, demonstrating increased testing capabilities for deflectometry.

4.2 Metrology results for Alvarez lens surface

The reconstructed map of the 6 mm optical area of the Alvarez lens as measured by the ID system, $\mathrm{ID}_{\mathrm{Alvarez}}$, and a comparison theoretical (i.e., designed) surface map are given in Fig. 8. Additionally, the height profile as measured by the KLA-Tencor Alpha-Step D-500 profilometer, $\mathrm{S_P}$, and the height of the same profile taken from the $\mathrm{ID}_{\mathrm{Alvarez}}$ map, $\mathrm{S_{ID}}$, are reported.

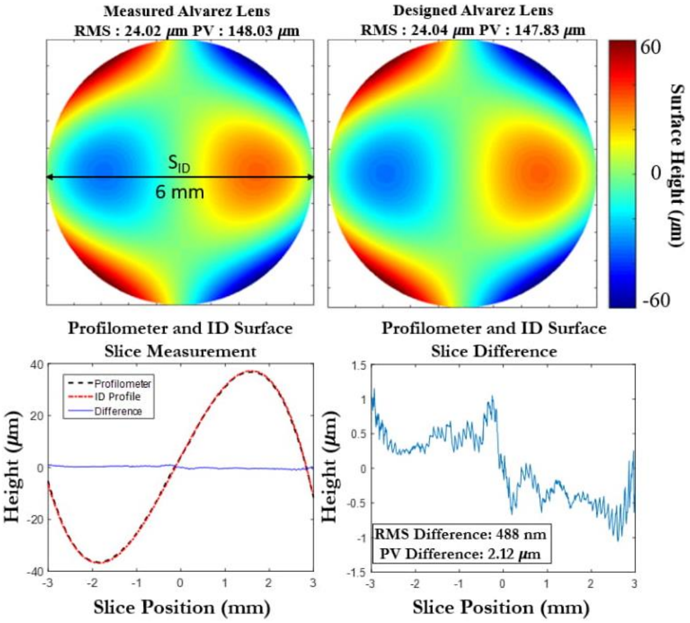

Fig. 8. An Alvarez lens represents a highly freeform surface which presents a unique metrology problem. Using a diamond turning machine a 6 mm diameter Alvarez lens with 17 μm of horizontal coma and −17 μm of trefoil was designed (top right) and manufactured. The final surface generated was measured using the Infinite Deflectometry system with 180 clocking positions (top left). To cross-check the measured data performance, a KLA Alpha-Step D-500 profilometer was used to measure a profile of the optic, shown as a black line in the surface map (top left). The surface height of the profile from the ID measurement, and the profilometer were compared (bottom left) and the difference was calculated (bottom right).

Standard Zernike terms 1:37 were fit to the $\mathrm{ID}_{\mathrm{Alvarez}}$ map, and the designed term values (i.e., ideal surface) are compared in Fig. 9. The RMS surface deviation from ideal design was 2.75 μm with Zernike terms 1:4 removed, 1.78 μm with terms 1:8 removed, 178 nm with terms 1:21 removed, and 160 nm with terms 1:37 removed.

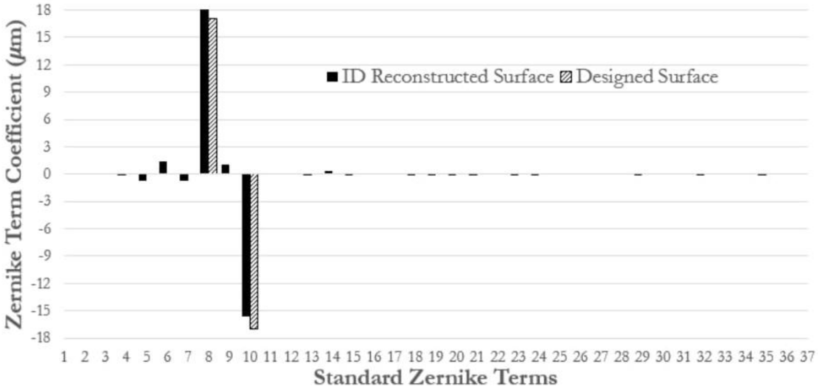

Fig. 9. Using a CNC diamond turning process, a 6 mm diameter Alvarez lens was generated on a PMMA disk and measured. The infinite deflectometry surface map was fitted with standard Zernike terms 1:37 (black bars). This was compared to the Zernike terms representing the design values (checked bars).

The Infinite Deflectometry system was able to achieve a full aperture surface reconstruction of the Alvarez lens, a 6 mm diameter freeform generated in a PMMA disk. The surface had ~148 μm PV of surface height variation over it. The reconstructed map was similar to the ideal surface, however, the measurement reported small amounts of Zernike terms Z5, Z6, and Z9, which represent vertical and 45-degree astigmatism and vertical trefoil respectively. Additionally, the magnitude of Z8 and Z10 in the reconstructed surface did not exactly match the designed surface. This is not unexpected for the manufacturing tolerance of machining performed for the surface. For an independent verification, a profilometer measurement of a profile of the surface was in close agreement to the same slight from the reconstructed ID surface, with 488 nm RMS difference.

5. Conclusion

While deflectometry historically has provided a powerful non-null metrology method for measuring concave optics, convex and even large flat optics have proven challenging to measure. This is due to the requirement that the source area in a deflectometry test must be large enough to allow for some light from the source to be collected by the camera, after it is deflected by the UUT. For flat to convex optics, or highly freeform optics, extremely large source areas are required to measure the full UUT area. As an alternative, we have presented Infinite Deflectometry, which utilizes a standard camera and digital display, along with a precision rotation stage which the UUT is placed upon, to create a series of virtual sources, thereby expanding the dynamic range of the slope measurement. When taken together, these virtual screens create a tipi shaped source which completely encloses the UUT and allows for testing a 'infinite' range of surface slopes.

A demonstration system successfully produced a high accuracy full aperture surface reconstruction map results of a highly convex f/1.26 50 mm diameter spherical optic, as well as testing a highly freeform Alvarez lens. The ID method represents another deflectometry system modality which extends the measurement capabilities of the deflectometry technique. We do not claim the ID method is superior to other precision metrology techniques such as interferometry. Instead, our goal is to improve the fundamental deflectometry technique to provide more value to the optics metrology community by providing multiple options and cross-checking metrology solutions.

Funding

II-VI Foundation Block-Gift Program; Technology Research Initiative Fund Optics/Imaging Program; Korea Basic Science Institute Foundation; Friends of Tucson Optics Endowed Scholarships in Optical Sciences.

References

1. M. Beier, S. Scheiding, A. Gebhardt, R. Loose, S. Risse, R. Eberhardt, and A. Tünnermann, "Fabrication of high precision metallic freeform mirrors with magnetorheological finishing (MRF)," *Optifab 2013.* International Society for Optics and Photonics **8884**, 88840S (2013).
2. S. Risse, S. Scheiding, M. Beier, A. Gebhardt, C. Damm, and T. Peschel, "Ultra-precise manufacturing of aspherical and freeform mirrors for high resolution telescopes," *Optifab 2014.* International Society for Optics and Photonics **9151**, 91510M (2014).
3. T. Blalock, K. Medicus, and J. D. Nelson, "Fabrication of freeform optics," *Optical Manufacturing and Testing XI*. International Society for Optics and Photonics **9575**, 95750H (2015).
4. D. Gurganus, J. D. Owen, B. S. Dutterer, S. Novak, A. Symmons, and M. A. Davies, "Precision glass molding of freeform optics," *Optical Manufacturing and Testing XII*. International Society for Optics and Photonics **10742**, 107420Q (2018).
5. S. C. West, R. Angel, B. Cuerden, W. Davison, J. Hagen, H. M. Martin, D. W. Kim, and B. Sisk, "Development and Results for Stressed-lap Polishing of Large Telescope Mirrors1," *Classical Optics 2014 (2014), Paper OTh2B.4* (Optical Society of America, 2014), p. OTh2B.4.
6. I. Trumper, B. T. Jannuzi, and D. W. Kim, "Emerging technology for astronomical optics metrology," Opt. Lasers Eng. **104**, 22–31 (2018).
7. D. W. Kim, M. Aftab, H. Choi, L. Graves, and I. Trumper, "Optical Metrology Systems Spanning the Full Spatial Frequency Spectrum," (Optical Society of America, 2016), FW5G.4.

8. M. B. Dubin, P. Su, and J. H. Burge, "Fizeau interferometer with spherical reference and CGH correction for measuring large convex aspheres," (2009), 7426, 74260S–74260S–10.
9. S. Scheiding, M. Beier, U.-D. Zeitner, S. Risse, and A. Gebhardt, "Freeform mirror fabrication and metrology using a high performance test CGH and advanced alignment features," *Advanced Fabrication Technologies for Micro/Nano Optics and Photonics VI*. International Society for Optics and Photonics **8613**, 86130J (2013).
10. R. Huang, P. Su, J. H. Burge, L. Huang, and M. Idir, "High-accuracy aspheric x-ray mirror metrology using Software Configurable Optical Test System/deflectometry," OE, OPEGAR **54**(8), 084103 (2015).
11. D. W. Kim, C. Oh, A. Lowman, G. A. Smith, M. Aftab, and J. H. Burge, "Manufacturing of super-polished large aspheric/freeform optics," (2016), Vol. 9912, pp. 99120F–99120F–9.
12. J. Burke, W. Li, A. Heimsath, C. von Kopylow, and R. B. Bergmann, "Qualifying parabolic mirrors with deflectometry," J. Eur. Opt. Soc. Rapid Publ. **8**, 13014 (2013).
13. C. J. Oh, A. E. Lowman, M. Dubin, G. Smith, E. Frater, C. Zhao, and J. H. Burge, "Modern technologies of fabrication and testing of large convex secondary mirrors," *Advances in Optical and Mechanical Technologies for Telescopes and Instrumentation II*. International Society for Optics and Photonics **9912**, 99120R (2016).
14. S. Chen, S. Xue, Y. Dai, and S. Li, "Subaperture stitching test of convex aspheres by using the reconfigurable optical null," Opt. Laser Technol. **91**, 175–184 (2017).
15. Z. Tian, W. Yang, Y. Sui, Y. Kang, W. Liu, and H. Yang, "A high-accuracy and convenient figure measurement system for large convex lens," Opt. Express **20**(10), 10761–10775 (2012).
16. Y. Chen, E. Miao, Y. Sui, and H. Yang, "Modified Sub-aperture Stitching Algorithm using Image Sharpening and Particle Swarm Optimization," J. Opt. Soc. Korea. **18**, 341–344 (2014).
17. Y.-C. Chen, C.-W. Liang, H.-S. Chang, and P.-C. Lin, "Reconstruction of reference error in high overlapping density subaperture stitching interferometry," Opt. Express **26**(22), 29123–29133 (2018).
18. L. Zhang, D. Liu, T. Shi, Y. Yang, S. Chong, B. Ge, Y. Shen, and J. Bai, "Aspheric subaperture stitching based on system modeling," Opt. Express **23**(15), 19176–19188 (2015).
19. D. Castán-Ricaño, F. S. Granados-Agustín, E. Percino-Zacarías, and A. Cornejo-Rodríguez, "Increase in the measurement of the normal vectors of an aspherical surface used in deflectometry," *Modeling Aspects in Optical Metrology VI*. International Society for Optics and Photonics **10330**, 103301W (2017).
20. I. Scheele, S. Krey, and J. Heinisch, "Measurement of aspheric surfaces with 3D-deflectometry," *Optifab 2007: Technical Digest*. International Society for Optics and Photonics **10316**, 103160P (2007).
21. C. J. Oh, A. E. Lowman, G. A. Smith, P. Su, R. Huang, T. Su, D. Kim, C. Zhao, P. Zhou, and J. H. Burge, "Fabrication and testing of 4.2m off-axis aspheric primary mirror of Daniel K. Inouye Solar Telescope," *Advances in Optical and Mechanical Technologies for Telescopes and Instrumentation II*. International Society for Optics and Photonics **9912**, 99120O (2016).
22. R. Huang, P. Su, T. Horne, G. B. Zappellini, and J. H. Burge, "Measurement of a large deformable aspherical mirror using SCOTS (Software Configurable Optical Test System)," *Optical Manufacturing and Testing X*. International Society for Optics and Photonics **8838**, 883807 (2013).
23. J. Balzer, D. Acevedo-Feliz, S. Soatto, S. Höfer, M. Hadwiger, and J. Beyerer, "Cavlectometry: Towards Holistic Reconstruction of Large Mirror Objects," *2014 2nd International Conference on 3D Vision* 448–455(2014).
24. P. Candry and B. Maximus, "Projection displays: New technologies, challenges, and applications," J. Soc. Inf. Disp. **23**(8), 347–357 (2015).
25. J.-W. Huang, "Design and Fabrication of Ultra-Short Throw Ratio Projector Based on Liquid Crystal on Silicon," Liquid Crystals - Recent Advancements in Fundamental and Device Technologies (2018).
26. B. Martin, J. Burge, S. Miller, S. Warner, and C. Zhao, "Fabrication and Testing of 8.4 m Off-Axis Segments for the Giant Magellan Telescope," (Optical Society of America, 2008), p. OWD6.
27. H. M. Martin, R. G. Allen, J. H. Burge, J. M. Davis, W. B. Davison, M. Johns, D. W. Kim, J. S. Kingsley, K. Law, R. D. Lutz, P. A. Strittmatter, P. Su, M. T. Tuell, S. C. West, and P. Zhou, "Production of primary mirror segments for the Giant Magellan Telescope," *Advances in Optical and Mechanical Technologies for Telescopes and Instrumentation* (International Society for Optics and Photonics, 2014), Vol. 9151, p. 91510J.
28. A. E. Lowman, G. A. Smith, L. Harrison, S. C. West, and C. J. Oh, "Measurement of large on-axis and off-axis mirrors using software configurable optical test system (SCOTS)," *Advances in Optical and Mechanical Technologies for Telescopes and Instrumentation III*. International Society for Optics and Photonics **10706**, 107061E (2018).
29. R. Huang, "High precision optical surface metrology using deflectometry," Ph.D., The University of Arizona (2015).
30. W. H. Southwell, "Wave-front estimation from wave-front slope measurements," J. Opt. Soc. Am. JOSA **70**(8), 998–1006 (1980).
31. W. Zhao, L. R. Graves, R. Huang, W. Song, and D. Kim, "Iterative surface construction for blind deflectometry," *8th International Symposium on Advanced Optical Manufacturing and Testing Technologies: Optical Test, Measurement Technology, and Equipment* (International Society for Optics and Photonics, 2016), **9684**, p. 96843X.
32. L. R. Graves, H. Choi, W. Zhao, C. J. Oh, P. Su, T. Su, and D. W. Kim, "Model-free deflectometry for freeform optics measurement using an iterative reconstruction technique," Opt. Lett., OL **43**, 2110–2113 (2018).

APPENDIX C
Scalable Time-Modulated Precision Infrared Source for Infrared Deflectometry

Logan Rodriguez Graves, Henry Quach,
and Dae Wook Kim

In Press in Optics Express.

High contrast thermal deflectometry using long-wave infrared time-modulated integrating cavity

LOGAN R. GRAVES,[1] HENRY QUACH[1], R. JOHN KOSHEL[1], CHANG-JIN OH[1], DAE WOOK KIM[1,2,*]

1 James C. Wyant College of Optical Sciences, University of Arizona, 1630 E. University Blvd., Tucson, AZ 85721, USA
2 Department of Astronomy and Steward Observatory, University of Arizona, 933 N. Cherry Ave., Tucson, AZ 85719, USA
** letter2dwk@hotmail.com*

Abstract: We introduce a scalable temporally modulated long wave infrared source design. The design makes use of time modulated blackbody heating elements which are input sources into a custom aluminum integrating cavity. The output of the box is a rectangular slit, built to match the traditional tungsten ribbon design for an infrared deflectometry source. Temporal modulation allows for signal isolation and improved resilience to background fluctuations in an infrared deflectometry source. Infrared deflectometry measurements using the new source design and a traditional tungsten ribbon, both with similar radiant flux, were compared for a ground glass surface, an aluminum blank, and an aluminum blank under thermal load (300 ° C). Signal to noise ratio was ~4 times higher for the new design, as well as improved source stability and geometry. Further, the new design successfully measured the previously untestable hot aluminum flat. The new design improves infrared deflecomtetry and allows for deflectometry measurements of optics under thermal load.

1. Introduction

As manufacturing methods continue to improve, a wider range of materials are being shaped into custom freeform surfaces for new optical applications. These materials, which include metals, glass, ceramics, and plastics, are turned into high performance optics using grinding and polishing methods, computer numeric control (CNC) diamond turning, sub-aperture polishing methods, 3D printing, and more [8,9,45,53,54]. To assure proper fabrication, advanced metrology technologies must be used. This allows for monitoring and guiding of the fabrication process, and final verification of the optical surface shape.

Typically, interferometry and deflectometry are used for high accuracy and precision metrology of freeform optics [37,45,54,55]. Interferometry is a null metrology method, which requires using a null optic as a reference measurement to the unit under test (UUT). For freeform optics in particular, computer generated holograms (CGH) have become highly attractive for use as a null optic as they can generate a freeform null and additionally can provide advanced alignment features [15]. Unfortunately, a CGH can only null a designed specific optical configuration, and they typically can be expensive to fabricate. Deflectometry is a non-null test method, in a which a source presents a known pattern, which specularly reflects from the UUT and is recorded by a camera. By knowing the geometry of all components to high precision the local slopes of the UUT can be determined and integrated to generate a reconstructed surface map. Particularly for extremely large optics, such as telescope optics, fabrication is typically achieved using grinding and polishing [5,54,56,57]. The grinding phase of generating optics offers a unique period during which rapid removal of material is performed, allowing for faster convergence to the final desired surface shape, with removal rates being up to thousands of times faster than during polishing. During the period, the optical surface root mean square (RMS) roughness can range from hundreds of microns down to 1 micrometer, and the surface shape can change significantly. The rough surface is not specularly reflective to visible wavelengths, making measurements challenging. Utilizing an infrared system is a desirable solution to grinding phase metrology as the rough surface will be specularly reflective at longer wavelengths. While infrared interferometers exist which could achieve this measurement [58], the rapidly changing surface shape during the grinding phase requires equally rapidly changing custom null optics. Instead, deflectometry has been used with an infrared source to measure such rough surfaces [37,59].

A key challenge in designing infrared deflectometry systems is in the choice of a thermal source. Ideally, a deflectometry source will provide a high signal to noise ratio for the system, while having high spatial modulation accuracy and capabilities and excellent stability. One possible source design is to apply current to a thin tungsten ribbon, which induces joule heating and creates a rectangular, pseudo-blackbody emitting source. By scanning the ribbon in orthogonal directions, a line scanning source is created. This ribbon design formed the basis for the scanning long wave optical test system, SLOTS, which has been used extensively in infrared deflectometry, and the tungsten ribbon source, with minor variations, is still the traditional source used for infrared deflectometry [37,46]. However, a tungsten ribbon has some significant limitations when applied to deflectometry.

In a deflectometry system, any uncertainty in the shape and position of all components directly reduces the accuracy in the final optical surface reconstruction. For a tungsten ribbon, low order bending modes frequently occur, particularly as the ribbon experiences thermal gradients and load. Thus, the idealized flat rectangular shape of the ribbon, used for data processing and surface reconstruction of deflectometry data measurements, may be incorrect and can lead to surface reconstruction errors. Further, the source output is assumed to be uniform across the ribbon, and stable over the testing period. However, tungsten evaporates and degrades with use over time, leading to a potentially non-uniform emission profile across the surface. This is coupled with the challenge that the ribbon's power draw and emission may fluctuate with time. One final consideration is the limit to how much output power can be achieved with a ribbon source. Because the ribbon acts as a pseudo-blackbody source, applying more power to raise the signal power will shift the output spectrum to lower wavelengths, away from the desirable longer wavelength, and above a certain point the load will be too great for the ribbon to handle, leading to a failure in the source. These comments are not meant to diminish the impact the tungsten ribbon had on infrared deflectometry specifically, and metrology generally. Without the introduction of the tungsten ribbon source, high accuracy, rapid and efficient in-situ testing of diffuse optics was challenging, time consuming, and extremely expensive. Instead, these known limitations to the tungsten ribbon layout a clear framework of considerations that must be addressed to produce an improved infrared deflectometry system at the source level.

We have created a new source design which addresses these prior issues and opens a new region of infrared deflectometry testing. The source is a long wave infrared time modulated integrating cavity (LITMIC), which uses modular high efficiency and high stability resistive membrane blackbody elements. Due to the modular design, the number of elements, referred to as 'caps', inputting radiation into the integrating cavity are readily scalable. The light is output via a machine cut slit, whose geometry is stable and known to machining precision. Finally, a key feature of the LITMIC design is the ability to temporarily modulate the source at up to 1 Hz, providing an infrared time modulated signal, which allows for isolation of the signal relative to background noise during a test. The new source was modeled and optimized using illumination design software, and the final optimized design was built and used to measure a diffuse glass and an aluminum blank surface. A comparison was made using a traditional deflectometry tungsten ribbon source, whose shape was identical to the exit slit of the box, using the same setup and camera. This allowed for direct comparison of the two sources. Finally, an aluminum flat under high thermal load, which has historically been unmeasurable using a traditional source for infrared deflectometry, was successfully measured using the LITMIC source.

2. Background Theory

2.1 Deflectometry

Deflectometry represents a non-null optical metrology method which can, using careful calibration, produce highly accurate surface reconstruction of optics. The metrology method measures the local slope of a unit under test (UUT), and these local slopes are integrated in post-processing to reconstruct the surface map. With proper calibration, deflectometry can provide surface measurements with an accuracy comparable to interferometry [4].

Due to the non-null nature of the test, deflectometry can measure a wide dynamic range of surface slopes. The key limiting factors in a deflectometry test for what is measurable are defined by the source size, the camera field of view (FOV), and whether the tested UUT surface can reflect the light emitted from the source. For an area on the UUT to be testable it must be in the FOV of the camera. Further, by tracing a ray from the camera to any mirror pixel, the ray, following the law of reflection, must then after deflection intercept some point on the source area. This assures that the extend of the source is great enough to fully measure the UUT surface, although techniques exist to assure this can be satisfied for most any surface [60]. Finally, the light emitted from the source must be specularly reflected from the surface of the UUT.

In most deflectometry setups, a high-resolution camera with a well-defined entrance pupil location is used, with the camera entrance pupil location referred to as $c(x,y,z)$. The camera is focused onto the UUT surface, such that the camera pixels are mapped to the UUT surface and represent discrete 'mirror pixels', referred to as $u(x,y,z)$, over which the local slopes will be calculated. Ideally, the source for a deflectometry setup has well defined spatial emittance, allowing for accurate knowledge of the geometry of $s(x,y,z)$, and has high repeatability and stability. Additionally, it is advantageous to have a source with high signal power, which provides the test system with a high signal-to-noise ratio (SNR). For every camera pixel, the precise location on the source that successfully illuminated the camera pixel is determined during the measurement. Taking this data, using the ray start location at the source, the end location at the camera, and the intercept location at the mirror pixel, the local slope at the mirror pixel can be determined. This process is extended to all pixels to measure the local slopes at all mirror pixels on the UUT in orthogonal directions, referred to as $S_X(x,y,z)$ and $S_Y(x,y,z)$, representing the x and y slopes respectively. These slope maps are integrated, typically done using a zonal integration method such as Southwell integration [61] or a modal integration such as using a gradient Chebyshev polynomial set [62], resulting in a reconstructed surface map. Figure 1 demonstrates a standard deflectometry setup and the model used for local slope calculation.

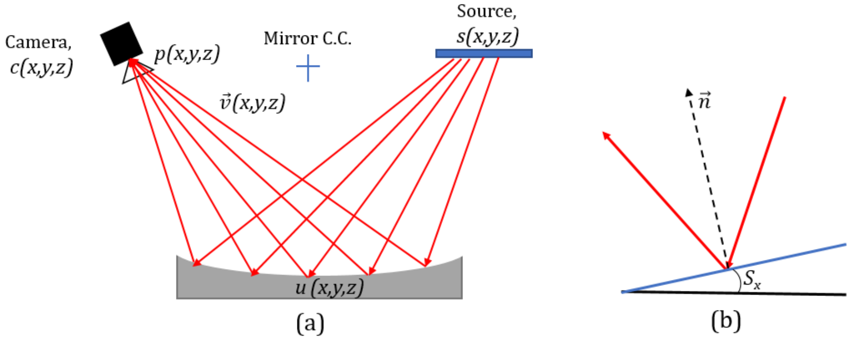

Figure 1. A traditional deflectometry system relies on a source, *s(x,y,z)*, which emits light with a well-known spatial definition. Some of the light rays, defined as vectors *v(x,y,z)*, successfully deflect from the UUT, *u(x,y,z)*, and are captured by a camera, *c(x,y,z)*, whose entrance pupil location, *p(x,y,z)*, is well known. Typically, the source and camera are place as close to the center of curvature (C.C.) as possible to approach a one-to-one imaging scenario, as shown in (a). By knowing the precise coordinates of the ray origin at the source, the ray intercept at the UUT, and the ray end at the camera, a local slope at the ray intercept can be determined in the x and y directions, referred to as S_x and S_Y respectively (b).

Uncertainty in the location of any components in the system will reduce the accuracy of the local slope calculations, and thus the surface reconstruction process. Therefore, it is important to know the position and geometry of all components to a high degree of certainty. While this is readily accomplished for the camera, using calibration and measurement methods such as a coordinate measurement machine (CMM) or even a laser tracker, for the source it can be more challenging, as the source is significantly larger than the camera pupil and, in a scanning source design, will have additional mechanical uncertainties. Further, the source emission uniformity and stability are extremely important, as any uncertainty in the source behavior with degrade local slope calculations [46,47]. These issues are readily addressed in visible deflectometry systems, which benefit from the use of high resolution, high performance digital displays. However, for infrared deflectometry, the problem becomes more challenging.

2.2 Infrared Deflectometry

Infrared deflectometry extends deflectometry to measuring diffuse rough optics which are challenging to measure using traditional techniques. There exists a wide range of materials which do not specularly reflect visible light, thus, infrared deflectometry is an important metrology tool. This is particularly true for the grinding phase of mirror fabrication, where a rough grit is used to rapidly grind the UUT down to the final desired surface shape. During this period the root-mean-square (RMS) surface roughness will typically drop from 1000 μm to 1 μm as smaller grit sizes are used. For such rough surfaces, visible light is scattered and thus visible spectrum metrology tools are inapplicable; however, infrared deflectometry has been applied during this phase successfully for several mirror fabrication projects, including the Daniel K. Inouye Solar Telescope (DKIST) primary mirror [37].

The test setup used for most infrared deflectometry systems relies on a rectangular source which is scanned in the x and y orthogonal directions. The longer the emission wavelength of the source, the rougher the surface that can be tested, provided the source power is high enough and a suitable camera for the given wavelength range can be used. Traditionally, a heated tungsten ribbon acts as the source, serving as a pseudo-blackbody element. Coupled with a long-wave infrared (LWIR) camera, which is sensitive in the 7-14 μm range, this allows for testing 1 μm to ~ 25 μm RMS rough surfaces. This test setup has been successfully deployed and used to measure a variety of rough, non-specularly reflecting surfaces and was able to achieve high accuracy surface reconstruction [21,37,38,45,46]. It should be noted that other dynamic heated screen patterns, including a scanning infrared laser and a resistor array, have successfully been used as sources for infrared systems, however, based on the literature a heated scanning ribbon still serves as the most common source for testing large diffuse optics [63]. An example case showing the rough 4.2 m diameter off-axis parabola DKIST primary mirror surface during testing, as well as the reflected LWIR light from a scanning tungsten ribbon as captured by a LWIR camera for a deflectometry measurement of the UUT are shown below in figure 2.

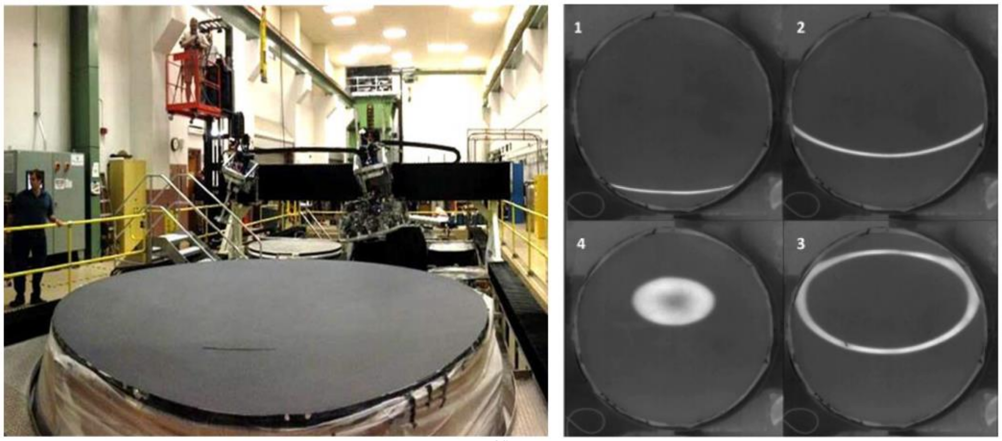

Figure 2. After generating a mirror blank, the surface goes through a grinding process, which rapidly converges the UUT to the desired shape. For the DKIST primary, a 4.2 m Zerodur blank was ground from ~100 μm down to 1 μm RMS surface roughness. During this process, the rough surface (left) was measured using infrared deflectometry. The infrared deflectometry system uses a scanning heated tungsten ribbon and captures reflected light in the 7-12 μm range (right), which is specularly reflected by the rough surface.

Just as with visible deflectometry, the uncertainty in all components directly affects the accuracy of the surface reconstruction. In the LWIR region, camera choices are more limited than the visible, and the most common detector type is a microbolometer array, which typically have large pixels than CCD or CMOS detectors. However, the diffraction limit in the LWIR region is also approximately an order of magnitude larger than the visible spectrum, thus, the pixel pitch is not a limiting factor. Additionally, accurate knowledge of the source shape and position can become highly challenging if not impossible to measure, as will be explored in the next section.

Finally, the source signal as compared to the background, which broadly is captured by the term signal to noise (SNR) ratio, is a key characteristic of the source. All objects radiate to some extent in the infrared region, thus, there is a large amount of background thermal radiation both in and out of scene that contributes significantly to the noise levels during an infrared deflectometry test. Further, the background radiation may change during the test. A simple and traditionally used pre-test background image (or average of background images), may not always be enough to remove the background noise during testing. This issue is especially clear when considering that the source itself is moving during the test and may leave a thermal 'tail' in the air, as well as introduce a shifting background emitter in the form of the housing hardware. The noise issue is compounded by the fact that, for a heated metal source, there is a clear limit to how much signal output power can be achieved before failure of the source. Lastly, the output power uniformity and stability are highly important, as any variation during testing will skew results and impart uncertainty into the final reconstructed surface.

2.3 Time Modulated Infrared Integrating Box Source

With these considerations in mind, we have developed an infrared source which addresses the previously covered limitations of a tungsten ribbon source and allows for novel testing situations for infrared deflectometry. The source is a long wave infrared time modulated integrating cavity (LITMIC) which uses modular heating elements as input radiation and has a rectangular output slit where the light is emitted, mimicking the ribbon source dimensions for direct comparison. It should be noted; the cavity and emission area were selected for comparison to a tungsten ribbon source and can be readily changed and optimized to other geometries for different testing configurations. The design provides high signal output power, excellent uniformity and signal stability. Because it is a machined output slit, the source geometry is known to machining precision.

The LITMIC source makes use of small resistive caps, which contain an extremely thin resistive alloy membrane that exhibits high emissivity can cool extremely quickly. Thus, the source can be temporally modulated, achieving an 80% contrast ratio at 1 Hz. This allows for in-situ updated background noise images during testing, as the signal output can be modulated to capture 'background' and 'signal' images during the scanning. Further, although not implemented in this setup, a detector which provides direct signal output, and does not integrate the signal, could be used to filter the signal in the Fourier domain to further isolate the signal from noise, although, due to the available camera in this study, this approach was not implemented.

The integrating cavity can be machined out of any material which will maintain shape and diffusely reflect the LWIR being input into the cavity, although consideration of the inner cavity dimensions must be made to assure that the light is properly scattered interiorly to achieve a uniform non-directional emission from the exit slit. Further, the interior of the cavity may be coated, depending on the cavity material, to adjust the radiant flux by minimizing reflection losses, and the number of input caps can be adjusted as well to scale radiant flux. Finally, the emission slit geometry can be altered, although again the interior cavity design must be properly configured to assure proper emission behavior.

With considerations towards matching the geometrical and radiometric properties of a tungsten ribbon source, an integrating cavity source was designed and machined. The cavity was designed with 20 input 'cap' sources, operating at approximately 70% maximum power for safety and to achieve a 1 Hz flicker rate. The cavity itself was optimized to achieve uniformity over a rectangular exit, while the interior of the cavity was a box shape made of bare aluminum with a surface roughness of 3.4 μm. The design was modeled to match a traditional tungsten ribbon source which has been used in previous infrared deflectometry test [64] for comparison purposes. The matching of the slit and ribbon dimensions allows for direct comparison of the two sources. The system was modeled in Light Tools, and the location of the heating elements, as well as interior cavity dimensions and surface roughness, were optimized to achieve a uniform power output across the exit slit while maintaining non-directional output over approximately 2π steradians. The output was simulated at the slit, where uniform power was the goal. The near field irradiance pattern, as well as the final optimized box design, are shown below in figure 3.

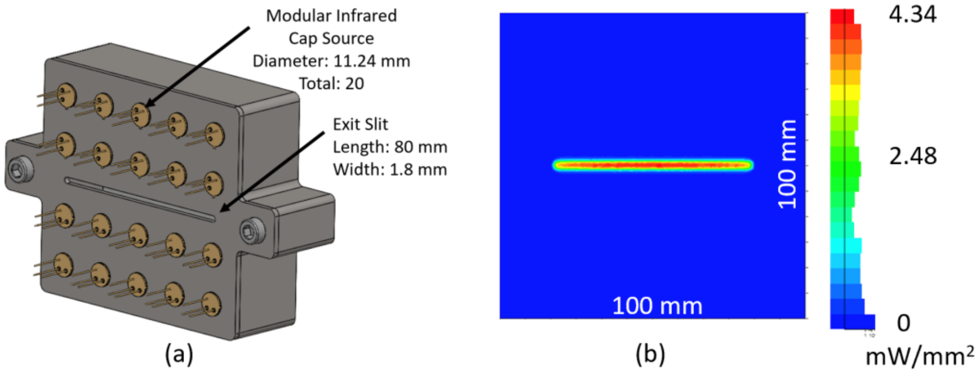

Figure 3. An aluminum integrating box was designed and optimized to make an infrared source. The box was designed to have 20 input source ports, where small, high emissivity, modular and time modulating infrared cap sources were input in the final built box. An emission exit slit, where light would leave the box, was designed to match the dimensions of a comparison tungsten ribbon infrared source (a). The optimized design was modeled in Light Tools, where the irradiance at the surface of the box was simulated to assure high uniformity across the exit slit (b).

2.4 Comparative Radiometric Modeling

For the purposes of a direct comparison, the source power of the integrating cavity design was matched to that of the tungsten ribbon. The tungsten ribbon behaves as a pseudo-blackbody emitting source, and the radiometric equations predicting the ribbon emission have been well documented [47]. The integrating cavity designed and built features a bare aluminum internal cavity, with an RMS surface roughness of approximately 3.4 μm, and when the source elements were activated, the emission slit acts as a black body emitting source, which emits roughly over 2π steradians. Further, each source features the same emission area and were linearly scanned for testing. The raw data acquisition is from the pixel camera detector pixel response, where a centroiding process is used to extract the peak signal response for every camera pixel as a function of source location Thus, as all other components are identical in a system other than the sources, the goal was to match the source radiance.

As has previously been described [21,48,49], using the law of error propagation, when only noise Ii is considered, the centroid uncertainty, σ, is determined from the recorded intensity response width, w, the number of samples taken, N, and the SNR:

$$\sigma = \frac{w}{\sqrt{N}\, SNR} = \frac{w}{\sqrt{N}\ P_{sig}/NEP}, \ [1]$$

P_{sig} is the signal power and *NEP* is the noise equivalent power, which is typically the dominant factor in an infrared deflectometry test. The centroid uncertainty directly relates to the slope uncertainty as:

$$\Delta s \cong \frac{\sigma}{2Z}\text{, [2]}$$

Where Z is the distance from the source to the UUT. The signal power is determined by considering the reflected radiance, L_{ref}, the diameter of the camera aperture, D_{ap}, the source width, w_{sc}, and the camera focal length, f, given by:

$$P_{sig} = \tau_o L_{ref} A_{im} \Omega_{pix} = \tau_o L_{ref}\ (w_{sc} D_{ap})\ \frac{A_{pix}}{f^2}\text{, [3]}$$

The reflected radiance, L_{ref}, is derived from the source radiance, L_{src}, and is scaled by the reflectivity of the UUT, r_U, and the relative reflectance due to rough surface scattering, r_s. The value is calculated according to:

$$L_{ref} = r_a\ r_s\ L_{srce}\text{, [4]}$$

To this point, the tungsten ribbon and the integrating cavity design share the same radiometric considerations. The primary difference arises in the different source radiance, defined as L_{src_ribbon} and L_{src_cavity} for the ribbon and cavity respectively. The ribbon source radiance is given by:

$$L_{srce\_ribbon} = \frac{\varepsilon^r\ \alpha_{7-14}^r\ P_{ribbon}}{\pi A_{srce}}\text{, [5]}$$

Where the total power from the power supply, P_{ribbon}, is scaled by the emissivity of the source over the given radiation band, ε_r., which is 0.10 [47,50,51] For the ribbon configuration used, the power draw was approximately 2.1 W (2.2 A, 0.95 V), with an operating temperature of roughly 440 ° C. The portion of the total radiation in the 7-14 µm band, α_{7-14}^r, is calculated from Stefan-Boltzmann law. Finally, the solid angle is given by $\pi = 3.14\ rad$, which is the solid angle when a differential plane source radiates towards a hemisphere and the surface area of the source, A_{src}, is directly calculated from the source geometry. The source radiance for the cavity is similar to that of the ribbon with some minor differences. This is given by:

$$L_{srce\_cavity} = r_c^b\ \frac{\varepsilon^c\ \alpha_{7-14}^c\ N\ P_{cap}}{\pi A_{srce}}\text{, [6]}$$

Where the input power is given by the power per cap source, P_{cap}, which for the designed cavity was approximately 0.35 W (23.8 V, 14 mA), with a temperature of 450 °C, and is scaled by the total number of caps inputting energy into the cavity, N, which for the presented design was 20. The emissivity and radiation are unique to the cap source and are designated as ε^c and α_{7-14}^c respectively. Finally, the total output radiance from the cavity is scaled by the reflectivity of the cavity interior, r_c, which for bare aluminum at the operating temperature is approximately 0.93 [52] to the power of the average number of bounces taken by a ray from a source cap to exiting the box, b, which for the given design was approximately 46, as calculated in the Light Tools model.

It should be noted that while minor parameters differ between the source radiance definitions for both a heated metal-based source and the LITMIC source, the most fundamental difference is the power scalability of the LITMIC source. Blackbody sources will shift their emission spectrum to higher energy, lower wavelengths as the input power, and thus temperature, increases. This is non-ideal for a long-wave infrared source. Further, there is an input power threshold for all materials, above which the material will fail. As seen in equation 6, the same long-wave infrared spectrum can be maintained while adding power to the source by scaling the number of sources, which is a unique feature for the LITMIC source.

The parameter values for the as designed and manufactured LITMIC source, as well the tested tungsten ribbon, are provided in table 1. The specific details of the source's implementations are provided in later sections.

Table 1. Source Parameters for Infrared Deflectometry

Parameter	Notation	Value	Unit
Tungsten Ribbon power total consumed	P_{tot}	2.10	W
Single cap power total consumed	P_{cap}	0.35	W
Tungsten Ribbon Radiation in 7-14 um band	α_{7-14}^r	0.28	N/A
Cavity Radiation in 7-14 um band	α_{7-14}^c	0.28	N/A
Tungsten Ribbon Source Emissivity	ε^r	0.10	N/A
Cavity Source Emissivity	ε^c	0.90	N/A
Cavity Reflectivity (Bare Al)	r_c	0.93	N/A
Cavity average ray bounces	b	46	N/A

Source surface area (for both sources)	A_{src}	1440	mm^2
Ribbon source radiance	L_{srce_ribbon}	1.36×10^{-5}	$W/mm^2/sr$
Cavity source radiance	L_{srce_cavity}	1.38×10^{-5}	$W/mm^2/sr$

It must be noted that in the final test, the input power to the cavity and the ribbon were altered slightly to achieve an average identical power signal on a camera pixel from both sources. This is due to the goal of having like comparisons between the two sources; the goal was not to compare the power output from the sources, which can be significantly adjusted via engineering choices.

3. Experimental Setup and Measurements

An infrared deflectometry system was assembled on an optical table. The camera featured a ~1 - 2 m variable focal length germanium lens, and the detector was a microbolometer array with 640x320 pixels (7-14 μm response, Thermal-Eye 3500AS). The exposure, gain, and level settings were adjusted prior to testing such that the output was never saturated, and the settings were held constant between all tests. An optical mount was situated approximately one meter from the camera and was fixed in place and allowed for repeatable placed of the UUT. The camera was focused on the UUT surface for deflectometry measurements and was focused on the sources for measurements of the source properties.

The source was the only component in the system which changed. To compare properties between source modalities, a scanning platform was utilized with a mounting interface to interchange LWIR sources. A motorized lead screw stage (Velmex BiSlide, Model #MN10-0350-M02-31) moved source assemblies in the vertical direction with an absolute positional accuracy of ±0.005 mm. For ease of comparison, sources shared identical slit dimensions (75 x 2.5 mm) and radiant exitance planes. Figure 4 demonstrates the camera and source setup for the test system.

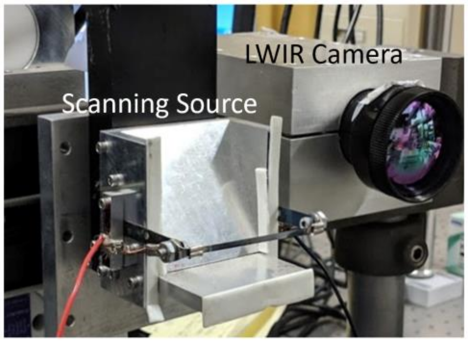

Figure 4. The infrared testing system used for all tests in this manuscript was composed of a linear scanning source (left) and a long wave infrared camera (right). The source was mounted in a kinematic mount, allowing for repeatable interchange between a tungsten ribbon source, as seen above, and the LITMIC source.

3.1. Infrared Source Structure and Setup

A LWIR thermal line source was implemented by running direct current (2.2 A, 2.1 W) across a thin tungsten ribbon. Transient thermal noise from the wire, such as the local heating of air, was reduced by taking measurements after the ribbon reached an equilibrium state (~5 minutes), closer to the environmental thermal steady-state condition.

The LITMIC source was implemented by applying a (0.24 A, 7W) load to a circuit consisting of 20 emitters (Axetris Model: EMIRS200 T039 w/ Cap; 2 to 14 μm spectrum, ~ 2π steradian emission). Pointed into the enclosure, the rectangular emitter array was operated by binary power cycling with a digitally controlled relay (Numato 1 Channel USB-Powered Relay Module). Enclosure walls were machined from bare Al 6061-T6 and characterized to 3.4 μm RMS by a Zygo NewView 8300 Interference Microscope. Finally, aluminum-covered “gull-wing” shields were added to block excess thermal noise from the slit source plane. Figure 5 demonstrates the integrating cavity after assembly.

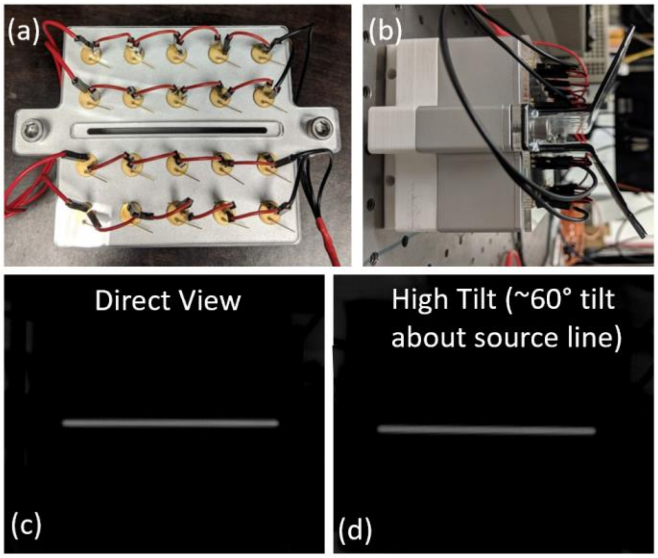

Figure 5. The assembled LITMIC source was constructed from an aluminum cavity and utilized 20 ‘cap’ input sources (a). Aluminum gull fins were added to the top of the box during testing to shield the back end of the caps and to assure no excess emission or reflected LWIR came from the LITMIC source (b). A direct view of the source, as capture by a LWIR camera, shows high spatial uniformity of the signal and an ideal rectangular emission shape (c), and when the LITMIC source is rotated about the emission slit, the same uniformity and power output is observed (d) indicating idea uniform non-direction emission from the exit slit.

3.2 Optics Under Test

Two diffuse optics were measured with both the tungsten ribbon and the LITMIC sources. The first optic was a 1500 grit ground glass (BK7) diffusing flat, measuring 2 inches in diameter, referred to as Glass^{1500}. Second, a bare aluminum blank, measuring 3 inches in diameter was tested in two separate configurations. The Al flat was tested at room temperature, referred to as Al_{Room}, and additionally, the optic was tested under thermal load, after being heated to a temperature of 150 °C, referred to as $\text{Al}_{150,}$ to model metrology of an object operating in a high temperature environment. The heating was accomplished by placing the aluminum blank on a hot plate operating at 150 °C for 30 minutes, after which, it was removed from the hot plate and mounted for testing. Surface roughness of the two optics were verified with a Zygo NewView 8300 Interference Microscope. The surface roughness of the Glass_{1500} was measured as 127.89 nm RMS while the Al_{Room} was measured as 102.53 nm. UUTs were positioned 1.35 m from the source plane. Figure 6 demonstrates the optics that were measured.

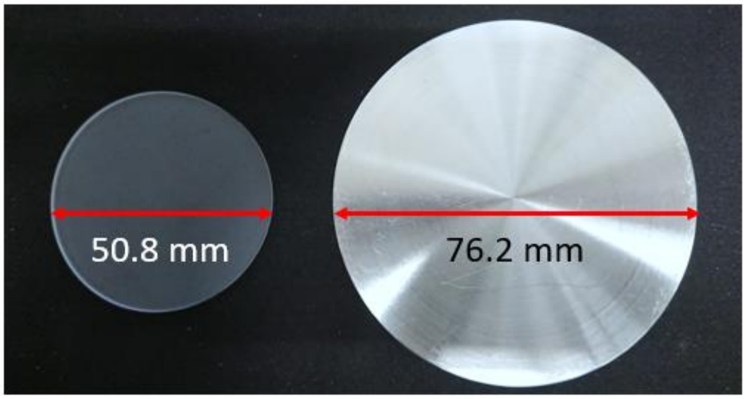

Figure 6. A 2-inch diameter rough ground glass flat, referred to as Glass^{1500}, (left) and bare aluminum flat, referred to as Al_{Room}, (right) were selected for measurement due to their diffuse nature, making infrared deflectometry and ideal metrology method. The surface roughness of both optics was measured using a Zygo NewView 8300 Interference Microscope. The ground glass surface featured a surface roughness of 127.89 nm RMS while the bare aluminum surface roughness was 102.53 nm RMS.

3.3 Source Geometry and Temporal Stability Measurements

To measure the source emission geometry, tests were performed by recording a focused image of each source using the LWIR camera previously described. A profile across the middle of each source was recorded to determine how similar each true source profile was, as compared to the assumed ideal flat top rectangular emission profile. Consequently, this allowed for verification that the recorded signal power on the camera pixels was similar between the two sources, and that the source area was similar on the detector for both sources.

To observe the temporal stability, a measurement was performed by focusing the camera on each source, which was turned on and recorded for 30 minutes, separately. An image was recorded every 10 seconds. For the test of both the tungsten ribbon source as well as the LITMIC source, signal data was calculated over a series of pixels that were imaging the source (N=50), and the noise statistics were calculated over several random pixels imaging the background scene ($N = 50$). Over every signal pixel the average recorded signal count, the standard deviation of the signal, and the peak-to-valley (PV) variation of the signal count, as reported by the output from the detector, was calculated. The mean value for the signal power, referred to as $\text{signal}_{\text{time-mean}}$, the mean standard deviation, referred to as $\text{signal}_{\text{time-std}}$, and the mean PV variation, referred to as $\text{signal}_{\text{time-PV}}$, were calculated. Similarly, the average noise recorded signal over every noise pixel, as well as the standard deviation for every noise pixel was determined. The mean noise signal, referred to as $\text{noise}_{\text{time-mean}}$, as well as the noise standard deviation, referred to as $\text{noise}_{\text{time-td}}$, was also calculated.

3.4 Infrared Deflectometry Reconstruction and Repeatability

To determine the comparative surface reconstruction repeatability, multiple optics were measured using both sources. The Glass^{1500} and Al_{Room} and Al_{150} optics were measured using the previously described deflectometry system and the surfaces were reconstructed. For both sources, where the source was scanned 150 mm, using 30 interval steps, in a step and stare method. The step and stare method operators such that the source is ‘stepped’ to the next scan position. Once it has reached the new position and motion is stopped, an image capture is performed, referred to as the ‘stare’ process. UUT re-mounting and alignment error was avoided by testing surfaces with one source first and then the other, keeping all other system parameters identical between tests. For all surfaces, 5 measurements were performed in succession at each step and the behavior of several locations across the UUT were analyzed for each source. The centroids were calculated for each source configuration. For the ribbon source, an average of 5 background images were recorded and subtracted from all measurement images. For the LITMIC source, an ‘on’ (cavity emitting light) and ‘off’ (cavity not emitting light) signal was recorded at every step position, and the ‘off’ signal at each position was subtracted from the ‘on’ measurement. After this, a standard centroiding process was used for both source measurements. The total acquisition time for the full 5 successive measurements of each optic was approximately 18 minutes using the tungsten ribbon source and was approximately 20 minutes using the LITMIC source.

The repeatability of the source reconstruction was determined by calculating the statistics across the repeated measurements. Across several repeat measurements (N =5) the recorded peak signal response as well as the standard deviation between measurements of the peak signal response, referred to as $\text{signal}_{\text{mean}}$ and $\text{signal}_{\text{std}}$ respectively, were determined for the camera pixels imaging the UUT. Additionally, the mean peak signal response and standard deviation across the repeat measurements, referred to as $\text{noise}_{\text{mean}}$ and $\text{noise}_{\text{std}}$ respectively, were determined for the camera pixels imaging the background, which represents the noise statistics. The mean signal-to-noise ratio was then determined. Finally, the data for every measurement set was processed and the source coordinate that illuminated every camera pixel imaging the UUT was determined via a standard centroiding process. The mean centroiding uncertainty of the source across the 5 repeated measurements, referred to as δ_{mean}.

Taking the processed data, the surface of all optics was reconstructed for every measurement for both sources. Standard Zernike terms were fit to the reconstructed maps, and, after removing terms 1:4, 1:6, and 1:37, the maps were compared. The reconstruction repeatability was analyzed. The results of all tests are detailed in the following section.

1. Results

4.1 Source Geometry and Temporal Stability Measurements Results

The recorded source images the tungsten ribbon and LITMIC source, captured with the test system LWIR focused through a flat precision mirror onto the source planes, as well as the signal profile across the midline, are shown in figure 7.

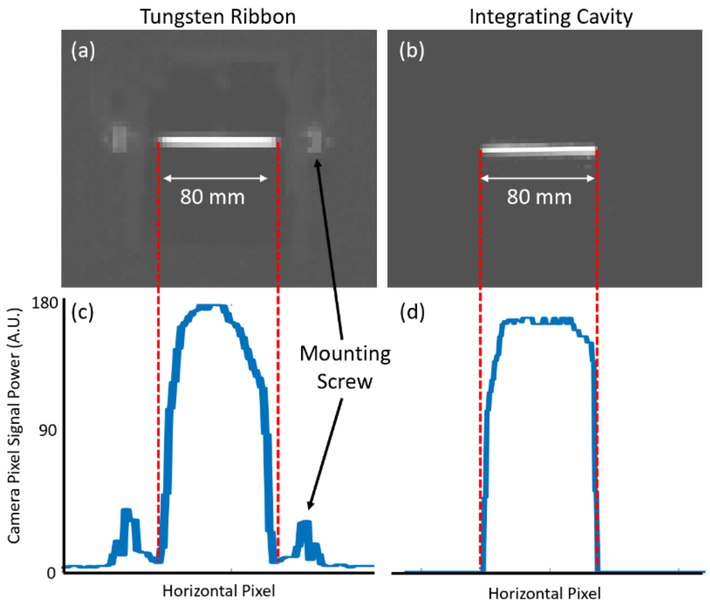

Figure 7. The source geometry is a key parameter in a deflectometry system. For the designed infrared deflectometry test system, and image of the tungsten ribbon (a) as well as the integrating cavity (b) sources was captured using the system camera through focused onto the source through a flat mirror. Observing a profile of the source for the tungsten ribbon (c) and the LITMIC (d) sources, it is seen that the average signal power is similar, but the source profile geometries are quite different, where both should ideally form a flat top rectangular shape.

The average source signal for both the LITMIC and tungsten ribbon sources, calculated over several pixels (*N*=50) imaging the source, over a 30-minute period with an image capture every 10 seconds is shown in figure 8.

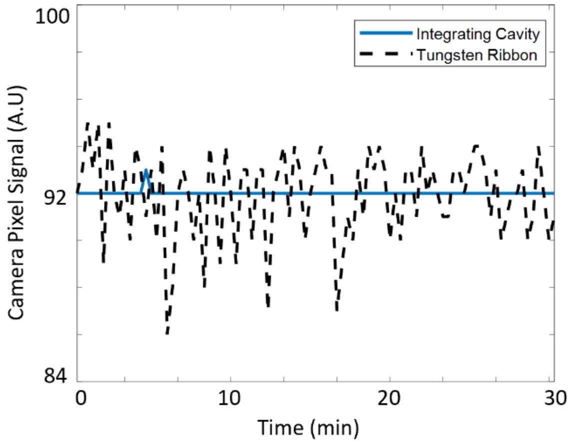

Figure 8. High temporal stability is essential for a deflectometry source, as any fluctuations in the radiant flux directly impacts the recorded power by the camera pixels, which leads to reconstruction error. Over a 30-minute period, with samples taken every 10 seconds, the camera detector pixel signal of the tungsten ribbon source (dotted black line) and the integrating cavity source (solid blue line) were recorded, to determine temporal stability of both sources.

The results of the source temporal stability measurements are reported in table 2. The time averaged camera signal of both sources, referred to as $\text{signal}_{\text{time-mean}}$, was calculated to verify the signal power, as recorded by the camera, was similar for both sources. Further, the standard deviation of the source signal over time, referred to as $\text{signal}_{\text{time-std}}$, is also reported, as is the peak-to-valley signal variation over the 30-minute measurement period, referred to as $\text{signal}_{\text{time-PV}}$. The time averaged background noise signal and the standard deviation of the noise signal over the 30-minute measurement period is also reported for both sources, referred to as $\text{noise}_{\text{time-mean}}$ and $\text{noise}_{\text{time-std}}$ respectively.

Table 2. Temporal Stability of Tungsten Ribbon and Integrating Cavity Sources

Source	signal$_{\text{time-mean}}$ (A.U.)	signal$_{\text{time-std}}$ (A.U.)	noise$_{\text{time-mean}}$ (A.U.)	noise$_{\text{time-std}}$ (A.U.)	signal$_{\text{time-PV}}$ (A.U.)
Tungsten Ribbon	95.72	1.97	72.39	0.45	11.10
LITMIC	93.21	0.53	73.32	0.43	1.82

The source image showed similar camera signal readout for both sources, which implies the source radiance for both the LITMIC and tungsten ribbon sources was similar, as designed. However, observing the profile of the sources, the tungsten ribbon source has a peak signal in the middle of the ribbon, which decays towards the edges, while the LITMIC source has a more rectangular emission pattern. The tungsten ribbon deviation from the ideal rectangular pattern is expected as the boundary conditions and material wear will cause the emission pattern to change from ideal. It must be noted that some of the shape deviation from an ideal rectangular shape is due to the limited camera resolution in the test setup, however.

The temporal stability results suggest again that while the average peak signals from both sources are similar, the temporal stability over time is highly different. At a peak mean power of ~95 signal counts on the camera, the tungsten ribbon fluctuated rapidly and randomly ~ 2 camera signal counts, or 2% of the signal power. Further, the peak-to-valley fluctuation at times reached 11 signal counts. The LITMIC source had a mean peak power of ~93 signal counts, fluctuating with a standard deviation of ~0.50 signal counts, or 0.5% of the signal power. The peak-to-valley fluctuation was 1.82 counts. In both test cases, the background noise, which is a combination of background radiation and camera noise, fluctuated with a standard deviation of ~0.4 signal counts on the camera.

4.2 UUT Reconstruction and Source Repeatability Results

The reconstructed surface roughness maps of the 2-inch diameter 1500 grit ground glass surface, referred to as Glass^{1500}, as well as the 3-inch diameter aluminum blank tested at room temperature and under a thermal load after being raised to a temperature of 150 °C, referred to as Al$_{\text{Room}}$ and Al$_{150}$ respectively are shown in figure 9. All surfaces were measured using the same deflectometry system with both the traditional tungsten ribbon source and the LITMIC source. The surface roughness was determined by removing Standard Zernike terms 1:37 from all surface maps to observe the high spatial frequency terms.

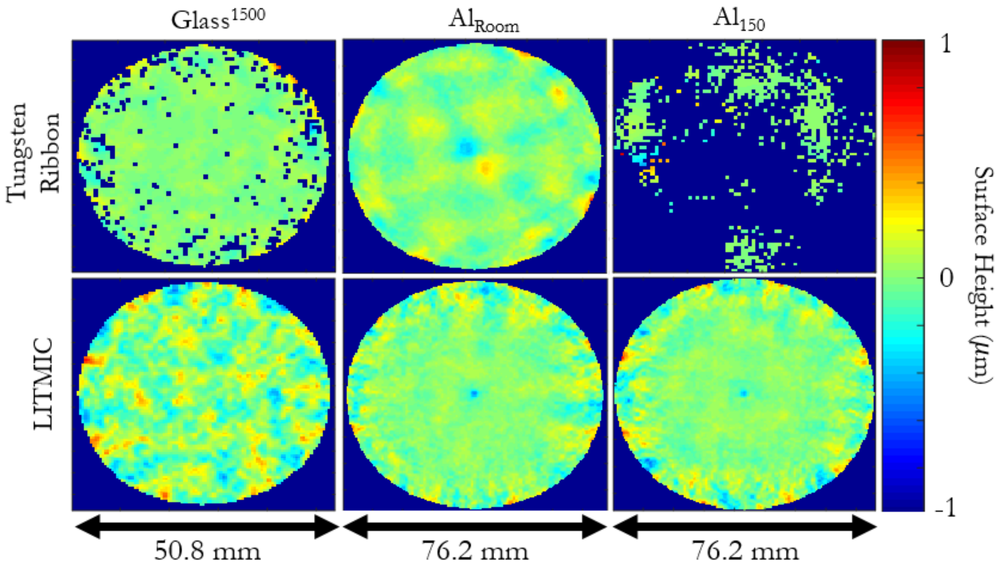

Figure 9. Using both a traditional tungsten ribbon source (top row) and the LITMIC source (bottom row), infrared deflectometry measurements were taken and the surface reconstructed for the Glass^{1500} optic (left column), the Al$_{\text{Room}}$ optic (middle column), and the Al$_{150}$ optic (right column). For all maps, Standard Zernike terms 1:37 were removed to observe the surface roughness, as represented by the high spatial frequency terms.

The surface roughness of the Glass^{1500} reconstructed surface was 156.63 nm RMS when tested with the LITMIC source and was 132.33 nm RMS when using the traditional tungsten ribbon source. The surface roughness of the Al$_{\text{Room}}$ reconstructed surface was 93.78 nm RMS when measured using the LITMIC source and was 95.63 when measured using the tungsten ribbon. The surface reconstructed of the Al_{150} was not successful when using the tungsten ribbon, however, the surface roughness when measured with the LITMIC source was 106.65 nm RMS. Figure 10 demonstrates the surface roughness maps of the $Glass^{1500}$ and Al_{Room} optics, as measured using a white light interferometer.

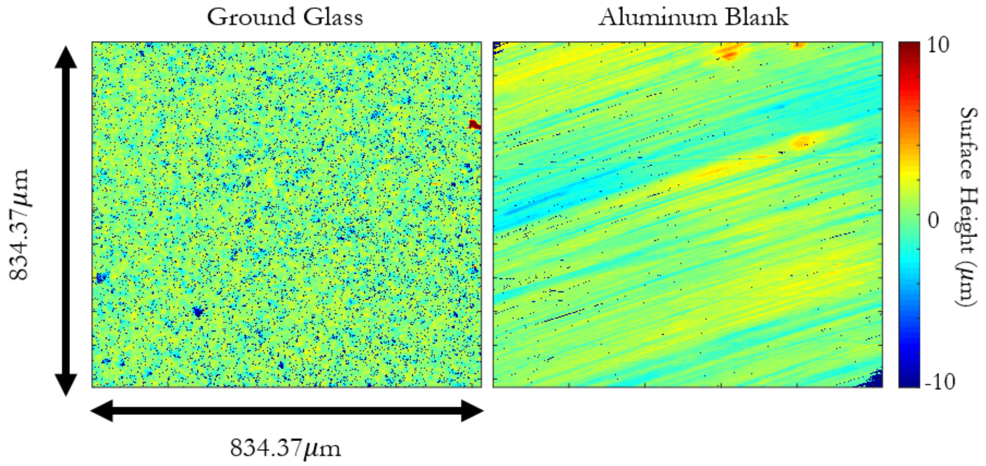

Figure 10. A 2-inch diameter rough ground glass flat, referred to as $Glass^{1500}$, (left) and bare aluminum flat, referred to as Al_{Room}, (right) surface roughness was measured using a Zygo NewView 8300 Interference Microscope. The ground glass surface featured a surface roughness of 127.89 nm RMS while the bare aluminum surface roughness was 102.53 nm RMS over a small 834×834 μm square area over each optic.

The signal from one pixel measuring the Al_{Room} surface during the five repeat measurements using the LITMIC source, as well as the average signal response is shown in figure 11. The mean peak signal response and the standard deviation of the peak signal response, as well as the mean peak background noise and standard deviation of the noise across the five measurements is also shown.

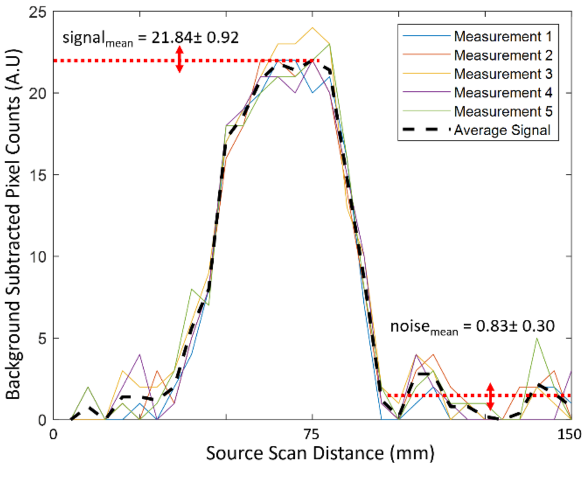

Figure 11. Five repeat measurements were obtained for every source configuration testing every optic. The five repeat camera signals for one pixel imaging the Aluminum blank at room temperature during testing using the LITMIC source were plotted, along with the average signal across the five measurements. For this test the mean peak signal recorded was 21.84, with a standard deviation of 0.92, while the mean peak background noise signal was 0.83, with a standard deviation of 0.30.

The signal, noise, and centroiding repeatability results across the five repeat deflectometry measurements of all optics, using both the LITMIC and tungsten ribbon sources, are reported in table 3. Please note that due to the lack of signal and the large noise in the measurement of the Al_{150} surface with a tungsten ribbon, it was impossible to record a consistent signal over anything more than a small portion of the UUT surface. Thus, these results were omitted as the signal, noise, SNR, and centroiding error could not be calculated.

Table 3. Source signal and reconstruction statistics

Source	Optic	$\text{signal}_{\text{mean}} \pm \text{signal}_{\text{std}}$ (A.U.)	$\text{noise}_{\text{mean}} \pm \text{noise}_{\text{std}}$ (A.U.)	SNR	Centroiding Error (mm)
Tungsten Ribbon	Glass^{1500}	4.68±1.92	1.28 ±0.44	3.66	6.30
LITMIC	Glass^{1500}	5.32±0.94	0.70±0.26	7.60	1.50
Tungsten Ribbon	Al_{Room}	22.68±1.17	4.74±0.27	4.78	4.50
LITMIC	Al_{Room}	21.84±0.92	0.85±0.30	25.69	1.35
LITMIC	Al_{150}	18.44±0.81	0.89±0.27	20.71	1.36

Both the LITMIC source and tungsten ribbon source were successfully used to test the Glass^{1500} and Al_{Room} optics. In both test cases, the mean signal power recorded after reflection from the optic was similar. The standard deviation across the five repeat measurements performed for every optic using each source however was slightly larger for the tungsten ribbon as compared to the LITMIC source. The LITMIC source was better able to reduce noise, with an average background noise of 0.70 camera signal counts in the glass test case, as compared to 1.28 counts for the tungsten ribbon, and approximately 0.85 counts for the tests of the aluminum blank, as compared to 4.74 counts for the tungsten ribbon. This directly impacts the SNR of both test methods, with the LITMIC source achieve a 2-5 times larger SNR. The centroiding repeatability over the five tests, determined by calculating the standard deviation of the centroids, was consistently ~1.5 mm for the LITMIC source and was 4-6 mm for the tungsten ribbon source.

Please note, the surface reconstruction results are in no way meant to reflect the reconstruction accuracy of either source, as the reconstruction accuracy related to several system level effects. They purely are meant to observe the repeatability and noise statistics of the traditional tungsten ribbon source and the LITMIC source.

2. Conclusion

While infrared deflectometry has been used to provide metrology of rough surfaces, there are clear limitations in surface testing and reconstruction capabilities due to inherent characteristics of a tungsten ribbon source. For precision fabrication and metrology, any uncertainty in the spatial and temporal behavior of a source directly negatively impacts the reconstruction accuracy and uncertainty. Additionally, due to testing being performed in the infrared region, there is almost always significant background thermal radiation contributions, which may fluctuate over time and further degrade results. We have instead created an integrating cavity source, which emits long wave infrared light uniformly from a machine precision exit slit, which we call the LITMIC source. The temporal and spatial emission behavior is excellent for the source. Further, the source is temporally modulated at up to 1 Hz, which allows not only for better signal isolation from the background noise but can accommodate testing in an environment where background thermal fluctuations are occurring.

A demonstration infrared deflectometry system using the new LITMIC source successfully tested a diffuse ground glass optic as well as an aluminum blank. The source exhibited excellent repeatability and significantly improved the SNR of the test, as compared to testing using a traditional tungsten ribbon. Further, the LITMIC source allowed for testing a previously unmeasurable aluminum blank while under thermal load, with the blank having been heated to approximately 150 °C. This could enable in-situ testing of optics placed under thermal load to observe surface behavior in extreme environment situations. We do not claim suing the LITMIC method is a superior test method to other metrology solutions. Instead, our goal is to expand the library of usable infrared sources for deflectometry, thereby further expanding the metrology options.

Acknowledgment.

This research was made possible in part by the II-VI Foundation Block-Gift Program, the Technology Research Initiative Fund Optics/Imaging Program, and the Friends of Tucson Optics Endowed Scholarships in Optical Sciences.

References

1. D. W. Kim, H. M. Martin, and J. H. Burge, "Calibration and optimization of computer-controlled optical surfacing for large optics," in Optical Manufacturing and Testing IX (International Society for Optics and Photonics, 2011), Vol. 8126, p. 812615.
2. M. Beier, S. Scheiding, A. Gebhardt, R. Loose, S. Risse, R. Eberhardt, and A. Tünnermann, "Fabrication of high precision metallic freeform mirrors with magnetorheological finishing (MRF)," in Optifab 2013 (International Society for Optics and Photonics, 2013), Vol. 8884, p. 88840S.
3. T. Blalock, K. Medicus, and J. D. Nelson, "Fabrication of freeform optics," in Optical Manufacturing and Testing XI (International Society for Optics and Photonics, 2015), Vol. 9575, p. 95750H.
4. D. W. Kim, C. Oh, A. Lowman, G. A. Smith, M. Aftab, and J. H. Burge, "Manufacturing of super-polished large aspheric/freeform optics," in (2016), Vol. 9912, pp. 99120F-99120F–9.
5. D. W. Kim, J. H. Burge, J. M. Davis, H. M. Martin, M. T. Tuell, L. R. Graves, and S. C. West, "New and improved technology for manufacture of GMT primary mirror segments," in Advances in Optical and Mechanical Technologies for Telescopes and Instrumentation II (International Society for Optics and Photonics, 2016), Vol. 9912, p. 99120P.
6. P. Zhou, H. Martin, C. Zhao, and J. H. Burge, "Mapping Distortion Correction for GMT Interferometric Test," in Imaging and Applied Optics Technical Papers (2012), Paper OW3D.2 (Optical Society of America, 2012), p. OW3D.2.
7. C. J. Oh, A. E. Lowman, G. A. Smith, P. Su, R. Huang, T. Su, D. Kim, C. Zhao, P. Zhou, and J. H. Burge, "Fabrication and testing of 4.2m off-axis aspheric primary mirror of Daniel K. Inouye Solar Telescope," in Advances in Optical and Mechanical Technologies for Telescopes and Instrumentation II (International Society for Optics and Photonics, 2016), Vol. 9912, p. 99120O.
8. M. B. Dubin, P. Su, and J. H. Burge, "Fizeau interferometer with spherical reference and CGH correction for measuring large convex aspheres," in (2009), Vol. 7426, pp. 74260S-74260S–10.
9. R. Geyl, D. Bardon, R. Bourgois, N. Ferachoglou, E. Harel, and C. Couteret, "First steps in ELT optics polishing," in Fifth European Seminar on Precision Optics Manufacturing (International Society for Optics and Photonics, 2018), Vol. 10829, p. 1082904.
10. M. Dimmler, P. Barriga, M. Cayrel, F. Derie, A. Foerster, F. Gonte, J. C. Gonzalez, L. Jochum, N. Kornweibel, S. Leveque, C. Lucuix, and L. Pettazzi, "Getting ready for serial production of the segmented 39-meter ELT primary: status, challenges and strategies," in Ground-Based and Airborne Telescopes VII (International Society for Optics and Photonics, 2018), Vol. 10700, p. 1070043.
11. U. Mueller, "Production metrology design and calibration for TMT primary mirror fabrication used at multiple manufacturing sites," in Ground-Based and Airborne Telescopes VI (International Society for Optics and Photonics, 2016), Vol. 9906, p. 99060Z.
12. M. Sieger, F. Balluff, X. Wang, S.-S. Kim, L. Leidner, G. Gauglitz, and B. Mizaikoff, "On-Chip Integrated Mid-Infrared GaAs/AlGaAs Mach–Zehnder Interferometer," Anal. Chem. 85, 3050–3052 (2013).
13. H. Yoo, G. A. Smith, C. J. Oh, A. E. Lowman, and M. Dubin, "Improvements in the scanning long-wave optical test system," in Optical Manufacturing and Testing XII (International Society for Optics and Photonics, 2018), Vol. 10742, p. 1074216.
14. T. Su, S. Wang, R. E. Parks, P. Su, and J. H. Burge, "Measuring rough optical surfaces using scanning long-wave optical test system. 1. Principle and implementation," Appl. Opt., AO 52, 7117–7126 (2013).

15. H. M. Martin, R. G. Allen, J. H. Burge, J. M. Davis, W. B. Davison, M. Johns, D. W. Kim, J. S. Kingsley, K. Law, R. D. Lutz, P. A. Strittmatter, P. Su, M. T. Tuell, S. C. West, and P. Zhou, "Production of primary mirror segments for the Giant Magellan Telescope," in Advances in Optical and Mechanical Technologies for Telescopes and Instrumentation (International Society for Optics and Photonics, 2014), Vol. 9151, p. 91510J.
16. L. R. Graves, H. Quach, H. Choi, and D. W. Kim, "Infinite deflectometry enabling 2pi-steradian measurement range," Opt. Express, OE 27, 7602–7615 (2019).
17. W. H. Southwell, "Wave-front estimation from wave-front slope measurements," J. Opt. Soc. Am., JOSA 70, 998–1006 (1980).
18. M. Aftab, J. H. Burge, G. A. Smith, L. Graves, C. Oh, and D. W. Kim, "Chebyshev gradient polynomials for high resolution surface and wavefront reconstruction," in Optical Manufacturing and Testing XII (International Society for Optics and Photonics, 2018), Vol. 10742, p. 1074211.
19. T. Su, "Asphercial Metrology for Non-Specular Surfaces with the Scanning Long-Wave Optical Test System," (2014).
20. D. W. Kim, T. Su, P. Su, C. Oh, L. Graves, and J. Burge, "Accurate and rapid IR metrology for the manufacture of freeform optics | SPIE Homepage: SPIE," http://www.spie.org/newsroom/6015-accurate-and-rapid-ir-metrology-for-the-manufacture-of-freeform-optics?SSO=1.
21. T. Su, S. Wang, R. E. Parks, P. Su, and J. H. Burge, "Measuring rough optical surfaces using scanning long-wave optical test system. 1. Principle and implementation," Appl. Opt., AO 52, 7117–7126 (2013).
22. S. Höfer, J. Burke, and M. Heizmann, "Infrared deflectometry for the inspection of diffusely specular surfaces," Advanced Optical Technologies 5, 377–387 (2016).
23. T. Su, W. H. Park, R. E. Parks, P. Su, and J. H. Burge, "Scanning Long-wave Optical Test System: a new ground optical surface slope test system," in Optical Manufacturing and Testing IX (International Society for Optics and Photonics, 2011), Vol. 8126, p. 81260E.
24. P. R. Bevington and D. K. Robinson, Data Reduction and Error Analysis for the Physical Sciences (McGraw-Hill, 2003).
25. J. S. Morgan, D. C. Slater, J. G. Timothy, and E. B. Jenkins, "Centroid position measurements and subpixel sensitivity variations with the MAMA detector," Appl. Opt., AO 28, 1178–1192 (1989).
26. J. C. De Vos, "A new determination of the emissivity of tungsten ribbon," Physica 20, 690–714 (1954).
27. V. D. Dmitriev and G. K. Kholopov, "Radiant emissivity of tungsten in the infrared region of the spectrum," J Appl Spectrosc 2, 315–320 (1965).
28. K. Ujihara, "Reflectivity of Metals at High Temperatures," Journal of Applied Physics 43, 2376–2383 (1972).

APPENDIX D

Model-free Optical Surface Reconstruction from Deflectometry Data

Logan Rodriguez Graves, Heejoo Choi,
Wenchuan Zhao, Chang Jin Oh, Peng Su,
and Dae Wook Kim

Copyright Transfer Agreement

Model-free optical surface reconstruction from deflectometry data

L. R. Graves[a], H. Choi[a], W. Zhao[b], C. J. Oh[a], P. Su[c], T. Su[d], D. W. Kim[a,e*]

[a]College of Optical Sciences, Univ. of Arizona, 1630 E. University Blvd., Tucson, AZ USA 85721
[b]The Institute of Optics and Electronics, Chinese Academy of Sciences, Chengdu 610209, China
[c]ASML Corporation, 77 Danbury Road, Wilton, TC 06897 USA
[d]KLA-Tencor Corporation, 3 Technology Dr., Miltipas, CA 95035, USA
[e]Steward Observatory, University of Arizona, 933 N. Cherry Ave., Tucson, AZ 85719, USA

ABSTRACT

Deflectometry is a metrology method able to measure large surface slope ranges that can achieve surface reconstruction accuracy similar to interferometry, making it ideal for freeform metrology. While it is a non-null method, deflectometry previously required a precise model of the unit under test to accurately reconstruct the surface. However, there are times when no such model exists, such as during the grinding phase of an optic. We developed a model-free iterative data processing technique which provides improved deflectometry surface reconstruction of optics when the correct surface model is unknown. The new method iteratively reconstructs the optical surface, leading to a reduction in error in the final reconstructed surface. Software simulations measuring the theoretical performance limitations of the model-free processing technique as well as a real-world test characterizing actual performance were performed. The method was implemented in a deflectometry system and a highly freeform surface was measured and reconstructed using both the iterative technique and a traditional non-iterative technique. The results were compared to a commercial interferometric measurement of the optic. The reconstructed surface departure from interferometric results was reduced from 44.39 µm RMS with traditional non-iterative deflectometry down to 5.20 µm RMS with the model-free technique reported.

Keywords: Deflectometry, model-free, metrology, freeform

INTRODUCTION

As the use of freeform optics in optical systems increases, there is a growing demand for accurate and dynamic metrology systems. Two popular optical tests methods that are used for freeform metrology are deflectometry and interferometry [1, 2]. Interferometry requires a null configuration for accurate results. This poses a challenge for freeform optics, as the null optics will typically have to be custom computer generated holograms (CGHs) [3]. While CGHs are extremely useful, they are expensive and only work for one null configuration. Deflectometry, a non-null test method, has been used to provide accurate metrology of standard to freeform optics [4–6]. A deflectometry test relies on having a source at a defined position. The ray emitted from the source is deflected by the unit under test (UUT) and is recorded by a detector. This allows for surface slope calculations of the UUT, and the process can be thought of as a reverse Hartmann test. By recording the ray start and end location, the slope on the UUT which deflected the ray is calculated. This slope calculation is typically done in a ray trace program, and the slope calculation relies on having an accurate estimation of where the ray was deflected by the UUT [5-6]. To minimize the error in the slope calculation an accurate model of the UUT is required for the ray trace process. However, it is not always possible to have an accurate surface model of the UUT; an example of this is during the grinding phase of an optic where the root mean square (RMS) surface shape error from an ideal surface can change by millimeters between runs. In lacking an accurate surface model of the UUT, significant error in the final reconstruction model can develop, particularly in the low to mid surface shapes [5]. There are limited methods for reconstructing deflectometry data when an accurate surface model is unknown, and all require significant user input. A standard approach when no accurate model exists is to simply model the UUT as a flat, recognizing that the final reconstruction map's low-mid order shape values have high uncertainty. More advanced approaches such as an iterative system parameter optimization process [7] and a rapid reconstruction method using a non-zonal parameter dependent integration to improve the initial UUT model followed by a successive over relaxation zonal integration [8, 9] can lead to improved reconstruction accuracy.

*letter2dwk@hotmail.com

Optical Manufacturing and Testing XII, edited by Ray Williamson, Dae Wook Kim,
Rolf Rascher, Proc. of SPIE Vol. 10742, 107420Y · © 2018 SPIE
CCC code: 0277-786X/18/$18 · doi: 10.1117/12.2320745

One primary limitation of these methods however is the demand for involved used input. We developed a model free iterative deflectometry (MID) reconstruction approach which avoids the need for any user input model [10]. The MID process begins always with a flat as the starting shape assumption and reconstructs the surface, which then serves as the surface model for the next iteration. This process is repeated until a final reconstructed surface is converged upon. By utilizing a continuously updating surface model, the MID method achieves improved accuracy in the low to mid spatial frequencies in the reconstruction map without any user input beyond the raw deflecomtetry data. In this paper we present a test of a freeform optic and the reconstruction results using the MID technique, which is described in detail in our previous publication [10]. A simulation is also presented which explores the influence the geometric position uncertainty in the system has on the final reconstruction map.

METHODOLOGIES

The raw input data for the MID approach does not differ significantly from traditional deflectometry processing methods. The Cartesian coordinates in object space (UUT) of the source and the camera, which are defined as matrices S and C respectively, must be known to high accuracy and must be input to the software. For the UUT itself, the MID approach always starts by defining the model as a flat, referred to as matrix U^0. The UUT clear aperture diameter must be input and, to bound piston of the model, one point on the UUT, $u^k(x,y,z)$, must be measured to determine its Cartesian coordinate in object space as well as what pixel on the camera is measuring it. The final input for the MID approach are the ray pointing vectors of the camera detector pixels, defined as vector R. Using these inputs, the MID process runs for a total of t = 0:N iterations and results in a final reconstruction surface U^N. The overall process is shown in figure 1.

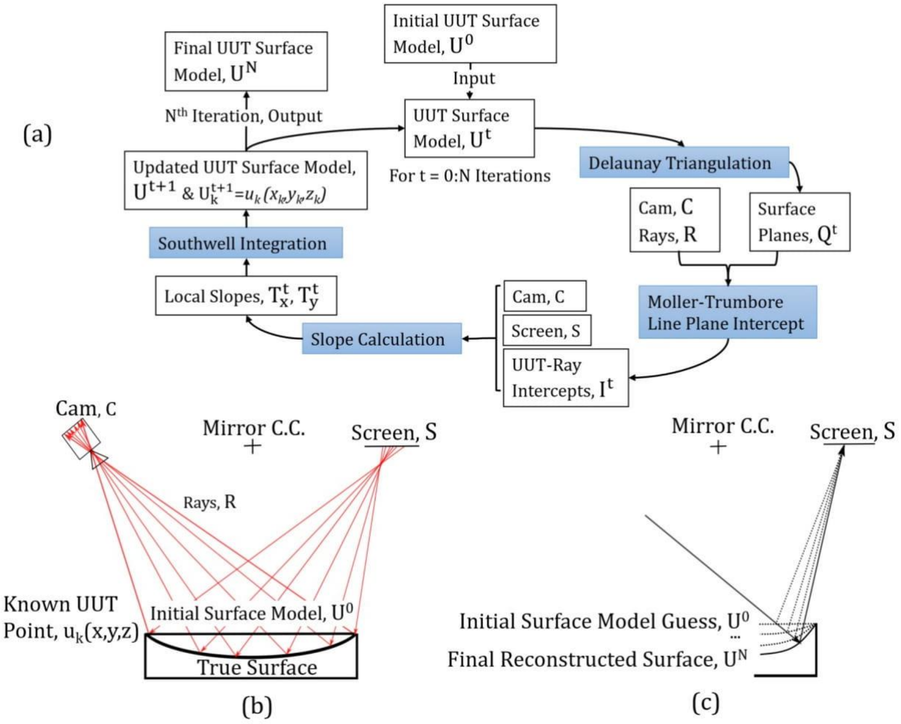

Figure 1. Using the initial flat surface model, U^0, the MID process iterates N times and generates the final surface reconstruction map U^N (a). With a traditional non-iterative approach when the UUT model is incorrect the ray intercepts are calculated at the plane of U^0 (b). Using the MID method, the true surface can be converged upon (c) [10].

During the MID process the UUT model is first segmented into surface planes, defined as matrix Q^t , using a Delaunay triangulation [11]. Rays are then traced from the detector and the intercept locations, defined as matrix I^t, calculated using a Möller–Trumbore algorithm [12]. The combined Delaunay/ Möller–Trumbore (DMT) process allows for highly accurate slope calculations at every iteration. The Delaunay process takes the discrete surface points, which are defined by mapping the camera pixels to the UUT surface model and segments them into unique planes that are well-shaped triangles and satisfy a nearest-neighbor relationship. Coupled with the Möller–Trumbore algorithm, which performs a highly efficient rapid ray-plane intercept calculation, the exact ray intercept coordinate in the surface planes is determined in 3D space. The combined DMT process linearly increases in total processing time while an improvement in accuracy exponentially decays with respect to the number of camera pixels used. The process is demonstrated in figure 2 [10].

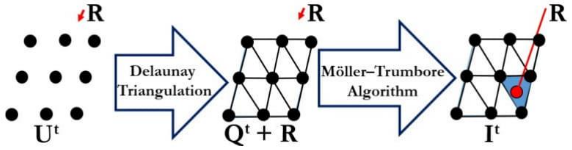

Figure 2. Surface points U^t are segmented into triangular planes, Q^t, using a Delaunay algorithm. The ray intercepts, I^t, are then calculated using a Möller–Trumbore algorithm.

The local slopes at the UUT model surface in the x and y directions, defined as matrices T_x^t and T_y^t respectively, are calculated using the ray start and end locations, C and S, and the intercept coordinates. The local slopes are then integrated using a standard Southwell integration [13] to reconstruct the surface model. The process is iterated, with a new reconstructed model U^t, being output at each iteration for a total of N iterations, at which point the final reconstructed model is output, referred to as model U^N.

In a previous paper, the performance of the MID approach was compared to a traditional non-iterative reconstruction method for deflectometry data [10]. The optic tested was a bare glass surface with freeform departure in all directions and had a radius of curvature (RoC) of 200 mm and a clear aperture diameter of 100 mm. The surface was generated using a magnetorheological finishing (MRF) method which imparted a spiral pattern unto the surface. As a reference comparison the UUT was measured using a commercial interferometer, a Zygo Verifire^{TM} MST. A Zygo F/1.75 sphere was used as the reference optic for the interferometer. The interferometer cannot accurately measure piston, tip, tilt, and power, and thus these terms were dismissed in all measurements, both interferometric and from the deflectometry test. Due to the steep freeform departure and the lack of a custom CGH for the test there was high fringe density even at best null configuration which resulted in partial surface reconstruction error and missing data in the final surface. Figure 3 shows the best null configuration obtained in the interferometric test and highlights the complex fringe pattern and the challenges associated with measuring the optic [10].

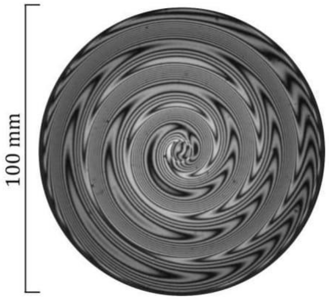

Figure 3. The UUT had a spiral pattern imparted on the surface which made obtaining an interferometric null impossible across the entire surface. High fringe density resulted in low modulation which made some areas on the map unmeasurable.

To obtain a deflecomtetry measurement of the UUT a SCOTS type system was utilized. The system consisted of an LCD monitor which acted as the phase shifting source and an off the shelf camera. The UUT was mounted onto a rotation stage below the screen and camera, which were located near the center of curvature of the UUT. All components were securely mounted on a breadboard which allowed for their positions to be maintained throughout testing. To measure the position of all components a coordinate measuring machine (CMM) was used with a touch tip probe, which provided position accuracy to ±10 µm. The body edges of the camera were measured, and the detector plane was located relative to the camera body using technical drawings. For the screen, the monitor edges were measured, and a plane was fit which defined the source. Finally, the center of rotation on the surface of the UUT was measured, which served as the known coordinate, u_k (x_k,y_k,z_k) and as the global zero coordinate in x, y, and z. This was related to the camera pixel measuring the known coordinate, pixel p(x,y,z). The full system parameters are listed below in table 1.

Table 1. Deflectometry Test System parameters

Camera Parameters	
Manufacturer	Point Grey
Model	FL3-U3-32S2M-CS
Resolution	2080x1552
Chroma	Mono
Pixel Pitch	2.5 µm
Source Parameters	
Manufacturer	Mimo Monitors
Model	Mimo UM-760F
Resolution	1024x600
Pixel Pitch	150 µm
Mirror Parameters	
Manufacturer	Optimax Systems, Inc
Method	MRF
Surface	Bare Glass
Diameter of Optic	100 mm
Radius of Curvature	200 mm

For system calibration and to determine the pointing vectors of the camera pixels the ray intercept locations of the camera pixels were measured at two locations. The camera was positioned at location c(x,y,z) and fixed in place. A screen was then placed facing the camera at location l_1(x,y,z). The screen pixels were then activated to determine which screen pixels were being measured by each camera pixel. The screen was then shifted axially along the camera pointing direction to a second location, l_2(x,y,z), and the process was repeated. By measuring the screen intercept coordinates of the camera pixels at two locations the pointing vectors for every camera pixel were recorded. All positions, c(x,y,z), l_1(x,y,z), and l_2(x,y,z), were measured using a CMM which was accurate to ± 10 µm. The test setup of the ray pointing vector calibration process is shown below in figure 4 [10].

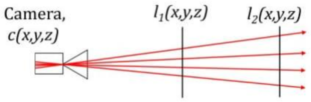

Figure 4. The ray path of all camera pixels was determined by measuring the ray intercept at two locations, l_1 and l_2.

To obtain the raw deflectometry data the screen displayed a total of eight fringes, four in the x and four in the y directions, while the camera measured the reflected signal from the UUT. To reduce systematic error, the UUT was clocked 36 times, with a 10° clocking each time for a full rotation and was measured at each position. This allowed for a rotation calibration to be performed [14]. After the raw data was obtained the surface was reconstructed in three ways. First, the MID method was performed, using a total of six iterations to reconstruct the surface. Second, a traditional non-iterative reconstruction method was performed using the same raw data, in which (1) a flat surface was assumed as the UUT model and (2) a 200 mm RoC base sphere model was assumed. For all the methods the phase maps were unwrapped using a four-bucket unwrapping algorithm to determine the screen coordinates, which were used for the local slope calculations. The local slopes were integrated using a Southwell integration to obtain a reconstructed surface. The clocked measurements were reconstructed and averaged to create systematic error maps which were removed from the reconstructed surfaces to generate the final reconstruction maps for the MID method and the two traditional techniques, referred to as MID_6, MB_{flat}, and MB_{sphere} respectively. These maps were analyzed, and low order standard Zernike terms were fit to the data to compare to the interferometric map, referred to as INT. The missing data regions in the INT map were not considered in the comparison to avoid extrapolation.

To complement the results of the paper a simulation of the test setup was performed, in which the system was modeled as measured and the screen and camera positions were modeled with ±10 µm uncertainty as well as a tip/tilt/rotation uncertainty of 1 mrad. The simulation was created to model the expected error effects in the final reconstruction surface due to the geometric uncertainty of the real test setup. Using the test setup uncertainty values described, the measurement was simulated, and the surface was reconstructed using the MID method for six iterations. The error between the reconstructed surface map and the ideal surface was calculated and low order standard Zernike terms Z5:Z11 were fit to the error maps. This allowed for an estimation of the amount of error that could reasonably be expected in the final reconstruction results for the real test based on the position uncertainties that existed in the test measurement.

RESULTS

The simulation was constructed in Matlab in which an ideal sphere modeled on the previously measured optic served as the UUT, with a radius of curvature of 200 mm and a diameter of 100 mm. The position of the screen and camera were modeled on the measured position of the test performed in the previous paper. Using the previously measured ray pointing vectors, a ray trace was performed which traced the rays from the camera pupil to the modeled UUT, and finally to the screen plane. Using this data, which represented the modeled raw output data we expect from a deflectometry test, the surface was reconstructed using the MID method. For no input error the MID method converged to a perfect reconstruction (limited by machine precision). The camera position was then modeled with a 10 µm error in the x, y, and z positions, as well as a tip, tilt, and rotation error of 1 mrad. Similarly, the screen was modeled with a 10 µm error in the x, y, and z positions and a tip, tilt, and rotation error of 1 mrad. These values represented the uncertainty in the position knowledge of the components in the previous paper [10]. The surface was then reconstructed using the MID approach and the difference in the reconstructed surface with geometric error induced versus the perfect reconstruction surface was determined. Standard Zernike terms 5:11 were fit to the difference map and a root-sum-square (RSS) was calculated for the error from the various configurations to determine the total error attributable to the geometric uncertainty. The results of the surface error in the reconstruction of the simulations are shown below in table 2 and table 3.

Table 2. Screen Uncertainty Simulation Reconstruction Error

Zernike Terms	10 µm X Pos. Error (µm)	10 µm Y Pos. Error (µm)	10 µm Z Pos. Error (µm)	1 mrad Tip Error (µm)	1 mrad Tilt Error (µm)	1 mrad Rotation Error (µm)	RSS Value (µm)
Z5	0.003	-1.497	-0.042	0.031	-0.002	-0.001	**1.50**
Z6	1.471	0.002	0.203	0.001	0.034	0.002	**1.49**
Z7	0.005	0.603	0.010	0.003	0.001	0.001	**0.60**
Z8	0.576	0.007	0.038	0.002	0.002	0.001	**0.58**
Z9	0.028	0.161	0.031	0.078	-0.015	-0.002	**0.18**
Z10	-0.580	0.161	-0.102	0.018	0.078	0.002	**0.62**
Z11	0.207	0.171	0.152	0.170	0.170	0.170	**0.38**

Table 3. Camera Uncertainty Simulation Reconstruction Error

Zernike Terms	10 µm X Pos. Error (µm)	10 µm Y Pos. Error (µm)	10 µm Z Pos. Error (µm)	1 mrad Tip Error (µm)	1 mrad Tilt Error (µm)	1 mrad Rotation Error (µm)	RSS Value (µm)
Z5	-0.006	4.119	-0.120	-0.001	-0.001	-0.001	**4.12**
Z6	-4.093	0.000	0.600	0.000	0.000	0.000	**4.14**
Z7	-0.008	-1.311	0.055	0.001	0.001	0.001	**1.31**
Z8	-1.253	-0.008	0.261	0.001	0.001	0.001	**1.28**
Z9	-0.203	-1.033	0.051	0.000	0.000	0.000	**1.05**
Z10	1.787	-0.313	-0.177	0.004	0.004	0.004	**1.82**
Z11	0.092	0.165	-0.479	0.170	0.170	0.170	**0.56**

The raw data from the deflectometry measurement of the UUT was reconstructed using the three methods, MID and the traditional non-iterative technique. The reconstructed surface maps were compared to the interferometric map and the difference between the surfaces was determined. The difference between the reconstruction maps had low order standard Zernike terms up to Z11 fit to the data. The first four Zernike terms, piston, tip, tilt, and power were not considered in the fit. The results are shown below in table 4.

Table 4. Low Order RMS Normalized Zernike Term Difference between Reconstructed and Interferometric Surface Maps

Zernike Term	MID$_6$ (µm)	MB$_{flat}$ (µm)	MB$_{sphere}$ (µm)
Z5, Oblique Astigmatism	0.76	1.90	0.42
Z6, Vertical Astigmatism	-5.12	-44.28	-15.80
Z7, Vertical Coma	-0.36	-1.98	-0.40
Z8, Horizontal Coma	-0.10	0.55	0.11
Z9, Vertical Trefoil	0.32	1.01	0.25
Z10, Oblique Trefoil	-0.05	0.29	0.06
Z11, Spherical	0.04	0.63	0.17
Z5:Z11 Total RMS Diff	5.20	44.39	15.80

For low order terms Z5-Z11, the total Zernike term root-mean-square (RMS) departure from the INT map for the MID$_6$, MB$_{flat}$, and MB$_{sphere}$ surfaces were 5.20 µm, 44.39 µm, and 15.80 µm, respectively. Based on the low order departure from INT, the MID method provides close to an order of magnitude improvement in reconstruction accuracy when compared to a traditional non-iterative approach with a flat as the model. When observing the reconstruction maps the astigmatism and coma mismatch between INT and the other reconstruction methods is apparent. The reconstruction maps with increasing Zernike terms removed are shown below in figure 5.

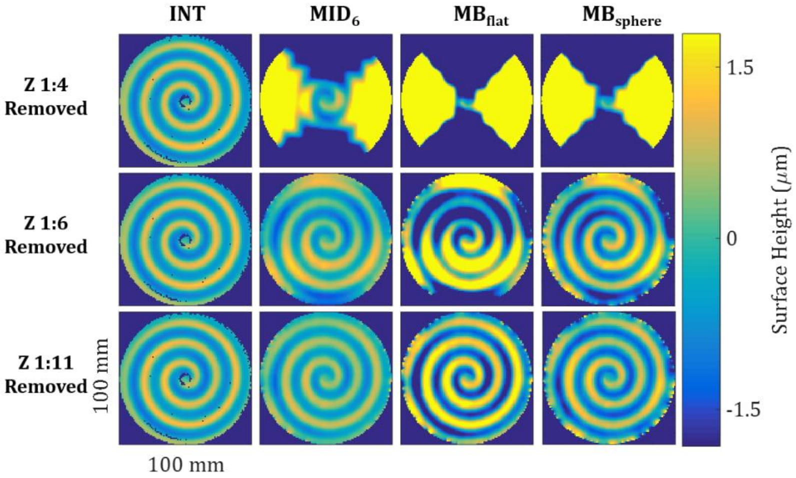

Figure 5. The interferometric surface map of the UUT (1st column), MID technique with 6 iterations (2nd column), and non-iterative traditional reconstruction with a flat UUT model (3rd column) and a 200 mm RoC base sphere model (4th column) method had Zernike terms 1-4 (top row), 1-6 (middle row), and 1-11(bottom row) removed to compare error contribution from low spatial frequency. Please note missing data regions in the interferometric surface map resulted from high fringe density in the measurement due to not having a custom CGH [10].

DISCUSSION

The MID approach produced a reconstruction map which more closely matched the interferometric measurement as compared to a traditional non-iterative reconstruction approach when no accurate model of the UUT exists. The improvement is particularly apparent at low order surface shapes, such as astigmatism and coma, where deflectometry traditionally suffers in reconstruction accuracy. However, there are still residual low order spatial features present in both MID and traditional non-iterative reconstruction approaches which were not present in the interferometric map. This is partly explained by the geometric uncertainties present in the deflectometry measurement. Any geometric error leads to significant reconstruction error in the final map. Most of the astigmatism and coma present in the final map from the MID method was predicted from the simulation of the test setup. This residual error can be reduced by using more advanced calibration methods to reduce geometric uncertainty.

Overall, the MID method was able to significantly reduce the low order terms as compared to the non-iterative approach, as well as demonstrating a capability to measure the large dynamic range of the UUT. This is particularly clear when considering the interferometric map of the UUT, which without a custom CGH struggled to achieve an ideal null, and thus resulted in missing data in the final map due to high fringe density.

CONCLUSION

The MID approach utilizes an iterative reconstruction method which leverages a Delaunay/ Möller–Trumbore algorithm to achieve improved reconstruction accuracy of raw deflectometry data. The approach can readily be applied to a deflectometry data processing package and can also be used on previously measured data. When testing a freeform bare glass UUT the MID method resulted in a final reconstructed surface map which more closely matched an interferometric measurement of the surface as compared to a traditional non-iterative deflectometry reconstruction approach of the same raw data. The improvement in accuracy is particularly apparent at low order spatial features, where traditional non-iterative deflectometry approaches struggled when no accurate UUT model was known. The residual errors in the final reconstruction approach were predicted by a simulation of the test which accounted for the geometric uncertainty of the positions of the hardware components. Thus, by improving calibration and hardware methods a further improvement in accuracy can be expected.

ACKNOWLEDGEMENT

This research was made possible in part by the II-VI Foundation Block-Gift Program, the Technology Research Initiative Fund Optics/Imaging Program, the Post-processing of Freeform Optics project supported by the Korea Basic Science Institute, the Friends of Tucson Optics (FoTO) Endowed Scholarships in Optical Sciences, and we thank Optimax Systems for providing the freeform UUT.

REFERENCES

[1] Martin, B., Burge, J., Miller, S., Warner, S., and Zhao, C., “Fabrication and Testing of 8.4 m Off-Axis Segments for the Giant Magellan Telescope” Frontiers in Optics 2008/Laser Science XXIV/Plasmonics and Metamaterials/Optical Fabrication and Testing, OSA Technical Digest (CD) (2008).

[2] Oh, C.J., Lowman, A., Smith, G., Su, P., Huang, R., Su, T., Kim, D.W., Zhao, W., Zhou. P., and Burge, J., “Fabrication and testing of 4.2m off-axis aspheric primary mirror of Daniel K. Inouye Solar Telescope,” Proc. SPIE 9912 (2016).

[3] Dubin, M.B., Su, P., and Burge, J., “Fizeau interferometer with spherical reference and CGH correction for measuring large convex aspheres,” Proc. SPIE 7426 (2009).

[4] Kim, D.W., Oh, C.J., Lowman, A., Smith, G., Aftab, M., and Burge, J., “Manufacturing of super-polished large aspheric/freeform optics,” Proc. SPIE 9912 (2016).

[5] Huang, R., “High Precision Optical Surface Metrology using Deflectometry,” Academic, (2015).

[6] Kim, D.W., Aftab, M., Choi, H.C., Graves, L., and Trumper, I., “Optical Metrology Systems Spanning the Full Spatial Frequency Spectrum,” presented at the Frontiers in Optics, p. FW5G.4. (2016).

[7] Olesch, E., Faber, C., and Häusler, G., “Deflectometric Self-calibration for arbitrary specular surfaces” in DGaO Proc. 112 Academic (2011).

APPENDIX E

Precision Optics Manufacturing and Control for Next-Generation Large Telescopes

Logan Rodriguez Graves, Greg A. Smith, Dániel Apai,
and Dae Wook Kim

Copyright Transfer Agreement

Nanomanufacturing and Metrology
https://doi.org/10.1007/s41871-019-00038-2

REVIEW PAPERS

Precision Optics Manufacturing and Control for Next-Generation Large Telescopes

Logan R. Graves[1] · **Greg A. Smith**[1] · **Dániel Apai**[2,3] · **Dae Wook Kim**[1,2]

Received: 2 December 2018 / Revised: 4 February 2019 / Accepted: 7 February 2019

Abstract

Next-generation astronomical telescopes will offer unprecedented observational and scientific capabilities to look deeper into the heavens, observe closer in time to the epoch of the Big Bang, and resolve finer details of phenomena throughout the universe. The science case for this next generation of observatories is clear, with science goals such as the discovery and exploration of extrasolar planets, exploration of dark matter and dark energy, the formation and evolution of planets, stars, galaxies, and detailed studies of the Sun. Enabling breakthrough astronomical goals requires novel and cutting-edge design choices at all stages of telescope manufacturing. In this paper, we discuss the integrated design and manufacturing of the next-generation large telescopes, from the optical design to enclosures required for optimal performance.

Keywords Metrology · Fabrication · Design · Telescope · Optics · Precision

1 Introduction

Astronomers studying new phenomena and testing increasingly detailed models of the universe require ever more powerful instruments to complete their goals and collect photons which have traversed immense distances and time, sometimes originating at the very beginning of the universe. From Edwin Hubble's measurements of the Doppler-shifts of galaxies, through studies of high redshift supernova explosions that revealed the acceleration of the universe to the latest studies of exoplanet atmospheric composition, astronomical knowledge has most often been limited by the number of photons that could be efficiently collected. Phenomena such as first light observations, exoplanet studies, dark matter, galaxy and planet formation, and other topics require ever more advanced scientific instruments. For a detailed analysis of these science goals, the reader is encouraged to explore resources such as the *GMT Science Book* [1] or *An Expanding View of the Universe—Science with the European Extremely Large Telescope* [2]. To provide these scientific capacities and to advance instrumentation capabilities, the next generation of telescopes (NGT) must provide higher spatial resolutions, larger light-collecting areas, and more sensitive instrumentation. These telescopes are each unique in their designs, from primary mirror and instrumentation design choices to the observatory sites and dome designs. However, they all share the goal of improving our understanding of the universe by providing advanced instruments for astronomical observations.

One family of fascinating telescope design concepts currently being implemented is that of extremely large telescopes. Since the 1.5 cm telescope made by Galileo in 1609, there has always been a push for larger light-collecting areas [3]. In the 19th century, there were rapid improvements in telescopes, beginning with the 60-inch (1.5 m) telescope in 1908, which was eclipsed by the Hooker telescope with a 2.5-m aperture in 1917. It was not until 1949 that the Hale Telescope took the record for the largest telescope aperture at 5.1-m, held until the BTA-6 telescope was introduced in 1975 with a 6-m aperture. Since then, the Keck 1 with a 10-m aperture in 1993, the LBT with two 8.4-m primary mirrors in 2005, and the Gran Telescopio Canarias with a 10.4-m aperture in 2009 have defined the largest telescopes in the world. Figure 1 demonstrates this evolution of telescope mirror diameters over time.

✉ Dae Wook Kim
letter2dwk@hotmail.com

[1] College of Optical Sciences, University of Arizona, 1630 E. University Blvd., Tucson, AZ 85721, USA

[2] Steward Observatory, University of Arizona, 933 N. Cherry Ave., Tucson, AZ 85718, USA

[3] Lunar and Planetary Laboratory, University of Arizona, 1629 E. Univ. Blvd., Tucson, AZ 85718, USA

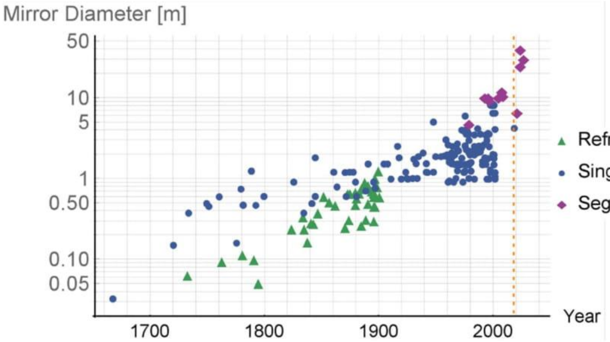

Fig. 1 Primary mirror diameter has grown more than two orders of magnitude in the last three centuries and shows no sign of slowing down. The next generation of extremely large telescopes will use segmented reflectors to increase mirror size by a factor of 3 or more within the next decade

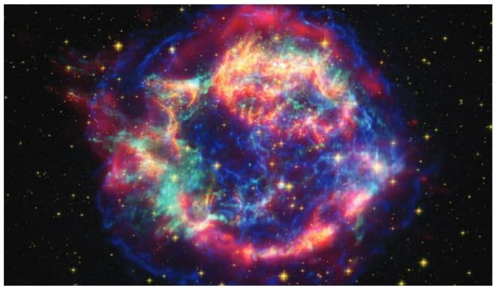

Fig. 2 One primary focus of the next generation of telescopes will be improved observational abilities of extremely faint phenomenon, such as the studies of supernova remnants, in conjunction with other telescopes. This is illustrated by the false color image of the remnants of supernova Cassiopeia A. This image uses data from the Spitzer Space Telescope (red), optical data from the Hubble Space Telescope (orange), and X-ray data from the Chandra X-ray Observatory (green) to display detailed structure. We can expect improved data from the next generation of telescopes to be used to provide a deeper look into such phenomenon [8]

Spanning more than two orders of magnitude in the last three centuries, the need for larger apertures shows no signs of slowing down. The extremely large telescopes, whose primary apertures will range from 20 to 40 m, are scheduled for first light as soon as 2024. Currently, three such telescopes are being fabricated and will be operational in the near future: the Giant Magellan Telescope (GMT) [4], the European Extremely Large Telescope (E-ELT) [5], and the Thirty Meter Telescope (TMT) [6, 7]. Despite sharing the designation of being extremely large telescopes, each system has unique design choices, from mirror substrate materials to adaptive optics approaches. However, all three extremely large telescopes share the feature of having enormous primary mirror collecting areas. This will enable not only greater light-collecting capability, allowing astronomers to observe fainter phenomenon in the universe, such as that shown in Fig. 2, but will also provide greater resolving power (spatial resolution) and higher image quality. A combination of spatial resolution, high image contrast, and sensitivity will be key, for example, to the imaging search for Earth-sized extrasolar planets in the solar neighborhood.

The current consensus is that a segmented primary mirror design is the best approach to create the light-collecting areas beyond that of 8.5-m diameter mirrors. The GMT consists of seven such circular aperture segments, each of which is an 8.4-m diameter monolithic borosilicate honeycomb structure [4]. The E-ELT and TMT primary mirrors are constructed of significantly more numerous, but smaller and thinner segments [5, 6]. Different designs have led to different fabrication approaches. GMT requires precise manufacturing over large areas. Each segment will be fabricated to have a root-mean-square (RMS) surface figure error in the 20 nm range after mirror bending modes are corrected. Six of the segments are off-axis parabolic structures and the central segment is an on-axis mirror with a central aperture. In contrast, the E-ELT and TMT have relatively more rapid fabrication processes per mirror segment. To maximize effective optical aperture size covered by mirrors in the final assembly, the segments will be hexagonal in shape. This requires unique fabrication methodologies, such as using Computer Numeric Control (CNC) machining, to achieve the desired mirror shape. For example, the E-ELT will utilize 798 hexagonal segments that are each roughly 1.45 m point to point and have unique freeform shapes [9]. While the fabrication processes for these extremely large primary mirrors is automated as much as practical, maintaining surface accuracy is a non-trivial process.

These extremely large ground-based telescopes will not operate in isolation. Their scientific observations will guide other ground-based observatories as well as observational programs on space-based telescopes [10]. The James Webb Space Telescope (JWST), scheduled for launch in 2021, uses a novel design in which 18 hexagonal, gold-coated beryllium segments make up the primary mirror. Surface RMS error is ~ 23 nm over a total diameter of 6.5 m, providing a significantly larger collecting area than the Hubble Space Telescope (HST) with its 2.4-m diameter design [11]. Unlike the HST, which observes at wavelengths ranging from near-ultraviolet to the near-infrared (0.2–2.3 µm), the JWST will be observing significantly deeper in the infrared wavelength range (0.6–27 µm). The JWST will be deployed to the L_2 Lagrange point between the Earth and Sun, and a large foldable sun shield made of aluminum and silicon-coated Kapton will improve telescope performance by keeping the telescope itself extremely cold throughout its mission.

Complementing these telescopes designed to probe deeper into the universe is the Large Synoptic Survey Telescope (LSST), whose goal is to provide time-domain observations by surveying extremely large swaths of the night sky. The system utilizes a single 8.4-m primary, similar to the GMT segments, and will have a final *f*-number of *f*/1.23 with a field of view (FOV) of 9.6 square degrees [12]. The LSST also utilizes a novel CCD camera system to accommodate the large FOV and sensitivity requirements, which is coupled with large bandpass filters having high optical requirements [13]. Part of the unique optical design of the LSST is a combined primary/tertiary mirror, requiring meticulous fabrication and metrology [14], as well as a custom telescope mount assembly [15]. Figure 3 demonstrates a portion of the process for fabricating both mirrors from a single glass blank.

The LSST is designed primarily for visible wavelengths, imaging from 320 to 1050 nm, and will spend approximately 90% of its observing time devoted to a deep-wide-fast survey mode. The data obtained is expected to include a catalog of 20 billion galaxies and a similar number of stars. This library will improve our scientific understanding of the universe and will provide valuable survey data for the global array of astronomical telescopes to examine in depth.

Another key area of observation which will soon benefit from next-generation telescopes is solar observations. The Daniel K. Inouye Solar Telescope (DKIST) is a 4.2-m aperture solar telescope which is expected to begin operations in 2019. The primary mirror is a 4.2-m off-axis parabolic surface fabricated from a monolithic piece of Zerodur glass with a super-smooth surface finish [16]. The system will provide spectro-polarimetry from the visible to near-infrared bands as well as advanced imaging tools to investigate solar flares, make coronagraphic observations of the prominence-cavity structure, and measure coronal magnetic fields among other studies.

Enabling these ambitious scientific programs requires advances in other supporting technologies as well. For the ground-based extremely large telescopes, advanced adaptive and active optical control are essential to achieve the system requirements. The GMT will utilize a segmented secondary mirror which provides active and adaptive control via driving actuators mounted onto a Zerodur support structure [17]. These systems, combined with active control of the primary segments, provide multiple different seeing modes for the telescope. On the other hand, the E-ELT system does not introduce a deformable mirror until after the first three mirrors in the optical path [9]. The fourth and fifth mirrors in the system provide adaptive optics control of the post-focus beam. All these design choices have tradeoffs and highlight

Fig. 3 The LSST primary/tertiary mirror is a coupled optic with an outer diameter of 8.4 m. This coupled design allows for a compact optical layout and powers the extremely wide FOV of the LSST. A 1.2-m stressed lap was used on the tertiary mirror while a 25-cm orbital lap was used on the primary mirror simultaneously using zirconium oxide as a polishing compound (left). A stressed lap polish on the tertiary mirror was also performed using iron oxide (right), and better highlights the disparity in curvature of the two mirror portions [14]

the diverse range of optical design choices that can be made within the scope of extremely large optics.

While adaptive optics control is essential for correction of atmospheric-induced aberrations, active mirror control and phasing are also required for all of the NGT systems. One key component that is used for both adaptive and active optics are wavefront sensors. Each telescope system has a unique wavefront-sensing approach, different in design and location within the system. The TMT, for example, plans to utilize a series of sodium laser guide stars to help direct its adaptive and active optic control [18]. Additionally, unique tip/tilt on-instrument wavefront sensors will be used for dedicated tip/tilt/focus sensing in the near-infrared. The JWST presents another interesting demand in which the primary mirrors and secondary mirror will all have to be phased and aligned in space after deployment [19]. To achieve the required active mirror control and phasing a complex iterative approach has been developed, which will combine wavefront sensing with other approaches, as shown in Fig. 4.

Once the telescope systems are aligned, active and adaptive control has begun, and phasing of the segments is completed (when applicable), the NGTs will begin recording data. However, the demands on the systems do not diminish at this stage. For the ground-based systems, wind, earthquakes, gravity, and thermal effects can compromise the precise alignment required from the systems. These factors are coupled with the requirement that the telescopes track their targets at high speeds and with great precision.

The extremely large telescope structures require novel designs to meet the size, accuracy, and speed requirements. While traditionally telescope domes have vertically sliding shutters, the sheer size of the required apertures for the extremely large telescopes made this approach undesirable. Thus, the GMT, E-ELT, and TMT all have different methods of achieving the required viewing aperture for the telescopes [20]. One commonality is that a horizontally opening aperture is frequently used. The DKIST design is an exception because it has tighter requirements on fast and accurate tracking of the sun with the aperture. This demand drove the enclosure design to make use of a novel crawler track which, when coupled with the overall enclosure design, allows for fast azimuthal and horizon tracking of the sun to high accuracy [21]. Other concerns such as minimizing stray light and wind control are major drivers in the design choices of the enclosures. Minimizing turbulence/convection in the airflow throughout the dome and providing stable/uniform temperature control of the telescope are also critical to reduce dome-seeing. Mounting stability and stiffness must be considered as well for such enormous and heavy structures and components, particularly when mirror positioning accuracy is of prime importance.

With telescopes going on-line as soon as 2019, the next generation of telescopes is finally upon us, ushering in a new era of global astronomical science. At all levels, these systems require novel technologies to enable new

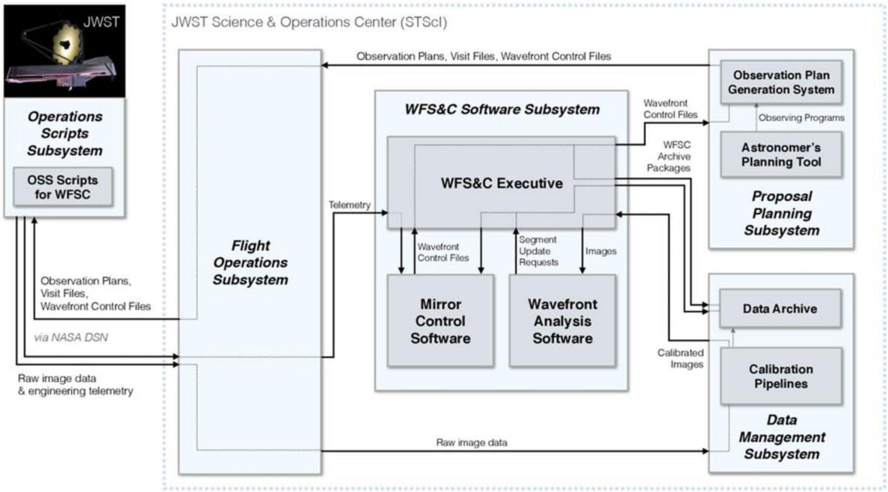

Fig. 4 The JWST must achieve and maintain proper mirror phasing and positioning once it reaches the proper orbit in space. Because further adjustments become prohibitively challenges once launched, the JWST will have a robust system for this alignment. The telescope utilizes a complex system, whose flow chart is shown, to provide active mirror positioning, mirror phasing and wavefront analysis [19]

breakthrough science. This paper seeks to summarize the methods utilized to create these powerful and timeless scientific instruments, which remain in use often for over a century.

2 Telescope Optical System Design

A key aspect enabling the science in the NGTs are the optics in the system, from the primary and secondary mirrors to overall optical design. Primary mirrors for the next generation of telescopes will use freeform shapes to achieve improved imaging quality. Freeform optics, optical surfaces which deviate from a standard spherical shape and typically are non-axisymmetric, have become increasingly integral in modern optical systems [22]. Further, a wider range of materials, from the standard borosilicate glass to the more exotic Zerodur and beryllium are being used to fabricate telescope optics. The primary mirror overall shapes additionally extend from standard circular apertures to hexagonal apertures. Thus, there is a wealth of new techniques and science being employed in the design of the NGT primary mirrors.

The extremely large telescopes are one area pushing the primary mirror optical design. Unfortunately, there is no practical way to handle (during a manufacturing process), test (requiring an enormous test tower), assemble (with an optical accuracy), and ship (to the final observatory site) a monolithic over 20-m in diameter precision mirror. To create such large primary mirrors, the fabrication consensus has been to fabricate multiple mirror segments which will be combined to create the overall primary mirror for these systems. To satisfy this approach, the GMT makes use of 8.4-m diameter segments, while the E-ELT and TMT utilize many smaller hexagonal segmented mirrors approximately 1.5-m in size. Each approach has unique fabrication and metrology requirements which impact other aspects of the design.

The GMT will provide observations across an extremely large spectrum, from 320 nm to 25 µm, and utilizes a fast-aplanatic Gregorian optical design with a final *f*/8.2 focus [17]. Figure 5 demonstrates the proposed GMT observatory. By using only seven segments for the primary mirror, phasing involves few parameters and the primary surface area (24.5 m diameter) is maximized. The segments are made of E6 low-expansion glass generated in a light-weighted honeycomb design. The telescope will provide a 20 arcmin FOV with a wide field of view corrector. The structure allows for 11 instruments to be simultaneously mounted with rapid optical path selection capability. The adaptive secondary mirror (ASM) is composed of seven 1.05-m segments which have deformable surfaces. Additionally, there exists a fast steering mirror (FSM) assembly, composed of seven optically identical segments, which can be switched out for the ASM [17]. Of the primary mirror segments, six are highly aspheric, with up to 14 mm of aspheric departure. One beneficial aspect of both the ASM and FSM secondary assemblies is their ability to correct minor positioning errors of the primary segments, which greatly relaxes the opto-mechanical constraints on the structure. Finally, one of the more distinctive characteristics of the GMT system is its use of a direct focus, with the instrument platform located directly below the primary mirror. This departs from the increasingly common Nasmyth platform design choice and allows instruments to record light after only two reflections, from the primary and the secondary mirrors, increasing system efficiency and compactness.

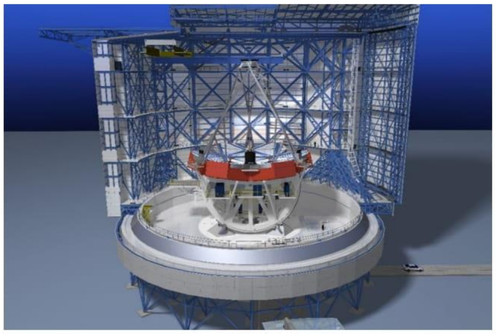

Fig. 5 The GMT telescope will be a relatively compact extremely large telescope. The optical design is a fast-aplanatic Gregorian design. The primary mirror is composed of seven 8.4-m diameter segments, for a total clear aperture diameter of 24.5 m. The secondary mirror is constructed from seven complimentary segments and will provide active and adaptive control. The final focus is located just below the primary mirror where instruments will be located for various observational studies. Image Credit: Giant Magellan Telescope GMTO Corporation

The E-ELT, on the other hand, makes use of a series of segmented hexagonal mirrors to create a primary mirror with an overall diameter of 39 m. For the E-ELT, which is a three-mirror anastigmat design used on axis, the primary mirror will be constructed from 798 segments of special low-expansion Zerodur glass, which measure roughly 1.45 m from point to point and are 50 mm thick. Figure 6 shows the conceptual diagram of the final E-ELT telescope design. The use of smaller segments allows for more rapid fabrication, which is essential as the project schedule calls for extremely rapid production and installation of the segments [23]. The secondary mirror is a convex asphere measuring 4.1 m in diameter and will be located 30 m above the primary mirror. The tertiary mirror is a concave mild asphere which will be located near the vertex of the primary mirror and

Fig. 6 The E-ELT telescope, the largest of the extremely large NGTs, is a three-mirror anastigmat on-axis design. Nearly 800 individual hexagonal segments will be used to construct the primary mirror, which is 39 m in diameter. The light travels to a suspended convex secondary mirror 30 m above the primary and from there to a concave tertiary mild aspheric mirror. Flat adaptive mirrors guide the light to instruments, located on two Nasmyth structures. Image Credit: ESO

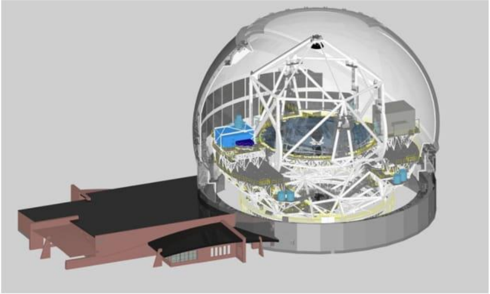

Fig. 7 The TMT telescope uses a Ritchey–Chrétien optical design which was guided by lessons learned from the Keck Observatory. Like the E-ELT, the primary mirror is composed of hundreds of hexagonal mirror segments. The secondary mirror is a hyperboloid which provides a final *f*/15 focus ratio. A tertiary flat mirror steers light to the Nasymth structure, where instruments are located. Image Credit: TMT International Observatory

will measure 3.9 m in diameter [9]. The emerging beam is approximately *f*/18 at this point, and here the design departs significantly from the previously mentioned GMT in that two additional flat mirrors are used to guide the light to the Nasmyth focus. These flat mirrors—which constitute the fourth and fifth mirrors in the system—are a 2.5-m flat deformable mirror and a 3-m × 2.5-m flat mirror, respectively. These mirrors will not only guide the beam but also provide atmospheric aberration correction.

The TMT telescope similarly will make use of 492 hexagonal segments that are 1.44 m point to point, 45 mm thick, and made from a special low-expansion Clearceram glass in order to create a primary mirror with a 30-m overall diameter [24]. The hexagonal design allows for tight packing of the segments and low weight, at the cost of a greater challenge of aligning and phasing so many mirrors. The TMT system will, for example, have over 10,000 degrees of freedom in the final system, all of which must be operating in precise coordination to achieve the required positioning and alignment of the system [25]. The telescope optical design is that of a Ritchey–Chrétien with an *f*/1 primary and an *f*/15 overall focus ratio [26]. Figure 7 highlights a cross section of the final system. The TMT has been designed with lessons learned from the Keck Observatory, and thus certain design and fabrication choices have been made to streamline and improve the overall structure. The secondary mirror is a 3.6-m diameter hyperboloid which provides the final *f*/15 focus ratio, and a tertiary flat steering mirror will guide the light to a Nasymth structure. The system is an optical-infrared telescope and the mirror coating will be a protected silver coating, which will provide high reflectivity and low emissivity in the planned imaging bands.

The JWST will make use of 18 hexagonal segments to construct its 6.5-m diameter primary mirror. However, the science requirements for JWST are significantly different from those of the ground-based telescopes discussed, and thus some unique design choices were made. The primary mirror segments are crafted from O30 Beryllium. To minimize the mass of the mirrors, they went through a final shaping process whereby much of the back side was removed, leaving a “rib” structure that keeps the segment shape steady. The light-weight segments thus have 92% of the original mass removed [27]. The mirrors were then polished and had a gold coating applied with a thin glass (SiO_2) protective overcoat to provide high reflectivity in the 0.6–28.5 µm infrared bands the telescope is designed for. The overall optical design is that of a three-mirror anastigmat (TMA). The light will be sent from the primary mirror to the secondary and from there to a protected tertiary mirror and finally to a fine steering mirror (FSM). The tertiary mirror is located behind the Cassegrain focus, while the FSM is located at the pupil image. The optical layout is shown in Fig. 8 and surrounded by a large solar shield to minimize thermal disruption.

Of course, not all the NGTs require a segmented primary mirror. The DKIST will make use of a single 4.2-m diameter off-axis parabolic primary mirror [16]. The mirror is a monolithic piece of Zerodur glass, which is essential to

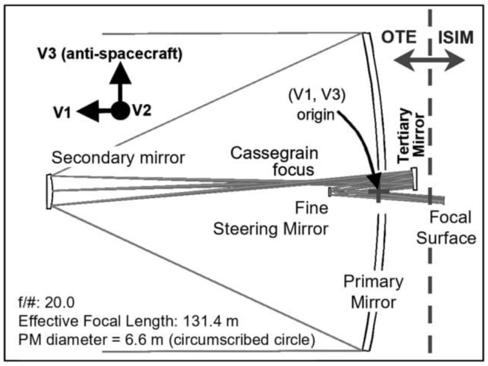

Fig. 8 The JWST will be the preeminent infrared space telescope when launched. Due to the constraints of launching a telescope, the design was guided strongly by minimizing weight and size. The system makes use of a three-mirror anastigmat design, allowing for minimal structure which still provides excellent optical performance. The telescope itself will unfold once it is deployed in space [27]

control thermal expansion during direct imaging of the Sun. Light is guided to a 70-cm-diameter secondary mirror which provides Gregorian focus with a 5 arcmin telescope FOV and a spectral range from 0.3 to 28 μm. Due to the intense thermal loads, the system will be exposed to the primary mirror must be actively cooled and must control the scattered light to less than 25×10^{-6} that of the solar disk irradiance at $R/R_{\mathrm{sun}} = 1.1$ and $\lambda = 1$ μm [28]. Because the goal of the DKIST is to provide premier observing capabilities of the Sun, a suite of tools will be located at the Gregorian focus which can obscure parts of the field to support specific observing goals. After the secondary mirror, the beam will be guided to further scientific instruments by eight additional mirrors, $M3$–$M10$, where $M10$ is a deformable mirror. (Note: $M\#$ stands for the mirror number.) The DKIST full optical path is shown in Fig. 9.

Amid such diverse and unique optical design choices, one key commonality exists: freeform optics, which enable more compact optical system designs and highly tailored aberration control for specific science or optical applications. Whether segmented or monolithic, ground or space-based, circular or hexagonal, freeform optics are key enablers in

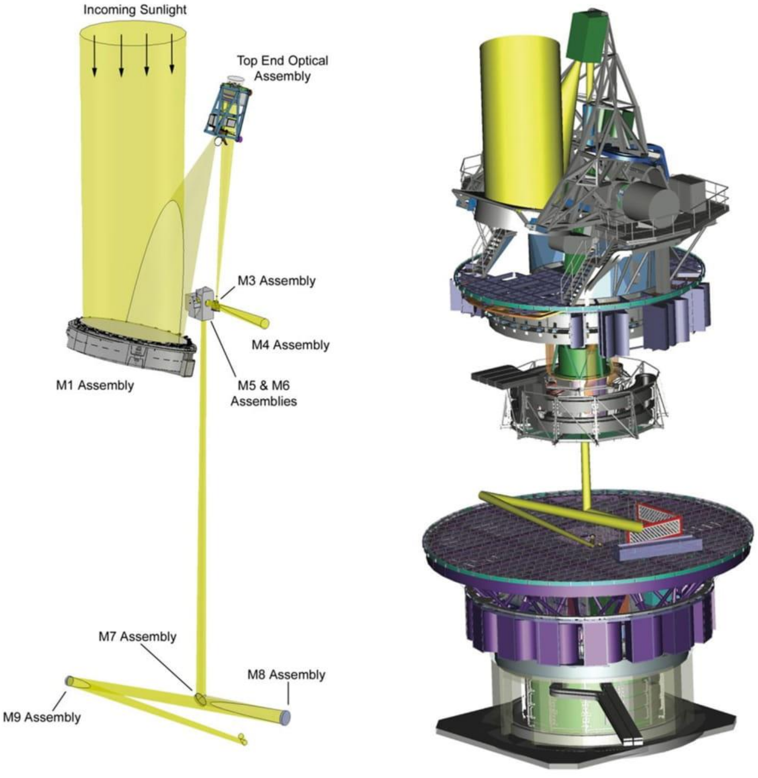

Fig. 9 The DKIST system will provide unprecedented observations of the Sun. The direct exposure to the Sun required for this mission calls for a novel design choice in the primary mirror to minimize thermal effect. The system uses a single monolithic Zerodur off-axis parabolic (OAP) primary mirror, which allows for the remaining optics to be in the optical path without obscuring the incoming beam. After the primary mirror, there are nine further mirrors which provide further beam focusing and steering to the science instruments [16]

the next generation of telescopes. This is a feature we can expect to see more of as today's fabrication and metrology teams have demonstrated their ability to create such optics to extreme precision.

3 Precision Manufacturing and Control Technology

3.1 Optical Fabrication Technologies

The design choices and theoretical performance of NGTs would amount to little without the capability to accurately fabricate the optics in the systems. The magnitude and complexity of surface shapes make for highly challenging fabrication processes. This challenge is compounded by the fact that the mirrors are made of different materials, over the course of a decade in some cases, and—after bending modes are applied—can only have a root-mean-square deviation from the ideal surface of tens of nanometers. However, not only have fabricators been able to deliver optics that meet all requirements, but they are now moving into higher efficiency and more streamlined methods which should allow for faster and more reliable production of advanced large optics. We explore some of the techniques being used to create the mirrors in these telescopes, from the materials to create the monolithic optics to the polishing and grinding tools used to generate the final surface figure. Today, multiple technologies are essential in freeform optical fabrication, including CNC machining and diamond turning and standard grinding and polishing as well as subaperture corrections via Magneto-Rheological Fluid (MRF) methods or other techniques [29–31].

It should be noted generally that several methods are used to generate the base surface of freeform optics. The optic shape can be achieved through CNC diamond turning, grinding of blanks, or even molded optics [32]. Diamond-turned optics can generate freeform shapes typically out of metal substrates with a multi-axis stage. The current limit on the precision that can be achieved with this technique is roughly 5 nm RMS, which, when followed by a smoothing run, can produce excellent freeform optical surfaces [33]. There are a range of other cutting methods which exist to shape precision surfaces. These techniques are essential in optical fabrication, allowing for nano- to micro level surface shaping [34].

One interesting technique which is sometimes applied for subaperture surface corrections is the MRF approach. This technique utilizes a magnetic fluid which can be precisely guided to polish a surface to a high-quality finish. It is extremely effective in the fabrication of freeform surfaces up to and larger than diameters of 300 mm, reliably achieving surface finishes on the order of 150 nm PV (Peak-to-Valley) and 20 nm RMS [35]. As shown in Fig. 10, by polishing the surface, residual mid-spatial frequencies generated during subaperture correction techniques can be effectively removed to produce a smooth optical surface.

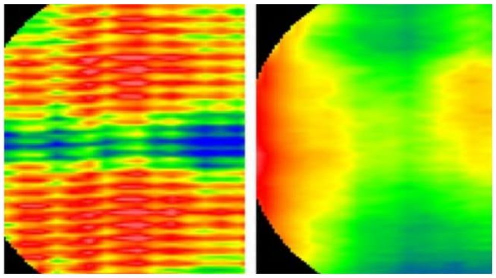

Fig. 10 Diamond turning involves using a diamond-tipped tool in combination with a CNC machine to achieve precise freeform fabrication over a variety of materials. After a first run, the process can leave mid-spatial frequencies on the optic surface (left). Thus a polishing run is required to smooth the mid-spatial frequencies out of the surface for the final optic (right) [29]

In the case of the GMT primary mirrors, a large rotating furnace is used to generate the glass primary blanks. To achieve high stiffness and low weight, the mirrors make use of a honeycomb back design. Coarse shaping occurs with diamond wheel cutting followed by loose abrasive grinding to remove tooling marks. Final shaping and polishing use traditional polishing compounds and computer-controlled polishing [36–38] shown in Fig. 11.

In this method, a tool pad is set in an orbiting motion with a spatially-dependent dwell time to control glass removal rate. Recent innovations in polishing include an actuated tool pad that is able to dynamically change shape for more precise glass removal, as well as a rigid conformal tool which uses a non-Newtonian visco-elastic fluid as the tool pad. Figure 11 demonstrates the rigid conformal tool being used for polishing of a GMT segment, and the estimated and measured removal maps as well as the designed dwell time for optimal surface figuring.

In the case of the E-ELT and TMT, where hundreds of segments must be produced, the demand for an efficient and rapid fabrication process becomes even more important [40, 41]. For the E-ELT the process starts with cast circular mirror blanks which are ground and rough polished and then cut to their hexagonal shape using a CNC machine. A unique grolishing process then fits in between the grinding and polishing stages to remove mid-spatial frequency surface errors [42, 43]. Next, the segments are attached to their mounting fixtures and undergo a version of the bonnet polishing method with a rotating, precessing compliant spherical tool [23]. The tool rasters across the surface, and by adjusting

Fig. 11 A visco-elastic non-Newtonian fluid is used in the rigid conformal tool during GMT primary mirror segment polishing (**a**). The surface removal after polishing (**b**) closely matches the predicted removal (**c**), with a difference of only 97 nm RMS (**d**).The tool is guided by a dwell time map (**e**), generated by software which predicts material removal via parametric modeling [39]

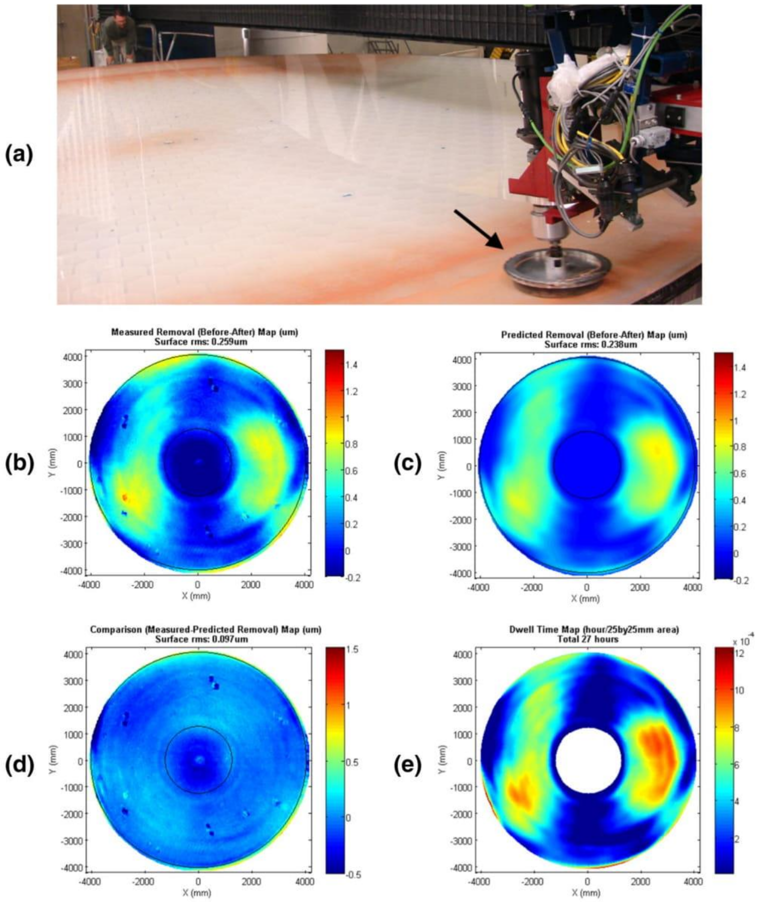

Fig. 12 The E-ELT primary mirror uses a multi-step process to generate the final mirror segments. Initially, a circular mirror blank is fabricated and sent for further processing (left). The circular mirror segments undergo grinding, and rough polishing. The mirror support is then prepared for bonding and the segments are cut into their final hexagonal shape (right). The support and segment are assembled, and final polishing runs then occur. Image Credit: ESO/SCHOTT

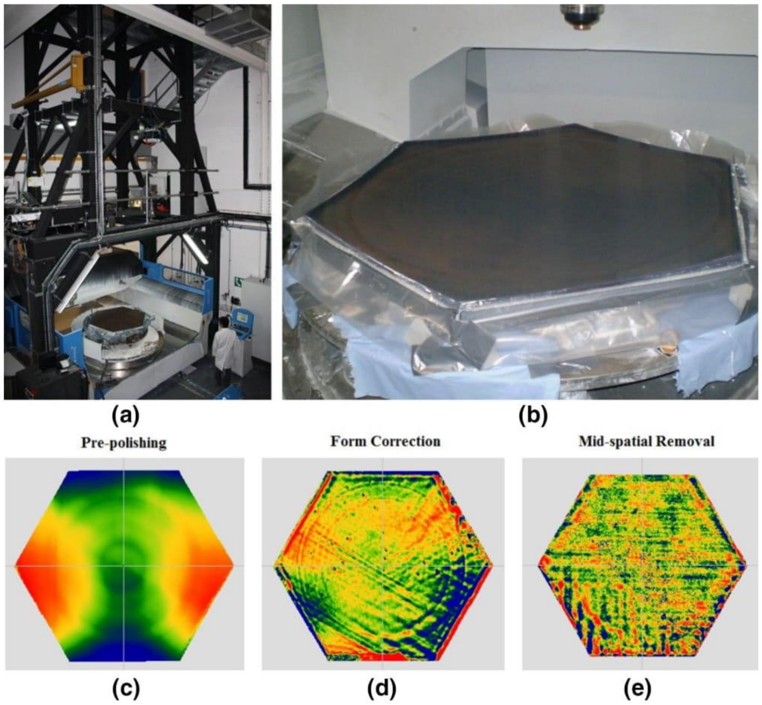

Fig. 13 During fabrication of the E-ELT primary mirror segments a combined in situ metrology process was performed to streamline the fabrication. The mirror segment is mounted on a polishing machine which is located under a metrology test tower (**a**). The surface is then polished to achieve the desired surface figure (**b**). At the pre-polishing stage the optical surface is dominated by low spatial frequencies errors, such as astigmatism (**c**). After form correction (**d**) the mid-spatial frequencies are removed using a unique grolishing technique (**e**), which fits between the polishing and grinding phases [43]

the pressing strength, the glass removal rate is adjusted. Figure 12 demonstrates the flow of the mirror fabrication process from casting to mounted optic.

Complimenting this process is a full aperture test tower which the machine sits under, allowing for in situ testing between fabrication runs. The configuration of this test process, as well as the surface figure progression, is shown in Fig. 13.

It should be noted that careful calibration of all tooling previously mentioned must be performed for accurate fabrication. Laser trackers, reference balls, self-centering probes, and advanced methods including a multilateration approach for geometric verification of a machine tool are essential for calibration of machine geometry prior to and during fabrication [44].

The JWST had to take a significantly different approach when fabricating the primary mirror segments due to the material used. The mirror blanks were generated using an optical grade beryllium powder, which was loaded into a hexagonal enclosure and underwent a hot isostatic press process which converted the material into a solid. The solid mass was then cut into two equal blanks and light-weighted to reduce the 250-kg mass of a single blank down to 21 kg

Fig. 14 After precision fabrication of the JWST mirror segments, they require a special coating. Due to the target infrared imaging band, the mirror segments utilize a high uniformity gold coating, which is achieved via vapor deposition. This provides high reflectivity in the imaging bands targeted. Additionally, a protective overcoat layer is applied to help shield the optical surface from damage once deployed [45]

by machining out much of the back structure of the blank to leave a fine ‘rib’ structure for support. The blanks were then ground and polished and transported to various other test facilities between initial and final polishing. For the coating, a vapor deposition process was utilized which created a high-quality, high uniformity gold coating with a protective overlayer [45]. Figure 14 shows a completed segment after coating.

3.2 Advanced Metrology Solutions

It is essential to utilize advanced metrology methods to guide and verify the optical fabrication process. The challenge this presents has grown significantly as more extreme freeform designs and larger optics are being utilized. Broadly, the metrology techniques used can be broken down into two major categories; contact and non-contact metrology. Both approaches are essential to fabricate the described optics, and interesting advancements have been made across the board [46].

The metrology methods used to guide and verify the fabrication of the optics in the next generation of telescopes must meet the precision and accuracy demands as well as the efficiency requirements for the optics. For example, the E-ELT telescope primary will require a total of 960 primary mirror (M1) segments, which includes extra mirrors for the manufacturing yield provision, to be produced over a period of 84 months [47]. Each of the E-ELT M1 segments is unique in shape and must have a final surface figure error less than 25 nm across the clear aperture. The metrology must be able to (a) meet the tight accuracy requirements in a repeatable way for the freeform segments, and (b) must not slow down the fabrication cycle significantly. This requires efficiency to be a strong consideration in the employed metrology approaches which will be employed at various fabrication sites, while also maintaining nanometer level form accuracy [48, 49]. For example, the grinding phase of fabrication can rapidly approach the desired surface figure, but metrology becomes extremely challenging as the surface is not specularly reflective in the visible band. Thus, traditional high-precision optical metrology methods, such as visible interferometry, cannot be applied. It is in this region where advancements in metrology have led to greatly reduced fabrication times by improving the accuracy of rough surface metrology, allowing for more rapid convergence of surface shape.

One approach to measuring surface figure error, particularly for rough surfaces, is using a swing arm profilometer (SAP). This technique uses a highly accurate probe which is mounted on a rotating arm such that its axis of rotation passes through the center of curvature of the tested optic [50]. The trajectory of the probe defines an arc that lies on a spherical surface defined by this center of curvature. The test measures the optical surface departure from this spherical surface and is capable of testing convex, concave, and flat optical surfaces. With the next generation of extremely large telescope optics in mind a SAP was devised as a collaborative project between the University College London and the UK National Physical Laboratory and was able to achieve repeatability of 40 nm RMS using a touch probe and a high-resolution stage system [51]. Alternatively, a non-contact optical probe can be used in what is known as a Swing arm Optical Coordinate-measuring-machine (SOC) test, and has produced surface figure results comparable to a Fizeau Computer-Generated Hologram (CGH) interferometry test [52]. To achieve this, a dual probe shearing method is utilized to calibrate the system. The dual probe shear calibration approach is essential as the arm will have systematic errors from the arm bearing. Because both probes see the same bearing errors while measuring different areas of the test surfaces, the error can be calibrated out. Figure 15 demonstrates the SOC process as well as the accuracy of the SOC system as compared to a Fizeau test of a 1.4-m diameter aspheric surface with 300 μm of aspheric departure.

An interesting novel development which reverses the SAP concept has recently been reported, described as a Swinging Part Profilometer [53]. The concept is like the SAP, except instead of the probe swinging, the optic under test is placed on a rotation table and is rotated under the probe. One obvious benefit of a fixed probe is that the SAP method can be deployed for in situ metrology of a part during fabrication. The key requirement is that the optic is mounted on a rotary air-bearing or hydrostatic table, which would lend itself nicely to a CNC fabrication process. One challenge is that for lateral motion the optic must move while a counterweight maintains proper balance of the table. The method has successfully been applied to testing flat optical surfaces and was able to exceed the expected probe accuracy of 300 nm.

One final contact metrology method for rough surfaces is the utilization of a laser tracker [54]. A laser tracker is a device that uses two angular encoders and a distance-measuring interferometer (DMI) to measure the position of a retroreflector in 3 dimensions. DMIs offer excellent distance measurement capabilities, and significant research is constantly being performed to improve the technology. Recent advancements include utilizing mode-locked lasers for improves distance measurement performance [55]. To complement the laser tracker, and account for rigid body motion as well as air refractive index variations, the laser tracker metrology approach utilizes four independent DMIs which measure retroreflectors at the mirror edge continuously. In this way, the rigid body can be well defined, and the laser tracker position measurement can be calibrated. For the measurement itself, a spherically mounted retroreflector is moved via computer-controlled motion over the mirror and independent measurement points are taken across

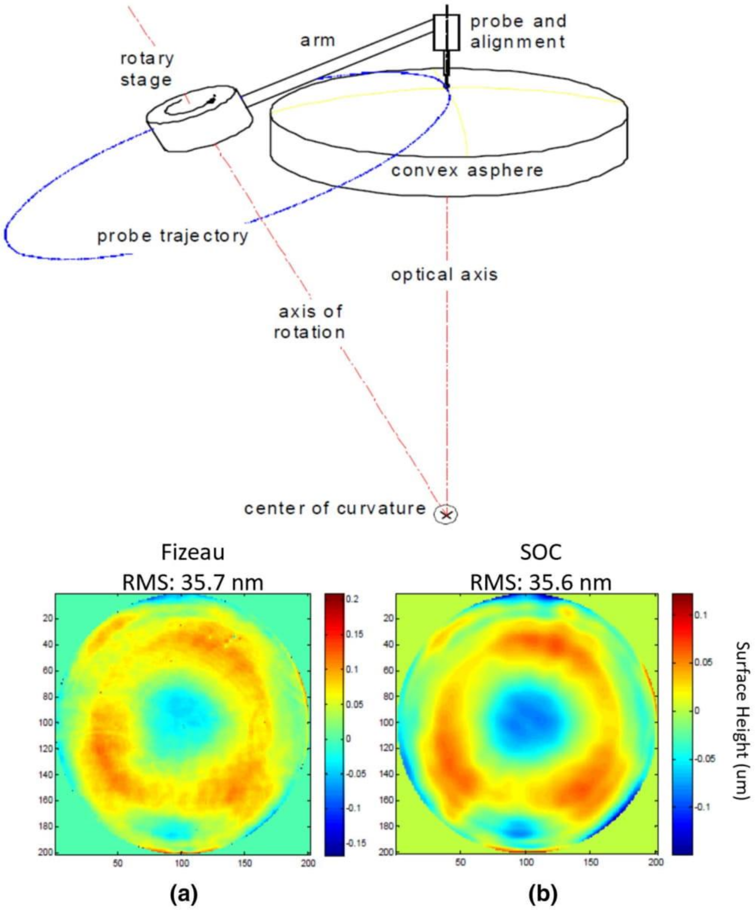

Fig. 15 A swing arm profilometer (SAP) has been used to great success in measuring the surface form of several precision large optics (top). The method utilizes a probe tip, either optical or touch, which is swung over the optic under test. Simultaneously, the optic is rotated on a precision rotation table and the resulting acquired data is stitched together to form a full surface map. To demonstrate the capabilities of the method, a Fizeau test of an optic (**a**) was compared to an SAP test which used a dual probe shear calibration method (**b**). The Fizeau test data reported a surface RMS of 35.7 nm while the SOC (Swing arm Optical Coordinate-measuring-machine) reported 35.6 nm RMS. The direct subtraction shows a difference of only 9 nm RMS [52]

the full aperture. The points are then combined to form a surface map of the optic. For the first segment of the GMT telescope, the method was able to provide independent corroboration of low-order metrology results for the surface with accuracy exceeding 1 µm RMS.

For non-contact optical metrology of rough surfaces infrared-based deflectometry has recently been successfully integrated into the metrology plan of several of the optics in the NGTs as a rapid, high accuracy and high dynamic range non-null metrology method. Deflectometry fundamentally measures the deflection of a ray of light, which originates at a known source location, off of a test optic and onto a recording device such as a camera [56]. The technique is a non-null metrology method and has been utilized in measuring freeform optics [57]. For rough surfaces, a hot scanning source, such as a heated tungsten ribbon or heated ceramic rod, provides radiation in the thermal-infrared spectrum that can specularly reflect from surfaces with roughness as high as 50 µm RMS [58]. The system was utilized in the DKIST fabrication and was able to greatly enhance the efficiency of fabrication, providing accurate metrology results during the grinding phase, which is often ~ 1000 × faster removal process than the final polishing phase, by reporting surface figure error with a sampling of roughly 512 × 512 points across the 4.2-m surface down to below 1 µm of RMS departure from ideal [59]. A surface reconstruction from a deflectometry measurement taken during 40 µm grit loose abrasive grinding of a 6.5-m diameter mirror is shown in Fig. 16 and illustrates how the rough surface measurement capabilities of the technique.

Another non-contact method for testing large figure error of the base shape is a scanning pentaprism test [61]. This test

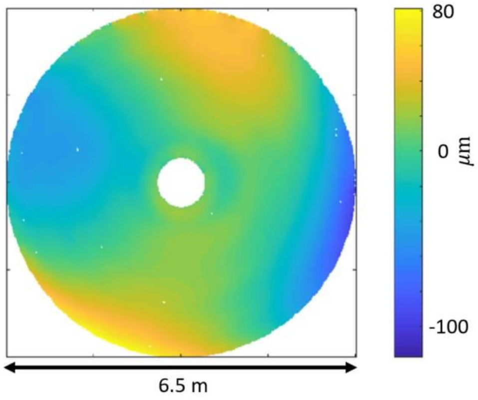

Fig. 16 The grinding phase of fabrication of an optic allows for extremely rapid convergence to the desired surface shape. Above, after grinding a 6.5-m optic with a 40-μm grit, the surface is tested with an improved infrared deflectometry system which uses a heated ceramic rod as the source and the surface map is reconstructed [60]

utilizes a pentaprism to scan a collimated beam across the optical test surface and measures the focus of the reflected beam. The technique has achieved slope accuracy down to 1 μrad RMS. Also, a novel method known as Exact Autocollimation Deflectometric Scanning (EADS) was able to achieve extremely high-precision measurement of surface slopes of a tested optic and shows great promise for measuring flat optics [62]. The method uses a null instrument which sends a signal through a scanning pentaprism to the optic surface. The optic itself sits on two points, one of which is a piezo-actuator, and the surface is tilted to achieve a null in the null instrument. Simultaneously, a mirror is mounted perpendicular to the optic and reflects the tilt of the optical surface. An instrument measures the precise tilt of the mirror and the local slope of the optic can be determined to high accuracy. Figure 17 demonstrates the theory behind the testing method.

Moving toward smoother surfaces allows for more accurate optical metrology methods which operate in the visible spectrum to be utilized. One such method is Phase Shifting Deflectometry (PSD), which is similar to the infrared deflectometry mentioned earlier but adapted for improved visible-light performance. Instead of a heated scanning source, a digital screen is used to display a sinusoidal pattern which is phase shifted as a camera records the reflected images. This technique has been used in testing multiple large precision optics [56, 63, 64]. The setup for the concept is demonstrated in Fig. 18.

With careful calibration, PSD can extend metrology down to very fine surfaces, where interferometery excels. This has been demonstrated with 1 nm RMS surface height accuracy demonstrated with x-ray mirrors [65] and can achieve 300 nanoradian RMS slope precision [66]. Figure 19 demonstrates the acquisition and calibration process for a PSD system employed on a recently produced 6.5-m mirror, as well as the surface test results compared to an interferometric test.

The traditional fine-surface metrology technique of interferometry is undergoing improvements. One important area that has made great strides is subaperture stitching interferometry. This method is essential when testing large convex optics, which are featured in several next-generation telescope designs. Recently, a method which utilizes a reconfigurable null test was devised which utilizes a multi-axis platform and two rotating Computer-Generated Holograms (CGHs) to minimize systematic errors in subaperture

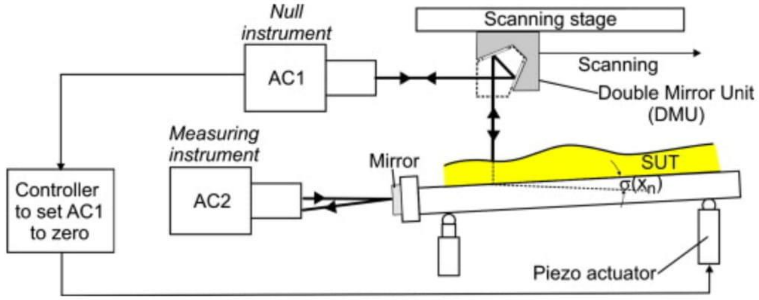

Fig. 17 Large flat mirrors are integral optical components in several of the NGTs. One method to achieve precision metrology of such surfaces is the EADS. The EADS principle utilizes a piezo-actuator to set the zero of AC1 (Autocollimator 1) at each position, while AC2 measures the precise slope. The system is able to achieve extreme precision for slope measurements and has been proposed to measure the flat mirrors used in large telescopes [62]. Reprinted from *Nuclear Instruments and Methods in Physics Research Section A: Accelerators, Spectrometers, Detectors and Associated Equipment*, Volume 710, *M. Shulz, G. Ehret, P. Kren*, *High accuracy flatness metrology within the European Metrology Research Program*, Pages 37–41., Copyright (2013), with permission from Elsevier

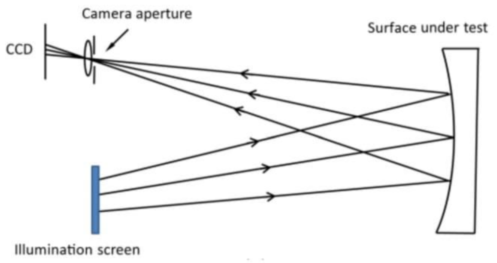

Fig. 18 Deflectometry has been used recently for metrology on several of the NGT optics, including the 4.2-m DKIST primary mirror and 8.4-m GMT primary mirror segments. The method uses a source which emits light at a known location. The light deflects from the optic under test and is recorded by a camera. By knowing the precise 3D location of all components, the local slope of the optic under test can be determined, and the surface sag is determined by integrating the local slopes [65]

measurements of a large convex asphere [68]. The acquisition and stitching process is demonstrated in Fig. 20.

For optics that are not highly convex one of the absolute best metrology results that can be achieved is via full aperture high-precision interferometry. As interferometry is a null-test method, it requires a null configuration to obtain the best test results. This typically can be achieved by using an appropriate optic to null out the test optic; however, the process becomes more complicated for a freeform optic. To achieve the highest level of testing for freeform surfaces, using a custom Computer-Generated Hologram (CGH) is a commonly preferred method. Figure 21 demonstrates a custom CGH and the resulting fringe pattern.

One additional benefit of CGHs is that they can provide advanced alignment of the null configuration by utilizing additional alignment holograms outside of the main testing aperture of the CGH. Because the external references are generated at the same time as the main null pattern, they are aligned to the accuracy of the lithographic process that created the CGH [69]. The result is a better aligned, higher performance custom null configuration which can achieve extraordinary precision metrology of the freeform optics. It should be noted that even with the improved alignment and nulling features a CGH presents, the exact implementation for testing some of the described optics may introduce distortion in the interferometric setup which must be mapped

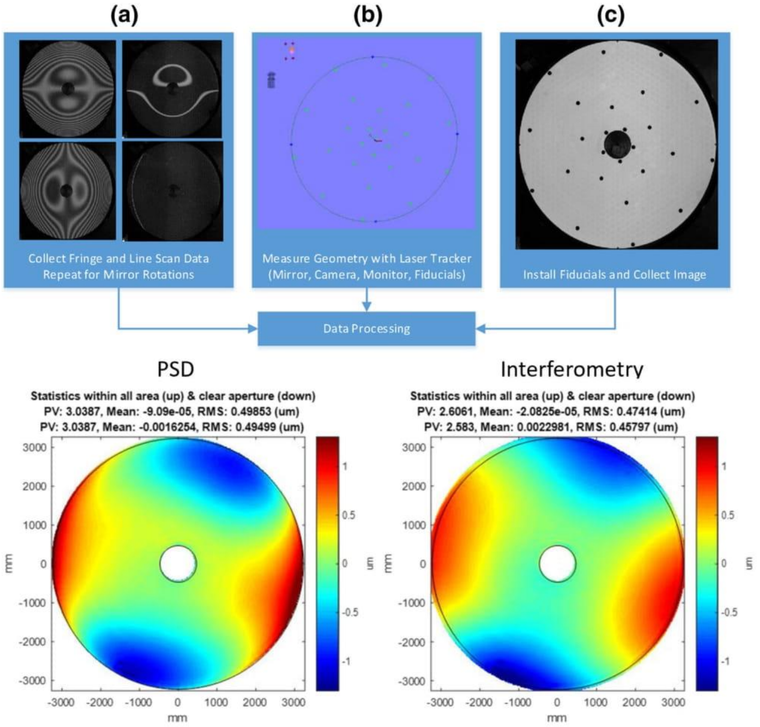

Fig. 19 Phase Shifting Deflectometry (PSD) and line scanning (**a**) are two common deflectometry source approaches. For the highest precision the geometry of the deflectometry test system is measured with a laser tracker (**b**) and fiducials are applied to the optic to map the camera distortion (**c**). Using this calibration approach, a PSD measurement (bottom left) achieved similar results to an interferometric measurement (bottom right) of a 6.5-m optic [67]

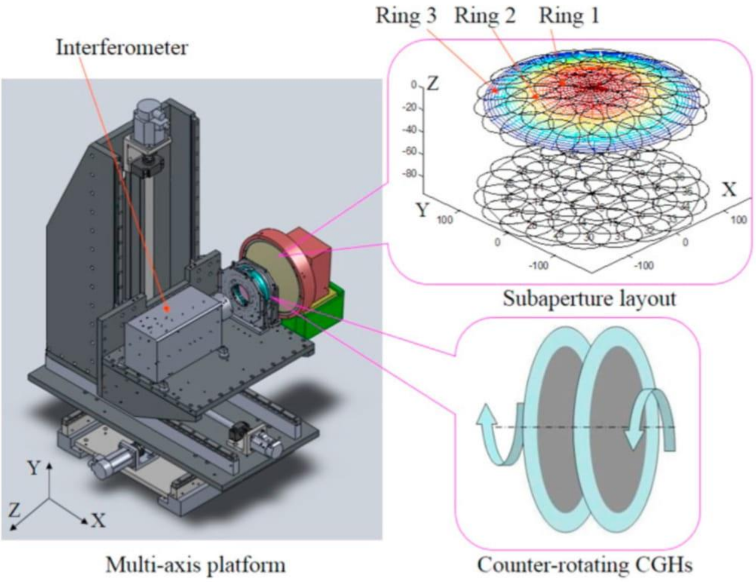

Fig. 20 Subaperture stitching interferometery allows for precise interferometric measurements of large surface that cannot be measured using a standard interferometric test. By utilizing a multi-axis platform to carefully adjust the measured subaperture (left) and counter-rotating CGHs (bottom right), a full map of the optic surface is obtained (top right). The subapertures are stitched, and system errors are calibrated out to produce a high-quality map [68] Reprinted from *Optics & Laser Technology*, Volume 91, *S. Chen, S. Xue, Y. Dai, S. Li*, *Subaperture stitching test of convex aspheres by using the reconfigurable optical null*, Pages 175–184., Copyright (2016), with permission from Elsevier

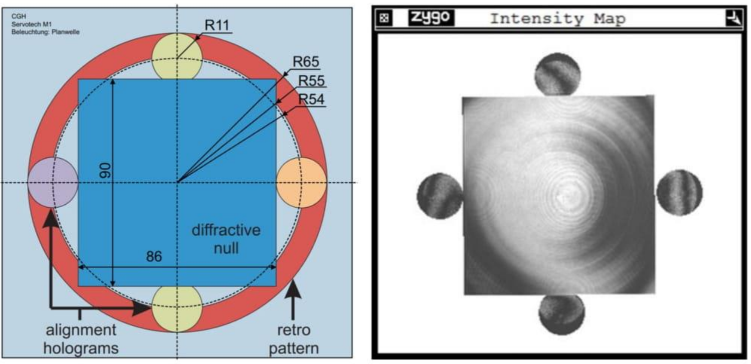

Fig. 21 For freeform optics, a custom null optic is required to achieve adequate fringe density over the entire optic aperture. A Computer-Generated Hologram (CGH) is an accurate way to generate extremely high-precision custom null optics and can feature helpful alignment features (left). When used, they can provide a proper fringe density for testing even over a highly freeform surface (right) [69]

and calibrated to achieve a high accuracy metrology result [70].

Another metrology system that must be noted is the highly unique cryogenic center of curvature test system used for the JWST [71]. The test system consists of a multi-wavelength instantaneous interferometer, a calibration system, and a reflective null. Due to the long path length required for the center of curvature test, the instantaneous interferometry becomes essential to eliminate random variations arising from vibrations, which with multiple tests can be averaged out. The system achieved a wavefront error (WFE) repeatability of 10.8 nm RMS. Figure 22 demonstrates the test results for a segment of the JWST using the cryogenic center of curvature test.

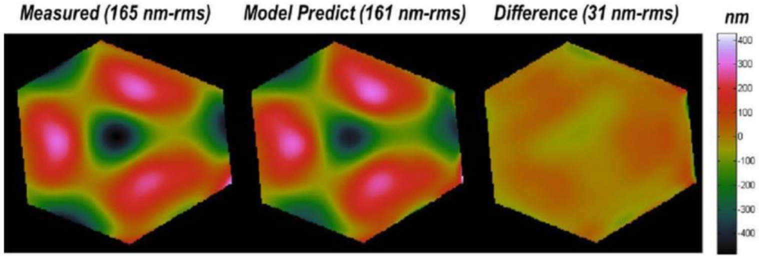

Fig. 22 The JWST mirror segments have extremely tight surface figure tolerances. Thus, a multi-wavelength instantaneous interferometer was an essential tool for measuring surface figure. The measured figure of one segment (left) is compared to a model-predicted surface (middle) and the difference of 31 nm RMS across the surface (right) was determined [71]

3.3 Large Primary Mirror Alignment and Co-phasing

Once the optics have been fabricated and meet specifications, they must be assembled and aligned. Not only must the mirrors be aligned relative to each other to create a well-aligned optical system, but for the segmented mirrors, co-phasing becomes essential. Additionally, proper alignment must be maintained throughout testing, where thermal gradients, gravity, and vibrations can cause small motions in the positions of the optics.

For systems such as the E-ELT and TMT, where there are hundreds of segments in the primary mirror, this alignment and co-phasing is a complex process. Because the steel structure which will support the optics is not sufficiently accurate to align the optics in these systems, additional interface structures, known as Fixed Frames in the E-ELT case, will be installed on top of the structure and aligned in six degrees of freedom to achieve the proper optical alignment [72]. The rigid fixturing is only the first step in the alignment for the large optics at play in these telescope systems. To get better performance active alignment and, in the case of segmented mirrors, co-phasing are required.

The TMT system uses an Alignment and Phasing System (APS) to control the 10,000+ degrees of freedom of the primary, secondary, and tertiary mirrors that constitute the system. The APS system, which is based on the Keck Telescope alignment system, is a Shack–Hartmann wavefront sensor which provides the pre-adaptive optics alignment for the TMT system [73]. The APS system adjusts the segment pistons and tip/tilts, the segment surface figure (by warping harness adjustments), the secondary mirror piston and tip/tilt, and the tilt and rotation of the tertiary mirror [74]. The typical test case for the system will be as follows: the telescope will be pointed at a star, the Acquisition Pointing and Tracking (ATP) camera will acquire the star, minor adjusted are made to center the star, and then the guiding process will begin. Based on the wavefront sensing, the system will then adjust the active position and phasing of the optics in the system.

The GMT primary segments have active control to correct figure, while the secondary segments have both active and adaptive control and can correct for phasing. Like the TMT, Shack–Hartmann sensors are used in conjunction with a guide star to determine mirror alignment, phasing, and shape error via ground-based adaptive optics. The design calls for a dispersed Hartmann design, with 1.5-m

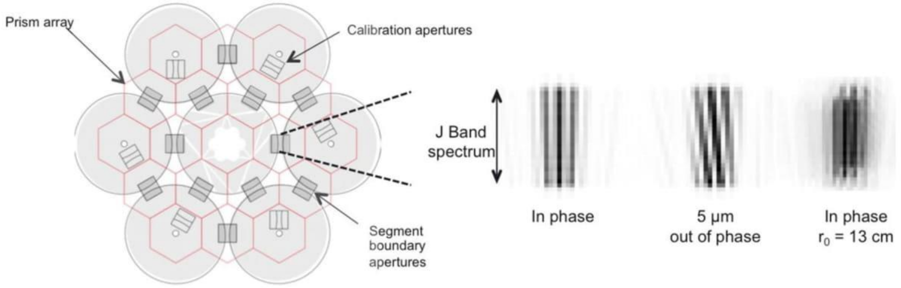

Fig. 23 The GMT, with its seven 8.4-m in diameter mirror segments (left), requires advanced mirror phasing to achieve proper alignment. The system will use a phasing camera system operating in the J band which, using dispersed fringes, will guide the phasing of the mirror segments. When the mirrors are properly in phase a correct fringe pattern is achieved. The out of phase error is reflected in the fringe pattern by tilted fringes, allowing the system to correctly guide the mirrors to proper phasing. r_0 represents median Fried parameter [17]

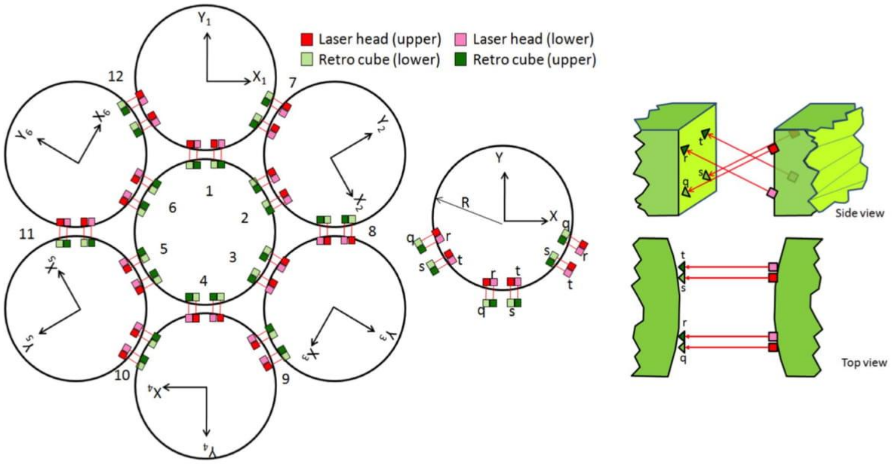

Fig. 24 The primary mirror of the GMT has seven segments that must be properly aligned to each other to within 10 nm. To accomplish this, distance-measuring interferometers (DMIs) will be used to monitor the positioning of the mirrors during operations and will guide correction of position. The DMIs use a laser which is reflected by a retro cube to measure distance to within 5.9 nm RMS and to ~ 0.01 µrad in tilt [77]

square apertures arranged at the tangent of each segment [75, 76]. These apertures create interference fringes, which are measured by a Dispersed Fringe Sensor (DFS) in an infrared channel. The patterns are recorded in the J band (1050–1350 nm) over a short integration time (10–20 ms) using a SAPHIRA eAPD array. This approach will be used to achieve optical path differences of less than 85 nm RMS between segments [17]. Figure 23 demonstrates the fringe phasing concept. After this step, a pyramid-based natural guide-star wavefront sensor (NGWS) will be used and can control piston to within 30 nm RMS.

To measure the position of the primary segments during observations an interferometric metrology system will be used. Distance-measuring interferometers will be used in 24 pairs to measure distance shifts of 5 nm but also are able to measure large motions during initial alignment of up to 3 cm. A similar network of distance-measuring interferometers will be used to monitor the alignment of the secondary mirror segments. Figure 24 illustrates the geometry of the laser truss at $M1$.

3.4 Active and Adaptive Optics Control

While the complex optical designs allow for extremely high-quality imaging and superb light-collecting capabilities, both active and, for ground-based systems, adaptive optics are required to achieve the desired system performance of these telescopes. This need is answered in an equally diverse set of methods as the optical design choices for the systems described. It must be considered as well that while some systems, such as the DKIST or LSST, have very specific science goals, the extremely large telescope systems have a wide variety of different observation goals and thus require a variety of different observing modes. Because of this, all the systems require advanced positioning control for slower shifts and mechanical drift. This control is provided by the active optics in the system.

On the other hand, for the ground-based telescopes, atmosphere-induced aberrations must also be controlled, or the imaging capabilities would be severely limited. This presents an interesting problem, as with increasingly large mirror areas the feasibility of adaptive optics covering such areas becomes challenging. Thus, a greater variation in design choices arises with the adaptive optics approach, whether they are implemented in the secondary mirror as is the case in the GMT, or in final stage deformable mirrors, as is the case in the E-ELT, TMT, and DKIST. To enable adaptive systems, a method is required for determining the wavefront that must be corrected. This is increasingly being accomplished using extremely powerful sodium guide-star lasers which create an ideal guide star. Similarly, while certain unique choices have been made to create highly accurate wavefront sensors, the base theory still mostly relies on Shack–Hartmann sensors. However, the exact implementation of the wavefront sensors is typically unique to the

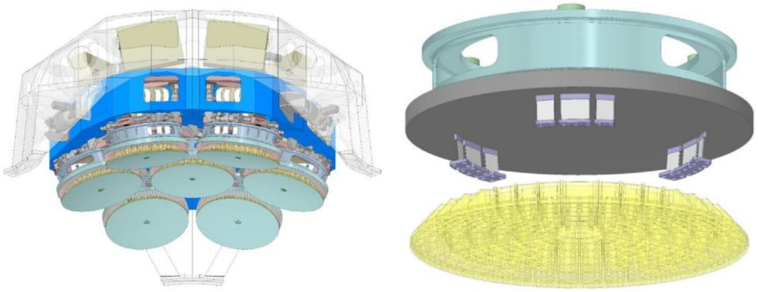

Fig. 25 The GMT secondary mirror makes use of seven paired segments (left), which are mounted into a Zerodur reference body. The secondary mirror segments are complementary to the primary segments and can be actively driven. Additionally, a suite of actuators provides adaptive control to the secondary mirror segments (right) [17]

telescope requirements, as seen in the curvature wavefront sensor implemented for the LSST [78].

While a number of the NGTs utilize a flat deformable mirror either near the end of the optical train or integrated into the science instruments, the GMT instead uses an adaptive secondary mirror. The GMT secondary will provide both active optics and adaptive optics. Because these two systems were designed in conjunction for the GMT, they broadly fall under the wavefront control (WFC) system [17]. Figure 25 demonstrates the mount for the GMT secondary segments. Included in the system are four distinct wavefront control modes.

The ground layer AO observing mode requires active control of the primary mirror ($M1$) segment positions and figure with fast (100 Hz) control of the secondary mirror ($M2$) figure. Because each of the seven primary segments is matched to a segment of the secondary mirror, active positioning control of the $M2$ segments can directly compensate $M1$ position errors. Additionally, a natural guide star observing mode will deliver a high contrast, diffraction-limited Point Spread Function (PSF) in the near-infrared. Finally, laser tomography adaptive optics can be used to reconstruct the high-order components of the atmospheric wavefront error in the direction of faint on-axis targets.

Four general-purpose natural guide-star wavefront-sensing probes located 450 mm ahead of the direct Gregorian focus provide the feedback for the natural seeing and GLAO observing modes. The diffraction-limited natural guide star and laser tomography observing modes require additional wavefront sensors in the instruments. Each diffraction-limited instrument is therefore equipped with a pyramid wavefront sensor for use when a bright natural guide star is available, and a set of 6 Shack–Hartmann wavefront sensors for use with a constellation of laser guide stars.

The TMT also is planning to make use of an adaptive secondary mirror [18]. Plans have investigated using a single Adaptive $M2$ (AM2) mirror that acts as a ground-based adaptive optic system. This design choice would allow for

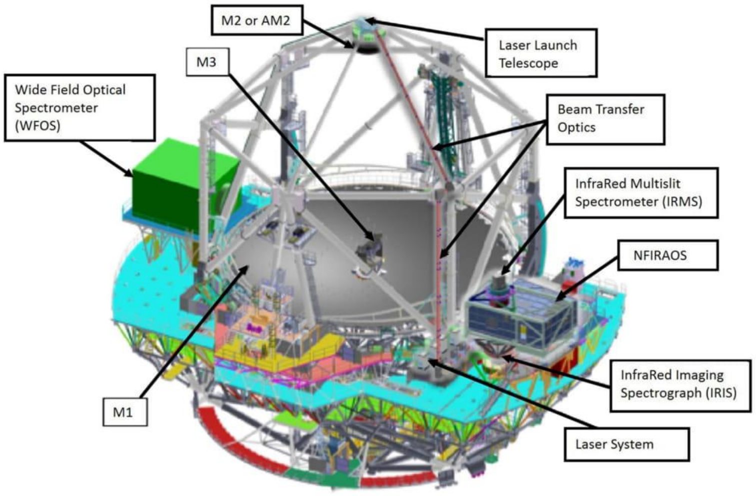

Fig. 26 Adaptive optics control is essential for the observations performed by the NGTs. After extremely precise manufacturing and alignment, constant adaption of the optical system to atmospheric turbulence and other motions (gravity, wind, etc.) must be performed to maintain the system requirements. The TMT system will utilize adaptive optics in the steering mirrors and inside of the instruments on the Nasymth stations. Additionally, a laser launch telescope will be used to produce a laser guide star, using powerful sodium lasers [18]

a simplification in the instrument adaptive optics. Although the adaptive *M*2 is in a planning stage, there is a suite of other adaptive optical control systems that will be utilized. The adaptive optics system itself is heavily incorporated into the primary instrument for the TMT, the Narrow Field IR Adaptive Optics System (NFIRAOS). The system utilizes a series of advanced wavefront sensors and deformable mirrors and a separate guide laser system. The guide laser will be composed of six 25 W sodium lasers, which will be Raman Fiber lasers that utilize second harmonic generation to achieve 598 nm output. Such lasers allow for high output, high reliability, and strong interface with the adaptive optics system in the NFIRAOS. Figure 26 demonstrates the wavefront correction suite that will be incorporated into the TMT telescope.

4 Next-Generation Observatories

4.1 Enclosure Design

The NGTs are incorporating larger systems with greater precision requirements than ever before in history. The ground-based systems require housing that is larger than any previous telescope system enclosures, with some structure being of a similar scale as a large sport stadium. Additionally, they require high precision and accuracy in alignment in azimuthal and altitudinal pointing while providing excellent stray light control. To minimize atmospheric losses, the ground-based NGTs are being installed primarily at very high altitudes and require wind control mechanisms to minimize wind-induced vibrations, as well as methods to control for earthquake-induced movements. Finally, the tracking and movement speeds for these systems are expected to operate at the same or higher rates as the current generation of smaller telescopes. To accommodate these requirements, novel design choices have been made for the enclosure systems of these telescopes [20].

One novel aspect in many of the newer telescopes is managing a wider field of view. This requirement demands unique optical designs and configurations, as well as new enclosure choices to provide the required viewing aperture for the telescope optics while still providing the required protection. For example, the LSST, with its 8.4-m diameter primary mirror and wide field of view (3.5°), is particularly susceptible to stray light and requires a unique design to mitigate the issue while also balancing wind-induced vibrations [79]. To accommodate wind vibration and stray light management the enclosure incorporates a rotating windscreen as well as a light baffle system. The windscreen itself operates as a light screen and helps to define a clear aperture for viewing. All vents include a light baffle system and will provide dome flushing to minimize air turbulence inside of

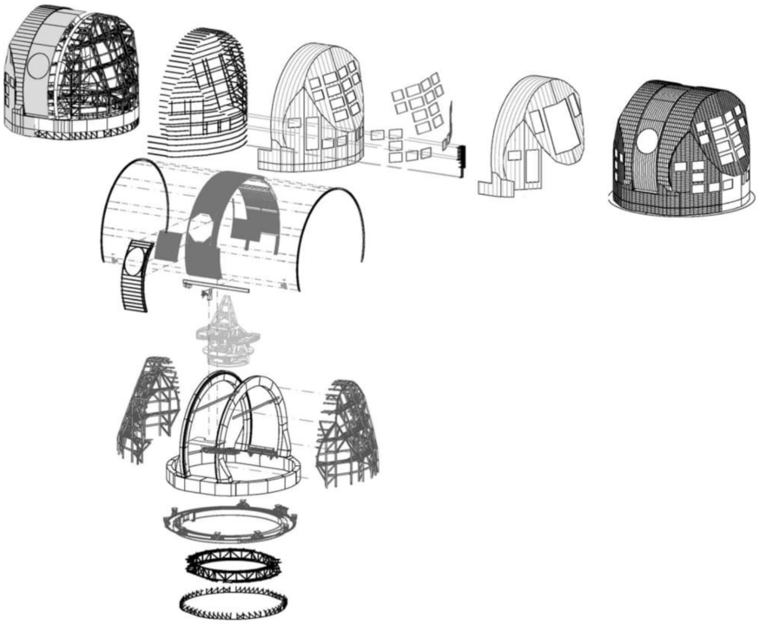

Fig. 27 The DKIST enclosure required a unique mechanism to accurately and quickly track the Sun. The main aperture is guided using a crawler system, which offers greater precision and speed in movement. To maintain structural rigidity over the motion two twin arches are used to support the crawler system. Further, the azimuthal pointing is controlled using a rotating ring which the entire enclosure is mounted on top of [80]

the enclosure. Additionally, the system is expected to operate continuously without rotational travel limits. To accommodate this requirement, the Azimuth drives for the system are in the lower enclosure, which allows for glycol water cooling without the need for a utility cable wrap. Lastly, temperature conditioning during daytime use will be controlled via an air vent which aligns with the dome in the parked position.

While the LSST requires a large, unrestricted field of view and excellent stray light control, the DKIST requires a highly precise aperture and tracking mechanism to meet the 0.03 arcsec visible solar imaging resolution laid out in its science mission. The telescope will soon be providing unprecedented observations of the Sun at the Haleakala High Altitude Observatory in Maui, Hawaii. Due to its mission of performing fine detailed solar observations, there are unique requirements placed on the dome enclosure design for the DKIST system, which is 22 m in height and 26.6 m in diameter [21]. Figure 27 demonstrates the various components in the support and steering systems that make up the enclosure.

Perhaps the most unique design feature in the DKIST enclosure is the method used to position the system's first aperture stop. This aperture stop must track the Sun to high accuracy and provide a clear viewing aperture while precisely controlling stray light. Because of the speed and accuracy required to precisely track the Sun a more traditional aperture system was ruled out for the telescope. Instead, the shutter system for the DKIST telescope utilizes a crawler type system, which achieves positioning accuracy with a maximum tracking velocity of 0.75°/s [80]. Further, the crawler system will always have several teeth in contact with the gearing system that controls movement, assuring steady and reliable tracking motion of the aperture. Due to the high thermal load placed on the system, the aperture shutter was designed to be actively water cooled. The shutter system itself is reinforced to accommodate varying gravitational loads based on the position. To maintain the required position accuracy, the altitude positioning system, via the crawler mechanism, is supported by two arch girders which provide high torsional strength and are further strengthened by the secondary structure. The arch girders are attached to a base ring, which is a key component for the azimuthal pointing system.

One final area that has introduced major design innovations in enclosures is that of extremely large telescopes. Due to the large aperture area required to permit light into the telescopes and the sheer size of these structures various new practices have been developed. The GMT enclosure takes a novel approach to the shutter concept for the system. The enclosure utilizes vertical shutter doors which can open and close depending on the activity of the telescope. For the vertical region, a horizontally sliding segment can retract to open the telescope to the night skies. A vertically sliding windscreen can also be deployed when the shutter is open, and the enclosure will have a robust seismic isolation system [81]. Figure 28 demonstrates a model of the proposed enclosure for the GMT system.

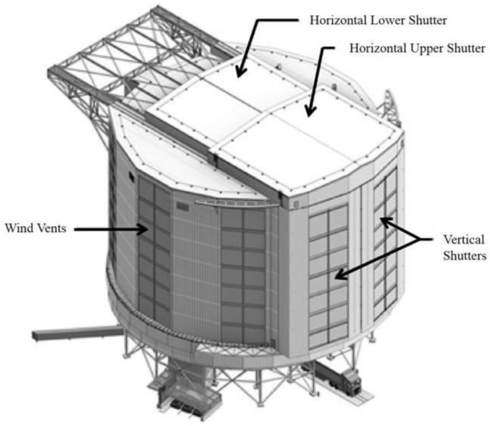

Fig. 28 The GMT enclosure departs from a dome shape in part due to the extreme size of the enclosure and the required shutter opening area. Instead, twin vertical shutters will slide horizontally to open the system while a top horizontal shutter will open as well. A deployable windscreen can also be used to minimize wind effects [81]

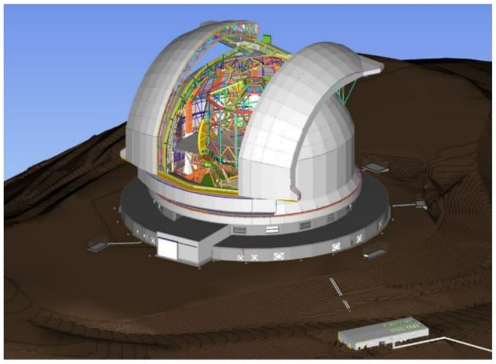

Fig. 29 The E-ELT enclosure will be a super-massive structure which houses the 40-m telescope. The structure currently is designed as a hemispherical dome with two sliding doors that will open the telescope to the night skies. The entire dome rests on a circular track which will allow for rotation of the enclosure. Due to the enormous size, multiple support structures are planned to maintain the required stiffness and positioning accuracy of all components [83]

The E-ELT takes a different approach to the shutter requirement. While it too will make use of two horizontally sliding twin doors to create a shutter, the enclosure is a more traditional dome design, and the vast shutter doors structure will slide apart to open the aperture [82]. Beyond that, the E-ELT will require a seismic isolation system to isolate the telescope system from any seismic vibrations. The dome itself is a hemispherical shape which rests upon a track which allows for rotation. The rotating enclosure will weigh 5500 tons and requires multiple support arches and structures [83]. Figure 29 displays the projected final dome design for the E-ELT.

4.2 Observatory Locations

The locations of the NGT observatories place significant demands on the structure designs. Despite the challenges, however, these exceptional sites provide key conditions essential for the observatories to accomplish their scientific goals. In order to increase the useful on-sky time for the next generation of ground-based telescopes, site selections must consider weather patterns in a changing climate (to minimize cloudy nights), minimize present and future light pollution from nearby cities, consider atmospheric turbulence that compromises image quality, and—for infrared observations—seek to minimize atmospheric water vapor content due to water's strong absorption bands. Thus, we see a preference for remote, mountainous deserts. With these considerations in mind, most of the next generation of telescopes will be located either on the summits of mountains in Hawaii or Chile.

The GMT system will be located at Las Campanas Observatory and the E-ELT in Cerro Armazones in Chile [84]. These sites have some defining features that make them ideal sites for observatories. Namely, the observatories are at the summits of tall but accessible mountains, thus reducing light pollution and creating a situation where there is less atmospheric interference between the telescope and space. Key parameters that were considered when selecting these locations, and the specific position inside the observatory area, were the cloud cover index and the frequency of achieving photometric sky conditions, as well as spectroscopic sky conditions. Additionally, wind speeds are low enough that the telescopes will be able to remain open to observations for a significant amount of time, while temperature is quite stable, and humidity is ideally low. Perhaps most important, however, is the precipitable water vapor (PWV) characteristics. The goal is to have low PWV values which are stable over the night [85].

The TMT is planning to build on Mauna Kea in Hawaii [86]. Like Cerro Campanas, the summit of Mauna Kea offers the required wind, humidity, and light levels for the observatories to maximize their scientific capabilities. The DKIST telescope construction is well underway on the Haleakala in Hawaii, which has access to quality infrastructure benefiting the construction process [87].

5 Concluding Remarks

The next generation of telescopes promise to be key enablers for future discoveries in astronomy. To achieve the required performance, novel design choices and improvements are being made at all levels of the telescopes. The new norm for optics used in the NGTs are those of extremely large freeform surfaces, with some systems such as the LSST and GMT utilizing monolithic mirror segments up to 8.4-m in diameter, and others with numerous 1.5-m sized segments. The scope of the primary mirrors has defined a new subset of telescopes, known as extremely large telescopes, whose primary mirror diameters can range up 40 m.

The size of these optics and the tolerances required have demanded novel ultra-precise and efficient fabrication methods. From utilizing rapid CNC machining processes and diamond-turned optics with precise grinding and polishing techniques, the fabrication methods are producing more accurate surfaces over a wider range of freeform shapes. To verify the surfaces created and guide the fabrication process, novel and improved metrology methods have been developed. For example, deflectometry has begun to be used in a variety of different ways to provide metrology from the grinding phase through to micro-finish measurements. Additionally, improvements in interferometry have led to better results when performing subaperture measurements, an essential technique for quantifying convex optics, as well as improved interferometric methods which utilize CGHs for nulling and alignment. With these methods, the most accurate, freeform, and largest optics ever produced are now being put together to create the next generation of telescopes.

The work does not end after fabrication. Complex structures and enclosures are necessary to assure proper alignment of the optics, as well as tracking capabilities. The enclosures must provide light baffling and prevent wind or seismic events from disrupting or damaging the optics. This has driven the extremely large telescope systems to explore shutters which slide horizontally to accommodate the vast shutter areas required. Due to entirely different design requirements calling for high speed, high accuracy aperture positions, the DKIST telescope uses a more traditional circular aperture driven by a novel crawler system to meet stringent accuracy and tracking speed requirements.

Finally, once the telescopes have been installed in their structures, they will undergo active and adaptive optical control to achieve the best possible results. The active control of optics will allow for accurate mirror alignment throughout observation and can utilize phasing measurements to assure all segmented mirrors are appropriately aligned and co-phased throughout operation. The adaptive optics, for ground-based systems, will greatly improve optical performance by compensating atmospheric-induced aberrations using high-frequency corrections, allowing for near diffraction-limited performance for these systems.

When the next generation of telescopes goes on-line, with some planning to begin operations as early as 2019, astronomers will have access to an unprecedented amount of detailed scientific information. These instruments promise to provide a look farther back in time, provide greater resolution, wider fields of view, and more detailed data acquisition. Further, they will work in conjunction with not only each other but the existing telescope systems to complement one another. We now must wait and watch as these super-instruments complete the final steps in their complex and long development process before they begin producing scientific results.

Acknowledgements We would like to thank Antonin Bouchez for his expert input to the paper's adaptive and active optics section. Also, this review and summary work was made possible in part by the II–VI Foundation Block-Gift Program, the Technology Research Initiative Fund Optics/Imaging Program, the Korea Basic Science Institute Foundation, and the Friends of Tucson Optics Endowed Scholarships in Optical Sciences.

References

1. Bernstein R, Dressler A, Apai D, Asplund M, Blum R, Brough S, Crane J, Cypriano E, Eisenstein D, Eisner J, Fabricant D, Gladders M, Greene J, Hwang N, Krause A, Papovich C, Sharp R, Simcoe R, Zaritsky D (2018) GMT Science Book 2018. Giant Magellan Telescope. GMTO, Vallenar
2. European Southern Observatory (2010) An expanded view of the universe: science with the European Extremely Large Telescope. Garching bei München, Germany, European Southern Observatory
3. King HC (1955) The history of the telescope. Griffin, London
4. Fanson J, McCarthy PJ, Bernstein R, Angeli G, Ashby D, Bigelow B, Bouchez A, Burgett W, Chauvin E, Contos A, Figueroa F, Gray P, Groark F, Laskin R, Millan-Gabet R, Rakich A, Sandoval R, Pi M, Wheeler N (2018) Overview and status of the Giant Magellan Telescope project. In: Ground-based and airborne telescopes VII. Presented at the ground-based and airborne telescopes VII, international society for optics and photonics, p 1070012. https://doi.org/10.1117/12.2313340
5. Martins CJAP, Leite ACO, Pedrosa POJ (2014) Fundamental cosmology with the E-ELT. Proc Int Astron Union 10:385–387. https://doi.org/10.1017/S1743921314013441
6. Skidmore W, Anupama GC, Srianand R (2018) The Thirty Meter Telescope International Observatory facilitating transformative astrophysical science. arXiv:1806.02481[astro-ph]
7. Skidmore W (2015) Thirty Meter Telescope detailed science case: 2015. Res Astron Astrophys 15:1945. https://doi.org/10.1088/1674-4527/15/12/001
8. Rudnick L, NASA, JPL-Caltech (2006) Lighting up a dead star's layers. NASA Spitzer Space Telescope. http://www.spitzer.caltech.edu/images/1675-ssc2006-19a-Lighting-up-a-Dead-Star-s-Layers. Accessed 8 Oct 2018
9. Tamai R, Spyromilio J (2014) European extremely large telescope: progress report. In: Ground-based and airborne telescopes V. Presented at the ground-based and airborne telescopes V, international society for optics and photonics, p 91451E. https://doi.org/10.1117/12.2058467
10. Tamai R, Cirasuolo M, González JC, Koehler B, Tuti M (2016) The E-ELT program status. In: Ground-based and airborne telescopes VI. Presented at the ground-based and airborne telescopes VI, international society for optics and photonics, p 99060W. https://doi.org/10.1117/12.2232690
11. Lightsey PA, Atkinson CB, Clampin MC, Feinberg LD (2012) James Webb Space Telescope: large deployable cryogenic telescope in space. OE, OPEGAR 51:011003. https://doi.org/10.1117/1.OE.51.1.011003
12. Ivezić Ž, Kahn SM, Tyson JA, Abel B, Acosta E, Allsman R, Alonso D, AlSayyad Y, Anderson SF, Andrew J, Angel JRP, Angeli GZ, Ansari R, Antilogus P, Araujo C, Armstrong R, Arndt KT, Astier P, Aubourg É, Auza N, Axelrod TS, Bard DJ, Barr JD, Barrau A, Bartlett JG, Bauer AE, Bauman BJ, Baumont S, Becker AC, Becla J, Beldica C, Bellavia S, Bianco FB, Biswas R, Blanc G, Blazek J, Blandford RD, Bloom JS, Bogart J, Bond TW, Borgland AW, Borne K, Bosch JF, Boutigny D, Brackett CA, Bradshaw A, Brandt WN, Brown ME, Bullock JS, Burchat P, Burke DL, Cagnoli G, Calabrese D, Callahan S, Callen AL, Chandrasekharan S, Charles-Emerson G, Chesley S, Cheu EC, Chiang H-F, Chiang J, Chirino C, Chow D, Ciardi DR, Claver CF, Cohen-Tanugi J, Cockrum JJ, Coles R, Connolly AJ, Cook KH, Cooray A, Covey KR, Cribbs C, Cui W, Cutri R, Daly PN, Daniel SF, Daruich F, Daubard G, Daues G, Dawson W, Delgado F, Dellapenna A, de Peyster R, de Val-Borro M, Digel SW, Doherty P, Dubois R, Dubois-Felsmann GP, Durech J, Economou F, Eracleous M, Ferguson H, Figueroa E, Fisher-Levine M, Focke W, Foss MD, Frank J, Freemon MD, Gangler E, Gawiser E, Geary JC, Gee P, Geha M, Gessner CJB, Gibson RR, Gilmore DK, Glanzman T, Glick W, Goldina T, Goldstein DA, Goodenow I, Graham ML, Gressler WJ, Gris P, Guy LP, Guyonnet A, Haller G, Harris R, Hascall PA, Haupt J, Hernandez F, Herrmann S, Hileman E, Hoblitt J, Hodgson JA, Hogan C, Huang D, Huffer ME, Ingraham P, Innes WR, Jacoby SH, Jain B, Jammes F, Jee J, Jenness T, Jernigan G, Jevremović D, Johns K, Johnson AS, Johnson MWG, Jones RL, Juramy-Gilles C, Jurić M, Kalirai JS, Kallivayalil NJ, Kalmbach B, Kantor JP, Karst P, Kasliwal MM, Kelly H, Kessler R, Kinnison V, Kirkby D, Knox L, Kotov IV, Krabbendam VL, Krughoff KS, Kubánek P, Kuczewski J, Kulkarni S, Ku J, Kurita NR, Lage CS, Lambert R, Lange T, Langton JB, Guillou LL, Levine D, Liang M, Lim K-T, Lintott CJ, Long KE, Lopez M, Lotz PJ, Lupton RH, Lust NB, MacArthur LA, Mahabal A, Mandelbaum R, Marsh DS, Marshall PJ, Marshall S, May M, McKercher R, McQueen M, Meyers J, Migliore M, Miller M, Mills DJ, Miraval C, Moeyens J, Monet DG, Moniez M, Monkewitz S, Montgomery C, Mueller F, Muller GP, Arancibia FM, Neill DR, Newbry SP, Nief J-Y, Nomerotski A, Nordby M, O'Connor P, Oliver J, Olivier SS, Olsen K, O'Mullane W, Ortiz S, Osier S, Owen RE, Pain R, Palecek PE, Parejko JK, Parsons JB, Pease NM, Peterson JM, Peterson JR, Petravick DL, Petrick MEL, Petry CE, Pierfederici F, Pietrowicz S, Pike R, Pinto PA, Plante R, Plate S, Price PA, Prouza M, Radeka V, Rajagopal J, Rasmussen AP, Regnault N, Reil KA, Reiss DJ, Reuter MA, Ridgway ST, Riot VJ, Ritz S, Robinson S, Roby W, Roodman A, Rosing W, Roucelle C, Rumore MR, Russo S, Saha A, Sassolas B, Schalk TL, Schellart P, Schindler RH, Schmidt S, Schneider DP, Schneider MD, Schoening W, Schumacher G, Schwamb ME, Sebag J, Selvy B, Sembroski GH, Seppala LG, Serio A, Serrano E, Shaw RA, Shipsey I, Sick J, Silvestri N, Slater CT, Smith JA, Smith RC, Sobhani S, Soldahl

C, Storrie-Lombardi L, Stover E, Strauss MA, Street RA, Stubbs CW, Sullivan IS, Sweeney D, Swinbank JD, Szalay A, Takacs P, Tether SA, Thaler JJ, Thayer JG, Thomas S, Thukral V, Tice J, Trilling DE, Turri M, Van Berg R, Berk DV, Vetter K, Virieux F, Vucina T, Wahl W, Walkowicz L, Walsh B, Walter CW, Wang DL, Wang S-Y, Warner M, Wiecha O, Willman B, Winters SE, Wittman D, Wolff SC, Wood-Vasey WM, Wu X, Xin B, Yoachim P, Zhan H, Collaboration for the L (2008) LSST: from science drivers to reference design and anticipated data products. arXiv:0805.2366[astro-ph]

13. Sassolas B, Teillon J, Flaminio R, Michel C, Morgado N, Pinard L (2013) Development on large band-pass filters for the wide field survey telescope LSST. In: Optical interference coatings (2013), paper MD.2. Presented at the optical interference coatings, optical society of America, MD.2. https://doi.org/10.1364/OIC.2013.MD.2
14. Martin HM, Angel JRP, Angeli GZ, Burge JH, Gressler W, Kim DW, Kingsley JS, Law K, Liang M, Neill D, Sebag J, Strittmatter PA, Tuell MT, West SC, Woolf NJ, Xin B (2016) Manufacture and final tests of the LSST monolithic primary/tertiary mirror. In: Advances in optical and mechanical technologies for telescopes and instrumentation II. Presented at the advances in optical and mechanical technologies for telescopes and instrumentation II, international society for optics and photonics, p 99120X. https://doi.org/10.1117/12.2234501
15. Callahan S, Gressler W, Thomas SJ, Gessner C, Warner M, Barr J, Lotz PJ, Schumacher G, Wiecha O, Angeli G, Andrew J, Claver C, Schoening B, Sebag J, Krabbendam V, Neill D, Hileman E, Muller G, Araujo C, Martinez AO, Aguado MP, García-Marchena L, Argandoña IR, de Romero FM, Rodríguez R, González JC, Venturini M (2016) Large Synoptic Survey Telescope mount final design. In: Ground-based and airborne telescopes VI. Presented at the ground-based and airborne telescopes VI, international society for optics and photonics, p 99060M. https://doi.org/10.1117/12.2232996
16. Tritschler A, Rimmele TR, Berukoff S, Casini R, Kuhn JR, Lin H, Rast MP, McMullin JP, Schmidt W, Wöger F, Team D (2016) Daniel K. Inouye Solar Telescope: high-resolution observing of the dynamic Sun. Astron Nachr 337:1064–1069. https://doi.org/10.1002/asna.201612434
17. Bouchez AH, Angeli GZ, Ashby DS, Bernier R, Conan R, McLeod BA, Quirós-Pacheco F, van Dam MA (2018) An overview and status of GMT active and adaptive optics. In: Adaptive optics systems VI. Presented at the adaptive optics systems VI, international society for optics and photonics, p 107030W. https://doi.org/10.1117/12.2314255
18. Boyer C (2018) Adaptive optics program at TMT. In: Adaptive optics systems VI. Presented at the adaptive optics systems VI, international society for optics and photonics, p 107030Y. https://doi.org/10.1117/12.2313753
19. Perrin MD, Acton DS, Lajoie C-P, Knight JS, Lallo MD, Allen M, Baggett W, Barker E, Comeau T, Coppock E, Dean BH, Hartig G, Hayden WL, Jordan M, Jurling A, Kulp T, Long J, McElwain MW, Meza L, Nelan EP, Soummer R, Stansberry J, Stark C, Telfer R, Welsh AL, Zielinski TP, Zimmerman NT (2016) Preparing for JWST wavefront sensing and control operations. In: Space telescopes and instrumentation 2016: optical, infrared, and millimeter wave. Presented at the space telescopes and instrumentation 2016: optical, infrared, and millimeter wave, international society for optics and photonics, p 99040F. https://doi.org/10.1117/12.2233104
20. Murga G, Bilbao A, de Bilbao L, Lorentz TE (2016) Design solutions for dome and main structure (mount) of giant telescopes. In: Ground-based and airborne telescopes VI. Presented at the ground-based and airborne telescopes VI, international society for optics and photonics, p 99060C. https://doi.org/10.1117/12.2233502
21. Murga G, Marshall HK, Lorentz TE, Ariño J, Ampuero P (2014) DKIST enclosure fabrication factory assembly and testing. In: Ground-based and airborne telescopes V. Presented at the ground-based and airborne telescopes V, international society for optics and photonics, p 914527. https://doi.org/10.1117/12.2055320
22. Roll J, Thompson K (2012) Freeform optics: evolution? No, revolution! | SPIE Homepage: SPIE. http://spie.org/newsroom/4309-freeform-optics-evolution-no-revolution?SSO=1. Accessed 15 Nov 2018
23. Dimmler M, Barriga P, Cayrel M, Derie F, Foerster A, Gonte F, Gonzalez JC, Jochum L, Kornweibel N, Leveque S, Lucuix C, Pettazzi L (2018) Getting ready for serial production of the segmented 39-meter ELT primary: status, challenges and strategies. In: Ground-based and airborne telescopes VII. Presented at the ground-based and airborne telescopes VII, international society for optics and photonics, p 1070043. https://doi.org/10.1117/12.2312073
24. Crampton D, Ellerbroek B. (2005) Design and development of TMT. International Astronomical Union. In: Proceedings of the International Astronomical Union; Cambridge, vol 1, pp 410–419
25. Seo B-J, Nissly C, Colavita M, Troy M, Roberts S, Rogers J (2018) Optical performance prediction of the Thirty Meter Telescope after initial alignment using optical modeling. In: Modeling, systems engineering, and project management for astronomy VIII. Presented at the modeling, systems engineering, and project management for astronomy VIII, international society for optics and photonics, p 107050T. https://doi.org/10.1117/12.2314351
26. Stepp L (2012) Thirty Meter Telescope project update. In: Ground-based and airborne telescopes IV. Presented at the ground-based and airborne telescopes IV, international society for optics and photonics, p 84441G. https://doi.org/10.1117/12.928006
27. Nella J, Atcheson PD, Atkinson CB, Au D, Bronowicki AJ, Bujanda E, Cohen A, Davies D, Lightsey PA, Lynch R, Lundquist R, Menzel MT, Mohan M, Pohner J, Reynolds P, Rivera H, Texter SC, Shuckstes DV, Simmons DDF, Smith RC, Sullivan PC, Waldie DD, Woods R (2004) James Webb Space Telescope (JWST) observatory architecture and performance. In: Optical, infrared, and millimeter space telescopes. Presented at the optical, infrared, and millimeter space telescopes, international society for optics and photonics, pp 576–588. https://doi.org/10.1117/12.548928
28. Hubbard R (2013) M1 microroughness and dust contamination (no. 0013, rev. C), advanced technology solar telescope technical note
29. Blalock T, Medicus K, Nelson JD (2015) Fabrication of freeform optics. In: Optical manufacturing and testing XI. Presented at the optical manufacturing and testing XI, international society for optics and photonics, p 95750H. https://doi.org/10.1117/12.2188523
30. Fess E, Bechtold M, Wolfs F, Bechtold R (2013) Developments in precision optical grinding technology. In: Optifab 2013. Presented at the Optifab 2013, international society for optics and photonics, p 88840L. https://doi.org/10.1117/12.2029334
31. Walker DD, Brooks D, King A, Freeman R, Morton R, McCavana G, Kim S-W (2003) The ‘precessions’ tooling for polishing and figuring flat, spherical and aspheric surfaces. Opt Express OE 11:958–964. https://doi.org/10.1364/OE.11.000958
32. Gurganus D, Owen JD, Dutterer BS, Novak S, Symmons A, Davies MA (2018) Precision glass molding of freeform optics. In: Optical manufacturing and testing XII. Presented at the optical manufacturing and testing XII, international society for optics and photonics, p 107420Q. https://doi.org/10.1117/12.2320574
33. Risse S, Scheiding S, Beier M, Gebhardt A, Damm C, Peschel T (2014) Ultra-precise manufacturing of aspherical and freeform

mirrors for high resolution telescopes. In: Advances in optical and mechanical technologies for telescopes and instrumentation. Presented at the advances in optical and mechanical technologies for telescopes and instrumentation, international society for optics and photonics, p 91510M. https://doi.org/10.1117/12.2056496

34. Fang F, Xu F (2018) Recent advances in micro/nano-cutting: effect of tool edge and material properties. Nanomanufacturing Metrol 1:4–31. https://doi.org/10.1007/s41871-018-0005-z
35. Beier M, Scheiding S, Gebhardt A, Loose R, Risse S, Eberhardt R, Tünnermann A (2013) Fabrication of high precision metallic freeform mirrors with magnetorheological finishing (MRF). In: Optifab 2013. Presented at the Optifab 2013, international society for optics and photonics, p 88840S. https://doi.org/10.1117/12.2035986
36. Martin HM, Allen RG, Burge JH, Davis JM, Davison WB, Johns M, Kim DW, Kingsley JS, Law K, Lutz RD, Strittmatter PA, Su P, Tuell MT, West SC, Zhou P (2014) Production of primary mirror segments for the Giant Magellan Telescope. In: Advances in optical and mechanical technologies for telescopes and instrumentation. Presented at the advances in optical and mechanical technologies for telescopes and instrumentation, international society for optics and photonics, p 91510J. https://doi.org/10.1117/12.2057012
37. Martin HM, Allen RG, Burge JH, Kim DW, Kingsley JS, Law K, Lutz RD, Strittmatter PA, Su P, Tuell MT, West SC, Zhou P (2012) Production of 8.4 m segments for the Giant Magellan Telescope. In: Modern technologies in space- and ground-based telescopes and instrumentation II. Presented at the modern technologies in space- and ground-based telescopes and instrumentation II, international society for optics and photonics, p 84502D. https://doi.org/10.1117/12.926347
38. West SC, Angel R, Cuerden B, Davison W, Hagen J, Martin HM, Kim DW, Sisk B (2014) Development and results for stressed-lap polishing of large telescope mirrors1. In: Classical optics 2014 (2014), paper OTh2B.4. Presented at the optical fabrication and testing, optical society of america, p OTh2B.4. https://doi.org/10.1364/OFT.2014.OTh2B.4
39. Kim DW, Martin HM, Burge JH (2011) Calibration and optimization of computer-controlled optical surfacing for large optics. In: Optical manufacturing and testing IX. Presented at the optical manufacturing and testing IX, international society for optics and photonics, p 812615. https://doi.org/10.1117/12.893878
40. Cole G (2017) Optical fabrication and metrology for the thirty meter telescope primary mirror segments. In: Optical design and fabrication 2017 (Freeform, IODC, OFT) (2017), paper OW1B.4. Presented at the optical fabrication and testing, optical society of America, p OW1B.4. https://doi.org/10.1364/OFT.2017.OW1B.4
41. Geyl R, Bardon D, Bourgois R, Ferachoglou N, Harel E, Couteret C (2018) First steps in ELT optics polishing. In: Fifth European seminar on precision optics manufacturing. Presented at the fifth European seminar on precision optics manufacturing, international society for optics and photonics, p 1082904. https://doi.org/10.1117/12.2317604
42. Gray C, Baker I, Davies G, Evans R, Field N, Fox-Leonard T, Messelink W, Mitchell J, Rees P, Waine S, Walker DD, Yu G (2013) Fast manufacturing of E-ELT mirror segments using CNC polishing. In: Optical manufacturing and testing X. Presented at the optical manufacturing and testing X, international society for optics and photonics, p 88380K. https://doi.org/10.1117/12.2023475
43. Yu G, Walker DD, Li H (2012) Research on fabrication of mirror segments for E-ELT. In: 6th international symposium on advanced optical manufacturing and testing technologies: advanced optical manufacturing technologies. Presented at the 6th international symposium on advanced optical manufacturing and testing technologies: advanced optical manufacturing technologies, international society for optics and photonics, p 841602. https://doi.org/10.1117/12.2009290
44. Acosta D, Albajez JA, Yagüe-Fabra JA, Velázquez J (2018) Verification of machine tools using multilateration and a geometrical approach. Nanomanufacturing Metrol 1:39–44. https://doi.org/10.1007/s41871-018-0006-y
45. Gallagher B, Bergeland M, Brown B, Chaney D, Copp T, Lewis J, Shogrin B, Smith K, Sokol J, Hadaway J, Glatzel H, Johnson P, Lee A, Patriarca D, Stevenson I, Cluney J, Parsonage T, Calvert J, Rodgers B, McKay A, Texter S, Cohen L, Feinberg L (2011) JWST mirror production status. In: UV/Optical/IR space telescopes and instruments: innovative technologies and concepts V. Presented at the UV/Optical/IR space telescopes and instruments: innovative technologies and concepts V, international society for optics and photonics, p 814607. https://doi.org/10.1117/12.892326
46. Trumper I, Jannuzi BT, Kim DW (2018) Emerging technology for astronomical optics metrology. Opt Lasers Eng Opt Tools Metrol Imaging Diagn 104:22–31. https://doi.org/10.1016/j.optlaseng.2017.09.009
47. Rees PCT, Gray C (2015) Metrology requirements for the serial production of ELT primary mirror segments. In: Optical manufacturing and testing XI. Presented at the optical manufacturing and testing XI, international society for optics and photonics, p 957508. https://doi.org/10.1117/12.2189783
48. Bos A, Henselmans R, Rosielle PCJN, Steinbuch M (2015) Nanometre-accurate form measurement machine for E-ELT M1 segments. Precis Eng 40:14–25. https://doi.org/10.1016/j.precisioneng.2014.09.008
49. Mueller U (2016) Production metrology design and calibration for TMT primary mirror fabrication used at multiple manufacturing sites. In: Ground-based and airborne telescopes VI. Presented at the ground-based and airborne telescopes VI, international society for optics and photonics, p 99060Z. https://doi.org/10.1117/12.2232036
50. Anderson DS, Burge JH (1995) Swing-arm profilometry of aspherics. In: Optical manufacturing and testing. Presented at the optical manufacturing and testing, international society for optics and photonics, pp 169–180. https://doi.org/10.1117/12.218421
51. Callender MJ, Efstathiou A, King CW, Walker DD, Gee AE, Lewis AJ, Oldfield S, Steel RM (2006) A swing arm profilometer for large telescope mirror element metrology. In: Optomechanical technologies for astronomy. Presented at the optomechanical technologies for astronomy, international society for optics and photonics, p 62732R. https://doi.org/10.1117/12.671304
52. Su P, Wang Y, Oh CJ, Parks RE, Burge JH (2011) Swing arm optical CMM: self calibration with dual probe shear test. In: Optical manufacturing and testing IX. Presented at the optical manufacturing and testing IX, international society for optics and photonics, p 81260W. https://doi.org/10.1117/12.894203
53. Zhang P, Li J, Yu G, Walker DD (2016) Development of swinging part profilometer for optics. In: Optics and measurement international conference 2016. Presented at the optics and measurement international conference 2016, international society for optics and photonics, p 101510B. https://doi.org/10.1117/12.2256295
54. Zobrist TL, Burge JH, Martin HM (2009) Laser tracker surface measurements of the 8.4 m GMT primary mirror segment. In: Optical manufacturing and testing VIII. Presented at the optical manufacturing and testing VIII, international society for optics and photonics, p 742613. https://doi.org/10.1117/12.826706
55. Jang Y-S, Kim S-W (2018) Distance measurements using mode-locked lasers: a review. Nanomanufacturing Metrol 1:131–147. https://doi.org/10.1007/s41871-018-0017-8
56. Knauer MC, Kaminski J, Hausler G (2004) Phase measuring deflectometry: a new approach to measure specular free-form surfaces. 366–376. https://doi.org/10.1117/12.545704

57. Huang R, Su P, Horne T, Zappellini GB, Burge JH (2013) Measurement of a large deformable aspherical mirror using SCOTS (Software Configurable Optical Test System). In: Optical manufacturing and testing X. Presented at the optical manufacturing and testing X, international society for optics and photonics, p 883807. https://doi.org/10.1117/12.2024336
58. Su T, Park WH, Parks RE, Su P, Burge JH (2011) Scanning long-wave optical test system: a new ground optical surface slope test system. In: Optical manufacturing and testing IX. Presented at the optical manufacturing and testing IX, international society for optics and photonics, p 81260E. https://doi.org/10.1117/12.892666
59. Oh CJ, Lowman AE, Smith GA, Su P, Huang R, Su T, Kim D, Zhao C, Zhou P, Burge JH (2016) Fabrication and testing of 4.2 m off-axis aspheric primary mirror of Daniel K. Inouye Solar Telescope. Advances in optical and mechanical technologies for telescopes and instrumentation II. https://doi.org/10.1117/12.2229324
60. Yoo H, Smith GA, Oh CJ, Lowman AE, Dubin M (2018) Improvements in the scanning long-wave optical test system. In: Optical manufacturing and testing XII. Presented at the optical manufacturing and testing XII, international society for optics and photonics, p 1074216. https://doi.org/10.1117/12.2321265
61. Allen R, Su P, Burge JH, Cuerden B, Martin HM (2010) Scanning pentaprism test for the GMT 8.4-m off-axis segments. In: Modern technologies in space- and ground-based telescopes and instrumentation. Presented at the modern technologies in space- and ground-based telescopes and instrumentation, international society for optics and photonics, p 773911. https://doi.org/10.1117/12.857901
62. Schulz M, Ehret G, Křen P (2013) High accuracy flatness metrology within the European metrology research program. Nuclear instruments and methods in physics research section A: accelerators, spectrometers, detectors and associated equipment. In: The 4th international workshop on metrology for x-ray optics, mirror design, and fabrication, vol 710, pp 37–41. https://doi.org/10.1016/j.nima.2012.10.112
63. Huang R (n.d.) High precision optical surface metrology using deflectometry. The University of Arizona. http://hdl.handle.net/10150/581252
64. Kim DW, Burge JH, Davis JM, Martin HM, Tuell MT, Graves LR, West SC (2016) New and improved technology for manufacture of GMT primary mirror segments. In: Advances in optical and mechanical technologies for telescopes and instrumentation II. Presented at the advances in optical and mechanical technologies for telescopes and instrumentation II, international society for optics and photonics, p 99120P. https://doi.org/10.1117/12.2231911
65. Huang R, Su P, Burge JH, Huang L, Idir M (2015) High-accuracy aspheric x-ray mirror metrology using Software Configurable Optical Test System/deflectometry. OE, OPEGAR 54:084103. https://doi.org/10.1117/1.OE.54.8.084103
66. Maldonado AV, Su P, Burge JH (2014) Development of a portable deflectometry system for high spatial resolution surface measurements. Appl Opt, AO 53:4023–4032. https://doi.org/10.1364/AO.53.004023
67. Lowman AE, Smith GA, Harrison L, West SC, Oh CJ (2018) Measurement of large on-axis and off-axis mirrors using software configurable optical test system (SCOTS). In: Advances in optical and mechanical technologies for telescopes and instrumentation III. Presented at the advances in optical and mechanical technologies for telescopes and instrumentation III, international society for optics and photonics, p 107061E. https://doi.org/10.1117/12.2313855
68. Chen S, Xue S, Dai Y, Li S (2017) Subaperture stitching test of convex aspheres by using the reconfigurable optical null. Opt Laser Technol 91:175–184. https://doi.org/10.1016/j.optlastec.2016.12.026
69. Scheiding S, Beier M, Zeitner U-D, Risse S, Gebhardt A (2013) Freeform mirror fabrication and metrology using a high performance test CGH and advanced alignment features. In: Advanced fabrication technologies for micro/nano optics and photonics VI. Presented at the advanced fabrication technologies for micro/nano optics and photonics VI, international society for optics and photonics, p 86130J. https://doi.org/10.1117/12.2001690
70. Zhou P, Martin H, Zhao C, Burge JH (2012) Mapping distortion correction for GMT interferometric test. In: Imaging and applied optics technical papers (2012), paper OW3D.2. Presented at the optical fabrication and testing, optical society of America, p OW3D.2. https://doi.org/10.1364/OFT.2012.OW3D.2
71. Hadaway JB, Wells C, Olczak G, Waldman M, Whitman T, Cosentino J, Connolly M, Chaney D, Telfer R (2016) Performance of the primary mirror center-of-curvature optical metrology system during cryogenic testing of the JWST Pathfinder telescope. In: Space telescopes and instrumentation 2016: optical, infrared, and millimeter wave. Presented at the space telescopes and instrumentation 2016: optical, infrared, and millimeter wave, international society for optics and photonics, p 99044E. https://doi.org/10.1117/12.2234741
72. Gray P, Ciattaglia E, Dupuy C, Gago F, Guisard S, Marrero J, Ridings R, Wright A (2016) E-ELT assembly, integration, and technical commissioning plans. In: Ground-based and airborne telescopes VI. Presented at the ground-based and airborne telescopes VI, international society for optics and photonics, p 99060X. https://doi.org/10.1117/12.2230965
73. Zimmerman DC (2010) Feasibility studies for the alignment of the Thirty Meter Telescope. Appl Opt, AO 49:3485–3498. https://doi.org/10.1364/AO.49.003485
74. Troy M, Chanan G, Michaels S, Dekens F, Hein R, Herzig S, Karban R, Nissly C, Roberts J, Rud M, Seo B-J (2016) The alignment and phasing system for the Thirty Meter Telescope: risk mitigation and status update. In: Ground-based and airborne telescopes VI. Presented at the ground-based and airborne telescopes VI, international society for optics and photonics, p 99066A. https://doi.org/10.1117/12.2231913
75. van Dam MA, McLeod BA, Bouchez AH (2016) Dispersed fringe sensor for the Giant Magellan Telescope. Appl Opt, AO 55:539–547. https://doi.org/10.1364/AO.55.000539
76. Kopon D, McLeod B, Bouchez A, Catropa D, van Dam MA, Frostig D, Kansky J, McCracken K, Podgorski W, McMuldroch S, D'Arco J, Close L, Males JR, Morzinski K (2018) Preliminary on-sky results of the next generation GMT phasing sensor prototype. In: Adaptive optics systems VI. Presented at the adaptive optics systems VI, international society for optics and photonics, p 107030X. https://doi.org/10.1117/12.2314381
77. Bouchez AH, McLeod BA, Acton DS, Kanneganti S, Kibblewhite EJ, Shectman SA, van Dam MA (2012) The Giant Magellan Telescope phasing system. In: Adaptive optics systems III. Presented at the adaptive optics systems III, international society for optics and photonics, p 84473S. https://doi.org/10.1117/12.927163
78. Xin B, Claver C, Liang M, Chandrasekharan S, Angeli G, Shipsey I (2015) Curvature wavefront sensing for the large synoptic survey telescope. Appl Opt, AO 54:9045–9054. https://doi.org/10.1364/AO.54.009045
79. DeVries J, Neill DR, Barr J, Lorenzi SD, Marchiori G (2016) The LSST dome final design. In: Ground-based and airborne telescopes VI. Presented at the ground-based and airborne telescopes VI, international society for optics and photonics, p 99060N. https://doi.org/10.1117/12.2233320
80. Murga G, Marshall H, Ariño J, Lorentz T (2012) ATST enclosure final design and construction plans. In: Ground-based and

airborne telescopes IV. Presented at the ground-based and airborne telescopes IV, international society for optics and photonics, p 844408. https://doi.org/10.1117/12.925987

81. Teran J, Sheehan M, Neff DH, Korde N, Manuel E, Ortega A (2014) GMT enclosure structure and mechanism design. In: Ground-based and airborne telescopes V. Presented at the ground-based and airborne telescopes V, international society for optics and photonics, p 91454L. https://doi.org/10.1117/12.2055189
82. Bilbao A, Murga G, Gómez C, Llarena J (2014) Approach to the E-ELT dome and main structure challenges. In: Ground-based and airborne telescopes V. Presented at the ground-based and airborne telescopes V, international society for optics and photonics, p 91452J. https://doi.org/10.1117/12.2054866
83. Stanghellini S, Martinez P, Kraus M (2018) Procurement of the dome and the telescope structure of the ESO ELT: status report. In: Ground-based and airborne telescopes VII. Presented at the ground-based and airborne telescopes VII, international society for optics and photonics, p 1070009. https://doi.org/10.1117/12.2313510
84. Thomas-Osip JE, McCarthy P, Prieto G, Phillips MM, Johns M (2010) Giant Magellan Telescope site testing: summary. In: Ground-based and airborne telescopes III. Presented at the ground-based and airborne telescopes III, international society for optics and photonics, p 77331L. https://doi.org/10.1117/12.856934
85. Teran J, Burgett WS, Grigel E, Bigelow BC, Donoso E, Figueroa F (2016) GMT site, enclosure, and facilities design and development overview and update. In: Ground-based and airborne telescopes VI. Presented at the ground-based and airborne telescopes VI, international society for optics and photonics, p 990610. https://doi.org/10.1117/12.2232573
86. Teran J, Sanders G, Falcon G, Adriaanse D, Gillett P, Dumas C (2018) Alternate site selection and development for the Thirty Meter Telescope at Observatorio del Roque de los Muchachos, La Palma, Spain. In: Ground-based and airborne telescopes VII. Presented at the ground-based and airborne telescopes VII, international society for optics and photonics, p 1070053. https://doi.org/10.1117/12.2313646
87. Warner M, Rimmele TR, Pillet VM, Casini R, Berukoff S, Craig SC, Ferayorni A, Goodrich BD, Hubbard RP, Harrington D, Jeffers P, Johansson EM, Kneale R, Kuhn J, Liang C, Lin H, Marshall H, Mathioudakis M, McBride WR, McMullin J, McVeigh W, Sekulic P, Schmidt W, Shimko S, Sueoka S, Summers R, Tritschler A, Williams TR, Wöger F (2018) Construction update of the Daniel K. Inouye Solar Telescope project. In: Ground-based and airborne telescopes VII. Presented at the ground-based and airborne telescopes VII, international society for optics and photonics, p 107000V. https://doi.org/10.1117/12.2314212

Logan R. Graves is a Ph.D. candidate in the College of Optical Sciences at the University of Arizona. His main research area covers precision optical metrology, focusing on deflectometry hardware and software development for improved freeform measurement capabilities. He also has a background in biomedical engineering, with research topics including early cancer detection utilizing autofluorescence and non-linear rod-cone interactions at the retinal level.

Greg A. Smith conducts research in large optics manufacturing and testing at the College of Optical Sciences, University of Arizona. He received his optics Ph.D. in 2006 and specializes in the areas of polarization optics and software algorithms for optical metrology. His experience with large optic manufacturing ranges from development of computer controlled polishing systems for a 4m off-axis parabola to metrology tools which can measure optical surfaces with 40-micron grit surface finish.

Dániel Apai is an associate professor at the Steward Observatory and the Lunar and Planetary Laboratory of The University of Arizona. He is specializing in studies of extrasolar planets with the goal of identifying planetary systems capable of supporting life. He is leading major programs on the Hubble and Spitzer Space Telescopes, and also regularly uses the largest ground-based telescopes for his studies. Dr. Apai is currently serving on the Giant Magellan Telescope Science Advisory Committee and on the Steering Committee of the NASA Nexus for Exoplanet System Science.

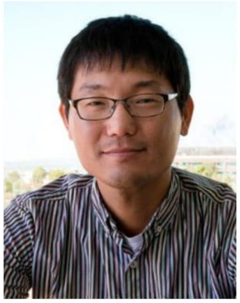

Dae Wook Kim is an assistant professor of optical sciences and astronomy at the University of Arizona. He has been working in the optical engineering field for more than 10 years, mainly focusing on very large astronomical optics, such as the 25 m diameter Giant Magellan Telescope primary mirrors. His main research area covers precision freeform optics fabrication and various metrology topics, such as interferometric test systems using computer generated holograms, direct curvature measurements, and dynamic deflectometry systems. He is currently a chair of the Optical Manufacturing and Testing conference (SPIE), Optical Fabrication and Testing conference (OSA), and Astronomical Optics: Design, Manufacture, and Test of Space and Ground Systems conference (SPIE). He is a senior member of OSA and SPIE and has been serving as an associate editor for the journal Optics Express.